UCN Production and Analysis and Magnetic Stability Studies for the Future neutron Electric Dipole Moment Experiment at TRIUMF(?)

what is the subtitle?

by

Taraneh Andalib

A Thesis submitted to the Faculty of Graduate Studies of

The University of Manitoba

in partial fulfilment of the requirements of the degree of

Doctor of Philosophy

Department of Physics and Astronomy
University of Manitoba
Winnipeg

Copyright © 2018 by Taraneh Andalib

Abstract

text of the abstract

Acknowledgment

text of the acknowledgment

Dedicated to myself!!

Contents

List of Figures

List of Tables

Chapter 1

Introduction

This thesis is focused on two important factors of successfully measuring the neutron Electric Dipole Moment (nEDM) at TRIUMF. Those include having a very stable magnetic field environment as well as a very high density Ultra Cold Neutron (UCN) source.

For the future nEDM measurement at triumf several types of shielding will be used. Magnetic shielding is vital to create a quiet magnetic environment. An important component of the magnetic shielding system is the large magnetic shields that are made of highly permeable materials. A prototype of such shields exists at the University of Winnipeg. the first half of the thesis is related on magnetic field stability studies on the prototype shields at the University of Winnipeg.

The The second half of the thesis is dedicated to the UCN production and analysis at TRIUMF using the vertical UCN cryostat which was previously used at RCNP (reference).

1.1 History of Fundamental Symmetries

Over the last few decades the interest in the invariance of the discrete symmetries have been increased. Such studies revealed the internal structure of the elementary particles and helped develop the underlying theories.

There are three significant symmetries in physics as Charge conjugation (C), Parity (P) and Time-reversal (T). C-symmetry simply decribes physical laws under a charge-conjugation transformation. Parity transformation, is simply the inversion of spatial coordinates and Time-reversal transformation is changing the direction of time. Tests of Charge C,P and T symmetries established the structure of the Standard Model (SM) [17].

In 1956, fall of discrete symmetries started with the famous $\theta - \tau$ paradox in the K-mesons decay. Yang and Lee suggested that the paradox is originated from a P violation in the weak interactions [18]. Immediately after, an experimental search was suggested by Ramsey for Parity violation in the β decay of Co-60. Within a few months, P violation was demonstrated by three different experiments [19–21]. After the observation of P violation, Landau showed that Electric Dipole Moments (EDMs) are forbidden by T symmetry [22] and then it was suggested that T symmetry should also be checked experimentally [23].

One of the most fundamental symmetries in physics is the CPT (Charge-Parity-Time) symmetry. The simultaneous operation of of C, P and T leaves the system unchanged.

	C	P	T
B	-	+	-
E	-	-	+
$\boldsymbol{\mu}$	-	+	-
d	-	+	-

Table 1.1: Symmetry properties of different components of the EDM Hamiltonian

To date there is no experimental evindence for CPT symmetry breaking. Because of the CPT invariance, breakdown of CP symmetry should be accompanied by violation of Time-reversal symmetry.

A finite EDM provides a good source of CP violation. EDMs caused by CP violation in the SM are negligible. But most extensions of SM such as supersymmetry naturally produces EDMs that are comparable to or larger than present experimental limits [24]. The search for EDMs can be traced back to 1950 when Purcell and Ramsey tested the possibility of finding EDMs for particles and nuclei. Smith, Purcell and Ramsey started an experiment to search for neutron EDM d_n and they achieved the upper limit of $d_n < 5 \times 10^{-20}$ e $\cdot$ cm [25]. Over the years the upper limit on the neutron EDM has been improved by many orders of magnitude. Measurement of particle EDMs provide some of the tightest constraints on extensions to the SM to probe CP violation. The most recent upper limit on the neutron EDM is found to be $|d_n| < 3.0 \times 10^{-26}$ e$\cdot$ cm [26].

1.2 Neutron Electric Dipole Moment

A permanent neutron electric dipole moment is an intrinsic property of a neutron. This fundamental property is a measure for the separation of positive and negative charges internal to the neutron. However no nEDM has been measured so far.

The interaction of a nonrelativistic neutron with the electromagnetic field can be descibed by the follwoing hamiltonian:

$$H = -\boldsymbol{\mu_n} \cdot \mathbf{B} - \mathbf{d_n} \cdot \mathbf{E} \tag{1.1}$$

where $\boldsymbol{\mu}_n$ is the magnetic moment of the neutron interacting with the magnetc field $\mathbf{B}$ and $\mathbf{d_n}$ is the electric dipole moment of the neutron interacting with the electric field $\mathbf{E}$.

The properties of the Hamiltonian under discrete symmetries is summarized in table. 1.2. Based on this, the first term is CP-even and T-even and the second term is *cp*-odd and T-odd where both terms are CPT-invariant. Therefore, a nonzero EDM may exists if both Parity and Time-reversal symmetries are broken.

1.2.1 Baryon Asymmetry of the Universe

The neutron EDM provides a highly sensitive diagnostic for CP violation which is an important element for the observed baryon asymmetry in the universe. The dominance of matter over antimatter in the universe can be characterized by [27]

$$\eta = \frac{n_b - \bar{n_b}}{n_\gamma} \simeq 6 \times 10^{10} \tag{1.2}$$

where n_b is the number of baryons, $\bar{n_b}$ is the number of anti-baryons and n_γ is the number of photons in the Cosmic Microwave Backgorund.

It is possible to assume that maybe the universe is baryon symmetric in a very large scale and it is split into regions that are made of only baryons or anti-baryons. If that was the case, an excess of gamma rays in between these separated regions was expected due to annihilation. But, even in the least dense regions of the space, there is hydrogen gas cloud.

Sakharov criteria

There are three ingredients needed to create baryon asymmetry known as Sakharov conditions [28]:

- Baryon number violation
- C(Charge) and CP(Charge-Parity) violation
- Departure from thermal equilibrium.

The first condition is obvious which means in a reaction, if the net baryon number is zero, there would be no baryon asymmetry. In the reactions that violate baryon number, if there is no C and CP violation, the net baryon number would be zero [29]. The third condition is essential for a net nonzero baryon asymmetry since the equilibrium average of B vanishes. Sakharov suggested that baryogenesis took place immediately after the big bang, at a temperature not far below the Planck scale of 10^{19} GeV, when the universe was expanding so rapidly that many processes were out of thermal equilibrium [30].

1.2.2 The nEDM Measurement Technique

1.2.3 neutron Electric Dipole Moment Status Worldwide

The most recent neutron electric dipole moment measurement at ILL found that be $d_n < 3.0 \times 10^{-26}$ e·cm (90% CL) [26]. The new ^{199}Hg EDM measurement constrains the nEDM better than direct nEDM measurements, $d_n < 1.6 \times 10^{-26}$ e·cm although subject to uncertainty from Schiff screening [31].

There are several ongoing experiments seeking to measure the nEDM. Most groups are aiming initially for an improvement of the uncertainty on d_n to the 10^{-27} e·cm level, ultimately improving to the 10^{-28} e·cm level over time.

The PSI nEDM measurement aims for a measurement at the 5×10^{-28} e·cm level [32]. (Add some detail about how they are going to measure it, what their technique is, reactor or spallation, solid deuterium or superfluid helium)

The nEDM collaboration at SNS plans to measure $d_n \approx 2 \times 10^{-28}$ e·cm, two orders of magnitude improvement from the current limit [33]. (Add some detail about how they are going to measure it, what their technique is, reactor or spallation, solid deuterium or superfluid helium)

The room temperature nEDM measurement at Munich also aims for nEDM measurement of 10^{-27} e·cm level, and is a world leader in active and passive magnetic shielding [34–37]. (Add some detail about how they are going to measure it, what their technique is, reactor or spallation, solid deuterium or superfluid helium)

(I am sure there are other places as well. They should be included here).

The nEDM experiment at TRIUMF is aiming for a determination of nEDM at the 10^{-27} e·cm level. A key factor for success is a unique high density ultracold neutron (UCN) source. The TRIUMF's approach is unique in a sense that it is the only place that is comibining a spallation method with superfluid helium for UCN production. Another novel feature is a dual comagnetometer (^{129}Xe and ^{199}Hg) to characterize systematic errors.

1.3 Ultracold Neutrons

(This section needs to be expanded) Ultracold neutrons (UCN) are neutrons with kinetic energy $\lesssim 300$ neV corresponding to velocity $\lesssim 8$ m/s or temperatures $\lesssim 3$ mK. Because of their low energy, UCN can be reflected from many materials under arbitrary angles of incident and therefore, it makes UCN storable in a material bottle. UCN are subjected to all four fundamental forces in the following ways [38–41]:

1.3.1 Ultracold Neutrons Interaction with Fundamental Forces

The Gravitational Interaction:

The interaction of UCN with the earth's gravitation field is described by

$$V_g = mgh \tag{1.3}$$

where

$$mg = 102 \text{ neV/m} \tag{1.4}$$

which is comparable to the UCN kinetic energy. This means a UCN of energy 200 neV can rise by at most 2 m.

The Weak Interaction:

UCN decay via

$$n \longrightarrow p + e^- + \bar{\nu}_e. \tag{1.5}$$

with a lifetime of 880.3 ± 1.1 S [42]. UCN can be bottled for times comparable to this time.

The Electromagnetic Interaction:

Although a neutron is electrically neutral, it possesses a magnetic dipole moment which interacts with a magnetic field **B** by the interaction

$$V_m = -\boldsymbol{\mu}_n \cdot \mathbf{B} \tag{1.6}$$

where

$$|\boldsymbol{\mu}_n| = 60 \text{ neV/T}. \tag{1.7}$$

UCN of anti-parallel spin to the magnetic field (high field seeker) have negative V_m, accelerate toward higher fields and are attracted and UCNs with parallel spin (low field seeker) have positive V_m and are repelled. If the UCN spin adiabatically traces the magnetic field, it will be fully polarized which can be achieved by passing UCN through a strong ~ 6 T magnetic field.

The strong Interaction:

The strong interaction governs the UCN interaction with material walls. It can be described by the Fermi potential V_F which arises from the coherent elastic scattering from nuclei. The highest known value ($V_F = 335$ neV) is measured for ^{58}Ni and it sets the upper limit of the UCN kinetic energy, since UCN are normally defined by the property of total reflection from materials.

1.3.2 Superthermal Sources of Ultracold Neutrons

Ultracold neutrons (UCN) move so slowly that they can populate traps made of matter, magnetic and gravitational fields. UCN can be stored and manipulated for several hundreds of seconds in such traps. Because of this property, UCN are a valuable tool for precise measurements in fundamental physics.

High precision studies of the static and decay properties of the neutron and its interactions provide important data for particle physics and cosmology. In addition, they enable sensitive searches for new physics. Examples of the experiments using UCN which aim to discover new physics are searches for a permanent electric dipole moment (EDM) of the neutron [43–47], precision measurements of the neutron lifetime [48–52], and β-decay correlation parameters [53, 54], as well as quests for dark matter candidates [55**?** , 56], axion-like particles [57**?** –59], Lorentz invariance violations [60] and the measurements of the quantum states of UCN in the gravitational field of the earth [61].

The search for a nonzero neutron EDM provides a promising route to investigate new mechanisms of CP violation beyond the standard model. These in theory could help explain the matter-antimatter asymmetry in the Universe. At the present best level of sensitivity $d_n = 3.0 \times 10^{-26}$ e·cm (90% C.L) [47] which was limited by counting statistics, severe constraints on new sources of CP violation were placed.

The prospect to make an important discovery in refining the neutron EDM search has strongly motivated many research groups to develop next generation UCN sources [62, 63] which aim to improve the available UCN densities by more than 2 orders of magnitude.

1.3.3 Properties of UCN

UCN have velocities less than 8 m/s and energies about 260 neV which corresponds to temperatures below 2 mK. The kinetic energy of UCN is less than the neutron optical potential of well-chosen materials and so they can reflect from material surfaces at all incident angles, allowing them to be stored in a vessel and studied for times approaching the neutron lifetime.

The neutron is an electrically neutral hadron and participates in all of the four fundamental interactions as described below.

The Gravitational Interaction

The neutron has a mass $m_n \approx 940$ MeV/c^2 and therefore has a potential in the Earth's gravitational field

$$V_g = m_n g h = (102 \text{ neV/m})h \tag{1.8}$$

where h is the vertical displacement and $g = 9.8$ m/s^2 is the acceleration due to the earth's gravitational field.

UCN with the kinetic energies < 260 neV can go < 2.5 m high. This may be contrasted with the case for cold neutrons at 20 K which have velocities ∼600 m/s.

The Nuclear Weak Interaction

In the standard β-decay of a neutron, the neutron decays into a proton, an electron and an electron antineutrino:

$$n \to p + e^{-} + \overline{\nu_e}. \tag{1.9}$$

The value of neutron lifetime sets the maximum time constant with which UCNs can be stored for. The current value of the neutron lifetime is 880.3 ± 1.1 s [64]. Other loss processes are described in Sec. 1.4.1.

The Electromagnetic Interaction

The neutron is an electrically neutral, spin-1/2 particle that possesses a magnetic dipole moment due to its internal structure including electrically charged quarks. The magnetic moment is antiparallel to the spin of the neutron; its magnitude is $\mu_n = 60.3$ neV/T.

When the neutron experiences an external magnetic field $\boldsymbol{B}$, its spin has two possible eigenstates with their interaction energy given by:

$$V_{mag} = -\mu_n \cdot \boldsymbol{B} = \pm(60.3\text{neV/T})|B| \tag{1.10}$$

where the higher interaction energy (i.e. positive value) is for the neutron spin parallel to the external field (and thus magnetic moment anti-parallel) and the lower interaction energy is for the neutron spin anti-parallel (magnetic moment parallel) to the external field. If the magnetic field $\boldsymbol{B}$ is inhomogeneous and the neutron spin traces the magnetic field adiabatically, the neutron will experience a force given by:

$$\boldsymbol{F}_{mag} = -\nabla V_{mag} = \pm\mu_n \nabla |\boldsymbol{B(r)}|. \tag{1.11}$$

The neutrons that experience a force towards regions of higher magnetic field strength are called high-field seekers. Conversely if the neutrons experience a force towards regions of lower magnetic field (a 3D minimum in the $\boldsymbol{B}$ field) strength they are called low-field seekers. It is this force that allows UCN with sufficiently low energy to be confined by magnetic field gradients. Furthermore, Nuclear Magnetic Resonance (NMR) experiments can be conducted on UCN. For example, NMR is used to measure the EDM of neutrons (the Ramsey technique) where UCN are placed in aligned electric and magnetic fields.

The Nuclear Strong Interaction

The strong interaction governs the UCN interaction with the material walls. Neutrons can be totally reflected from material surfaces under grazing angles of incidence. To each material, a critical angle for total reflection exists. This angle becomes larger for smaller neutron velocities. The reflection is caused by coherent elastic scattering of the neutron with material walls which can be described by the neutron optical potential. The highest known value of the neutron optical potential is measured for ^{58}Ni (335 neV) and it sets the upper limit of the UCN kinetic energy, since UCN are normally defined by the property of total reflection from materials at all angles of incidence.

1.4 Superthermal UCN sources

In 1975 it was shown that, it is possible to achieve higher steady state UCN densities corresponding to temperatures much lower than the temperature of the moderator [62]. These are called superthermal converters. Here thermal or cold neutrons are inelastically scattered and transfer their kinetic energy to an excitation of the converter medium (e.g. to a phonon).

In contrast, in thermal UCN sources neutrons are extracted from a distribution almost in thermal equilibrium with a moderation system. The UCN turbine source at the Institute Laue-Langevin (ILL) extracted very cold neutrons vertically from a cold source (liquid deuterium) and slowed them down using the mechanical action of a turbine [65, 66]. Here cold neutrons with velocities of $\sim$ 40 m/s are decelerated by reflection from a set of curved turbine blades moving with a velocity $\sim$ 20 m/s in the same direction as the neutrons. A UCN density $\sim$ 40 UCN/cm^3 was achieved with this method [67**?**]. current UCN density of this source is 110 UCN/cm^3 for neutrons with velocities $<$ 7m/s[65].

1.4.1 Basic Idea of Superthermal UCN Sources

The mechanism of a superthermal UCN source is the following. An incident neutron can lose almost its entire energy in a single scattering event by creating excitations (*e.g.* phonons) in a converter medium [62**?**]. because of the loss in the kinetic energy, this process is called downscattering. The reverse process is called upscattering where a UCN absorbs kinetic energy from the medium. Consider a simple model for the medium as a two-level system with an energy gap E_0^*. The principle of detailed balance links the cross-section for upscattering $\sigma(E_{UCN} \rightarrow E_{UCN} + E_0^*)$ and downscattering $\sigma(E_{UCN} + E_0^* \rightarrow E_{UCN})$ [**?**]

$$\sigma(E_{UCN} \rightarrow E_{UCN} + E_0^*) = \frac{(E_{UCN} + E_0^*)}{E_{UCN}} e^{-\frac{E_0^*}{k_B T}} \sigma(E_{UCN} + E_0^* \rightarrow E_{UCN}) \tag{1.12}$$

where T is the temperature of the medium, E_{UCN} is the energy of the UCN, and k_B is the Boltzmann factor.

In general $\sigma(E_{UCN} + E_0^* \rightarrow E_{UCN})$ is practically independent of T so that for $E_0^* \gg k_B T \gg E_{UCN}$ the upscattering cross-section for UCN can be made arbitrarily small by decreasing the temperature. If the converter is now placed in a neutron flux at a temperature $T_n \geq E_0^*$ there will be a significant number of downscattering events and a negligible number of upscattering events.

If the converter is contained in a vessel whose walls are good UCN reflectors with potential $V \gg V_m$ where V_m is the UCN potential of the converter, and the walls are transparent to the neutrons of energy E_0^*, then UCN will build up in the moderator to a density until the rate of loss is equal to the rate of UCN production.

The steady state UCN density in the source is given by

$$\rho_{\mathrm{UCN}} = P_{\mathrm{UCN}} \tau \tag{1.13}$$

where P_{UCN} (UCN/cm^3·s) is the UCN production rate and τ (s) is the UCN mean lifetime in the system. The mean lifetime τ of the UCN in the vessel is restricted by a variety of possible loss mechanisms

$$\frac{1}{\tau} = \frac{1}{\tau_a} + \frac{1}{\tau_W} + \frac{1}{\tau_{up}} + \frac{1}{\tau_\beta} \tag{1.14}$$

where $1/\tau_a$ is the UCN absorption rate in the medium, $1/\tau_W$ is the rate of the UCN loss on the walls, $1/\tau_{up}$ is the neutron loss due to the upscattering in the medium and $1/\tau_\beta$ is the β-decay losses.

Pure deuterium and liquid ^{4}He are good candidates for superthermal conductors, possessing a balance of high production rate and small neutron absorption cross-section and upscattering rate.

1.4.2 UCN Production by Superfluid ^{4}He

Superfluid ^{4}He Definition

^{4}He is an isotop of helium with two protons and two neutrons with an integer spin of zero which makes it a boson. As a result, it follows the Bose-Einstein statistics. It has two liquid states known as He-I and H-II. The He-I phase is the normal fluid phase and He-II is the superfluid phase with zero viscosity and zero entropy. Fig. 1.1 shows the phase transition diagram of of ^{4}He. These two phases are separated out by the λ-line. The phase transition happens at 2.172 K. Below the lambda line the liquid can be described by the so-called two-fluid model which consists of both phases. Below 1 K the liquid is mostly superfluid.

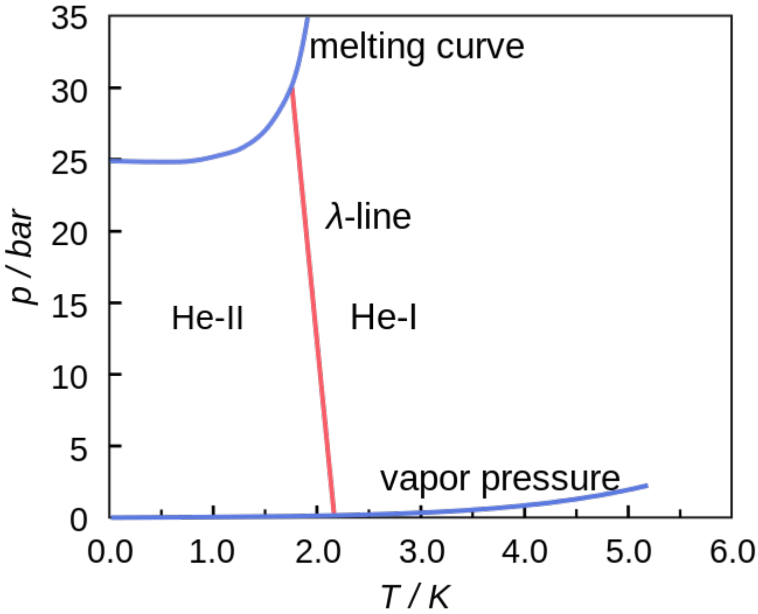

Figure 1.1: The phase diagram of ^{4}He. Here the normal fluid phase or He-I and the superfluid phase or H-II are shown.

Because of its zero viscosity, superfluid helium has the ability to flow through very small capillaries or narrow channels without experience any friction at all. The flow of liquid helium along the surface is called *film flow*.

Superfluid Helium Converter

The superfluid ^{4}He is an attractive candidate as a UCN source and was studied in Ref. [68]. It has zero neutron absorption cross-section resulting in $\tau_a \rightarrow \infty$ which makes it a good candidate as a UCN source. In superfluid helium, upscattering losses become smaller than β-decay losses below $T \sim 0.7$ K. The dominant production mechanism is the excitation of a single phonon at the crossing of the free neutron and phonon dispersion curves, with a momentum $q \sim 0.7/\text{Å}$ [69] and energy 1 meV corresponding to a neutron wavelength 8.9 Å. The availability of 8.9 Å cold neutrons is crucial and their flux must be maximized. There are two types of UCN sources based on superfluid helium: sources where experiment and source are combined in one apparatus and the measurement is performed inside the superfluid helium, and extracted-UCN sources where the source is an apparatus on its own and delivers neutrons to experiments at room temperature connected to it by UCN guides.

UCN Production Rate with Single Phonon scattering in Superfluid helium [5, 6, 68]

UCN can be produced by one phonon excitation in superfluid helium when the energy of the incident neutrons is equal to that of the one phonon excitation in the medium. The incident neutrons then scatter down to UCN by creating one-phonon excitations in the converter medium. Fig. 1.2 shows the dispersion relation of the superfluid helium and a

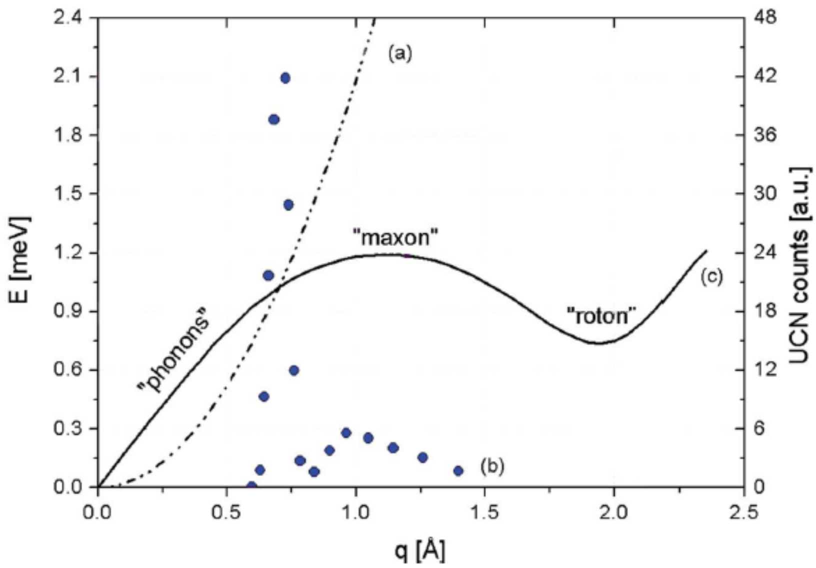

Figure 1.2: [4] Dispersion relation of superfluid helium (c) and of the free neutron (a). Neutrons with $E \simeq 1$ meV and wavenumber $q \simeq 0.7/\text{Å}$ can excite a single phonon with the same energy and momentum and be downscattered to UCN energy range. The UCN production rate (b)(circles) shows the dominance of this single phonon process with respect to multiphonon processes at higher momentum q.

free neutron. A neutron at rest can absorb energy $\hbar\omega$ and momentum $\hbar q$ with

$$\omega = \frac{\hbar q^2}{2m} \tag{1.15}$$

where m is its mass and a neutron with this energy and momentum can come to rest after transferring its energy and momentum to the superfluid ^{4}He. For single phonon interactions, which are usually dominant, the superfluid can only exchange quantities of energy and momentum that are related by the dispersion curve

$$\omega = \omega(q) = cq \tag{1.16}$$

where ω is the energy of the phonon, q is the phonon's momentum, and c is the speed of sound in the moderator. The second equal sign in Eqn. (1.16) is an approximation to simplify the discussion. The neutrons can only come to rest by emission of a single phonon if they have the resonant energy E_0^* given by the intersection of Eqns. (1.15) and (1.16)

$$\omega(q) = cq = \frac{\hbar q^2}{2m} \tag{1.17}$$

and so

$$q^* = \frac{2mc}{\hbar}. \tag{1.18}$$

The differential cross-section for neutron scattering is given by the dynamic scattering function $S(q,\omega)$ which is the Fourier transform of the Van Hove correlation function $G(r,t)$ in space and time of the superfluid helium [70]:

$$\frac{d\sigma}{d\omega} = b^2 \frac{k_2}{k_1} S(q,\omega) d\Omega \tag{1.19}$$

where b is the bound neutron scattering length for ^{4}He, $\hbar k_1$ is the momentum of the incident neutrons and $\hbar k_2 = \hbar k_{\mathrm{UCN}}$ is the momentum of UCN. The quantity $S(q,\omega)$ has been measured in great detail [71**?** , 72]. Performing the change of variables,

$$d\Omega = 2\pi \sin\theta d\theta = 2\pi \frac{qdq}{k_1 k_2} \tag{1.20}$$

gives

$$\frac{d\sigma}{d\omega} = 2\pi b^2 \frac{k_2}{k_1} S(q,\omega) \frac{qdq}{k_1 k_2} = 2\pi b^2 S(q,\omega) \frac{qdq}{k_1^2}. \tag{1.21}$$

This may effectively be integrated over the limits on q which are

$$k_1 - k_2 < q < k_1 + k_2. \tag{1.22}$$

Since

$$k_2 = k_{\mathrm{UCN}} \ll k_1, \quad q \sim k_1 \tag{1.23}$$

we may write $dq = 2k_{\mathrm{UCN}}$. This results in the cross-section being related to $S(q,\omega)$ evaluated on the incident neutron's dispersion curve:

$$\frac{d\sigma}{d\omega} = 4\pi b^2 \frac{k_{\mathrm{UCN}}}{k_1} S\left(k_1, \omega = \frac{\alpha k_1^2}{2}\right), \tag{1.24}$$

where $\alpha = \frac{\hbar}{m} = 4.14$ meV/Å^2 and $S(q,\omega)$ assumed to be constant over the narrow range dq. The approximation

$$\omega = \frac{\hbar(k_1^2 - k_2^2)}{2m} = \frac{\alpha}{2}(k_1^2 - k_2^2) \approx \frac{\alpha}{2} k_1^2 \tag{1.25}$$

has also been used.

The UCN production rate is given by

$$P(E_{\mathrm{UCN}})dE_{\mathrm{UCN}} = N_{He}\int \frac{d\Phi(E_1)}{dE}\cdot\frac{d\sigma}{d\omega}(E_1 \to E_{\mathrm{UCN}})dE_1 dE_{\mathrm{UCN}} \tag{1.26}$$

where $\frac{d\Phi(E_1)}{dE}$ is the differential incident neutron flux, N_{He} is the atomic density in the liquid helium and $\frac{d\sigma}{d\omega}(E_1 \to E_{\mathrm{UCN}})$ is the energy differential cross-section for the inelastic neutron scattering or the probability of the incident neutrons with energy E_1 to scatter from the helium nucleus and become UCN. Then

$$\begin{aligned}\int_0^{E_c} P(E_{\mathrm{UCN}})dE_{\mathrm{UCN}} &= N_{He}4\pi b^2\alpha^2\left[\int \frac{d\Phi(k_1)}{dE}S\left(k_1,\omega=\frac{\alpha k_1^2}{2}\right)dk_1\right]\int_0^{k_c} k_{\mathrm{UCN}}^2 dk_{\mathrm{UCN}} \\ &= N_{He}4\pi b^2\alpha^2\left[\int \frac{d\Phi(k_1)}{dE}S\left(k_1,\omega=\frac{\alpha k_1^2}{2}\right)dk_1\right]\frac{k_c^3}{3}\ \mathrm{UCN/cm^3s},\end{aligned} \tag{1.27}$$

where E_c and k_c are the critical UCN energy and wave vector of the walls of the storage chamber. This way of writing the UCN production rate is more general and it is useful to calculation single phonon and multiphonon contributions to the UCN production rate. The one phonon production rate is found by evaluating Eqn. (1.27) over the one phonon peak ($q^* = 0.7/\text{Å}$). Thus

$$P_{\mathrm{UCN}} = 9.44\times 10^{-9}\frac{d\Phi(E_1^*)}{dE_1^*}\ \mathrm{UCN/cm^3} \tag{1.28}$$

where E_1^* is the energy of the incident neutrons at the one phonon peak.

Multiphonon Scattering Contribution in UCN Production in Superfluid helium [5, 6]

For polychromatic neutron sources, UCN can also be produced by multiphonon processes in superfluid ^{4}He. Multiphonon production of UCN with various energy spectrum of the neutron flux has been studied in Ref. [6]. Fig. 1.3 shows the energy spectrum of neutron flux $\frac{d\phi}{dE}$ for three sources as a function of momentum q and are compared to the dynamic scattering function $S(q, \omega = \hbar q^2/2m)$. The peak at $q = 0.7/\text{Å}$ corresponds to the one phonon excitation by superfluid helium. The values of S above $1.2/\text{Å}$ are extrapolated. The value of S above $2/\text{Å}$ are essentially zero. The UCN production from one phonon and multiphonon processes have been calculated for three input neutron spectrums: SNS ballistic guide, PULSTAR MC flux and HMI polarized flux. The multiphonon contribution to UCN production is calculated by using Eqn. (1.27) and calculating $\int \Phi(E_1)S(k_1, \omega = \frac{\alpha k_1^2}{2})dk_1$. The result showed that, for sources where helium is exposed to the total thermal flux or at a dedicated spallation source, the multiphonon contribution can amount to slightly more than a factor of 2 increase in the UCN production.

UCN production by multiphonon emission in superfluid helium under pressure was studied in Ref. [5]. The dynamic scattering function $S(q, \omega)$ of the superfluid helium strongly depends on pressure, leading to a pressure-dependent differential UCN production rate. The expression for the multiphonon part of S describing UCN production was derived from inelastic neutron scattering data. Application of pressure to superfluid

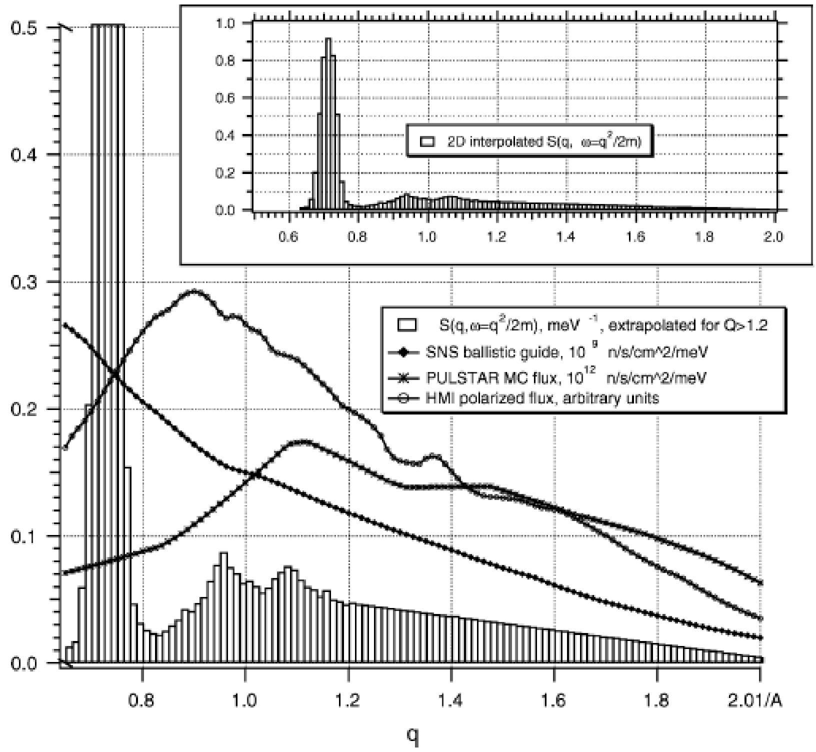

Figure 1.3: The energy spectrum of the incident cold neutron flux from three sources compared to the dynamic scattering function $S(q, \omega = \frac{\alpha k_1^2}{2})$ /meV as a function of q /Å.

helium increases the velocity of sound, such that the dispersion curves of the ^{4}He and of the free neutron cross at shorter neutron wavelength.

Since for neutron beams from a liquid deuterium cold source, the differential flux density $\frac{d\Phi}{dE}$ in the range 8-9 Å normally increases for decreasing wavelength of the cold neutron flux, and also since pressure increases the density of He-II, it was expected to observe an increase in the single phonon UCN production rate, and different multiphonon contribution with pressure increase. It was observed that, both the single and the multiphonon scattering functions change with pressure. The single phonon excitation moves to a shorter wavelength (see Fig. 1.4) and the value for S decreases. It leads to a reduction in one-phonon UCN production. The multiphonon excitations increase with pressure and the peak of the scattering function S moves to shorter incident-neutron wavelengths, see Fig. 1.4. However the UCN production rate decreases with pressure increase. Only if the cold neutron flux at 8.3 Å exceeds by more than 2.5 times that at 8.9 Å, an increase in the UCN production rate may be expected. However, it has to be considered that the application of pressure requires a window for UCN extraction which causes severe UCN losses. Therefore, UCN production in superfluid helium under pressure was concluded not to be attractive.

UCN upscattering and UCN lifetime in superfluid helium [73]

Superfluid ^{4}He has a zero neutron absorption cross-section and if the converter is kept at sufficiently low temperatures (typically $\lesssim 1$ K), thermal upscattering of UCN is suffi-

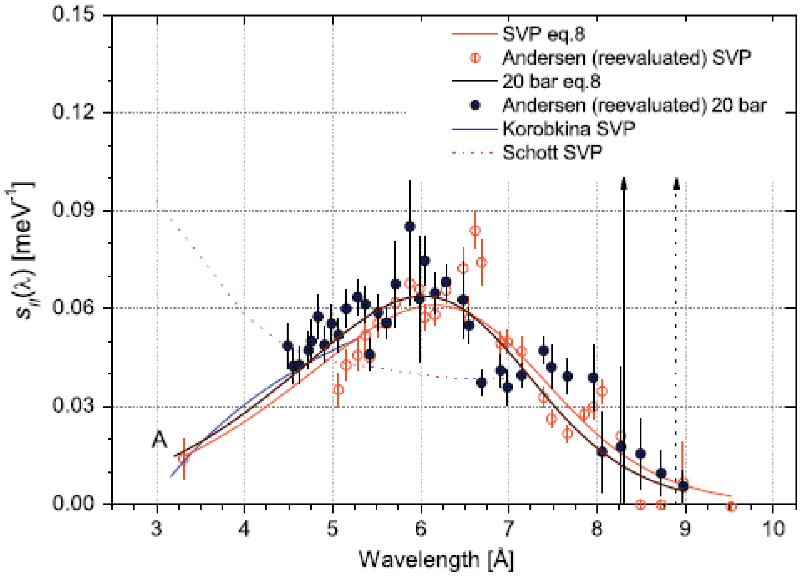

Figure 1.4: [5] Multiphonon scattering function at SVP (Saturated Vapour Pressure) and 20bar. The extrapolation to short wavelength of Korobkina *et al.* [6] at SVP is linear in k, whereas the calculation of Schott *et al.* [7] is based on the static structure factor of the superfluid helium. The data point (A) is taken from Ref. [8]. The one-phonon peaks are indicated by vertical arrows: SVP (dotted line) and 20bar (solid line).

ciently suppressed. This allows the produced UCN to survive in the converter for times dominated by the wall losses of the vessel, typically >100 s [73].

The upscattering of neutrons is caused by the interactions between a neutron at rest and excitations in superfluid helium at different temperatures. These excitations can be categorized in three groups: one phonon absorption, two-phonon scattering, and roton-phonon scattering. The total upscattering rate can be written as

$$\frac{1}{\tau_{up}} = \frac{1}{\tau_{1-ph}} + \frac{1}{\tau_{2-ph}} + \frac{1}{\tau_{rot-ph}} \tag{1.29}$$

where,

$$\frac{1}{\tau_{1-ph}} = Ae^{-(12K)/T} \tag{1.30}$$

is the one phonon absorption contribution,

$$\frac{1}{\tau_{2-ph}} = BT^7, \tag{1.31}$$

is the two-phonon scattering contribution (one phonon absorbed and one phonon emitted), and

$$\frac{1}{\tau_{rot-ph}} = CT^{3/2}e^{-(8.6K)/T}, \tag{1.32}$$

is the contribution from roton-phonon scattering with the absorption of one roton followed by a phonon emission.

The values of A, B and C are extracted from data for temperatures up to 2.4 K [73]. The comparison between the UCN production and upscattering rate to the theoretical temperature dependence of these processes showed that the main contribution is from two-phonon scattering $\frac{1}{\tau_{up}} = BT^7$ with $B = (4 - 16) \times 10^{-3}$ /(s K^7) [73].

1.4.3 UCN production by Solid Deuterium

Solid deuterium (sD_2) is a material with small absorption cross-section, small incoherent scattering cross-section (to minimize upscattering), and the presence of numerous phonon modes which can inelastically scatter neutrons down to UCN energies. A converter based on sD_2 should be operated at temperatures below 10 K in order to avoid subsequent upscattering of UCN by phonons within solid deuterium.

Solid deuterium has an almost perfect hcp crystal structure, when prepared under suitable conditions (low pressure and $T > 5$ K). The D_2 molecule has internal rotational modes which are described by the rotational quantum number J. The rotational excitations give rise to additional modes in the solid deuterium. J is still a good quantum number. Deuterium in the states with even J is called ortho-deuterium (o-D_2) whereas deuterium in the states with odd J is called para-deuterium (p-D_2). An increase of the concentration of the p-D_2 molecules leads to a larger neutron upscattering rate. Theoretically and experimentally it has been shown that sD_2 at sufficiently low temperatures (around 5K) with high enough purity and with high ortho concentration can be used to produce a high density UCN [**?**].

UCN Production Cross-Section and UCN Production Rate in Solid Deuterium [10, 74?]

The formula for the UCN production in solid deuterium is very similar to that of the superfluid helium shown in Eqn. (1.26) with replacing ^{4}He atomic density N_{He} with molecular density of solid deuterium N_{D_2} and noting that in sD_2 the neutron scattering cross-section may be written as a sum of coherent and incoherent contributions:

$$\frac{d\sigma}{d\omega} = \left[\frac{k_2}{k_1} b_{\rm coh}^2 S_{\rm coh}(q,\omega) + \frac{k_2}{k_1} b_{\rm inc}^2 S_{\rm inc}(q,\omega) \right] d\Omega. \tag{1.33}$$

In Ref. [10] the UCN production cross-section σ was determined by two ways. One way is the determination of the quasi-particle (phonons and rotational excitations of the D_2 molecule) density of states $G_1(E)$ (incoherent approximation) from the measured neutron cross-section $\frac{d\sigma}{d\omega}$ and the other method is the direct integration of the dynamical neutron cross-section $\frac{d\sigma}{d\omega}$ ($\hbar = 1$) in the kinematical region along the free-neutron dispersion parabola.

UCN production cross-section: Incoherent approximation. With the knowledge of the quasi-particle density of states $G_1(E)$, it is possible to calculate the dynamical neutron cross-section $\frac{d\sigma}{d\omega}$ (averaged over the scattering angle, thus q). Vice versa it is also possible to extract $G_1(E)$ from a measured dynamical neutron cross-section [75]. If $G_1(E)$ is known, it is possible to calculate one-phonon and multiphonon contributions to the neutron cross-section $\frac{d\sigma}{d\omega}$.

The method for the determination of $G_1(E)$ from the measured neutron scattering data in solid deuterium is studied in Ref. [74]. In the determination of $G_1(E)$, contributions of higher order multiphonons to $\frac{d\sigma}{dE}$ are incorporated.

In the case of UCN production the energy transfer of the downscattered neutron $E = E_1 - E_{\mathrm{UCN}}$ is approximately equal to the initial neutron energy E_1 ($E_{\mathrm{UCN}} \ll E_1, E_{\mathrm{UCN}}$: UCN energy). The total cross-section for UCN production can be calculated by

$$\sigma_{\mathrm{UCN}}(E_1) = \int_0^{E_{\mathrm{UCN}}^{max}} \frac{d\sigma(E_1)}{dE} dE_{\mathrm{UCN}}. \tag{1.34}$$

The calculated cross-section is shown in Fig. 1.5 is in agreement with data on UCN production using a cold neutron beam ($E_1 \sim 1.4$ meV to 20 meV). Here the one-quasi-particle and two-quasi-particle excitations are included in the calculations. The UCN production cross-section is mainly determined by one-quasi-particle excitation for energies below 15 meV. The two-quasi-particle contribution is non-negligible in the region of 5-25 meV.

The application of the incoherent approximation in the case of sD_2 has certainly to be questioned since the sD_2 crystal scatters neutrons more coherently than incoherently.

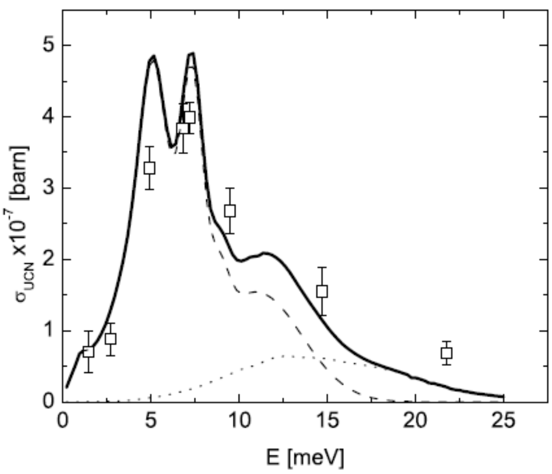

Figure 1.5: UCN production cross-section of sD_2 with 98% ortho concentration. UCN energy range 0-150 neV inside the solid D_2. Solid line: cross-section calculated in incoherent approximation. Dashed line: one-quasi-particle contribution. Dotted line: two-quasi-particle contribution. □: data from measurements at PSI [9].

UCN production cross-section: Direct determination. The easiest way of determining the cross-section for UCN production is the use of the dynamical scattering function $S(q,\omega)$ in the (q,ω)-phase space along the free-neutron parabola, as shown schematically in Fig. 1.6.

This method allows the incorporation of all the coherent and incoherent contributions to the UCN production cross-section. Possible coherent contributions, which cannot be treated exactly with the incoherent approximation, appear directly in the deduced cross-section. Therefore, this method is superior in principle to the result obtained by the incoherent approximation.

The UCN production cross-section can be determined by

$$\sigma_{\mathrm{UCN}}(E_1) = \frac{\sigma_1}{k_1} S(k_1, E_1) \frac{2}{3} k_{\mathrm{UCN}}^{max} \, E_{\mathrm{UCN}}^{max} \tag{1.35}$$

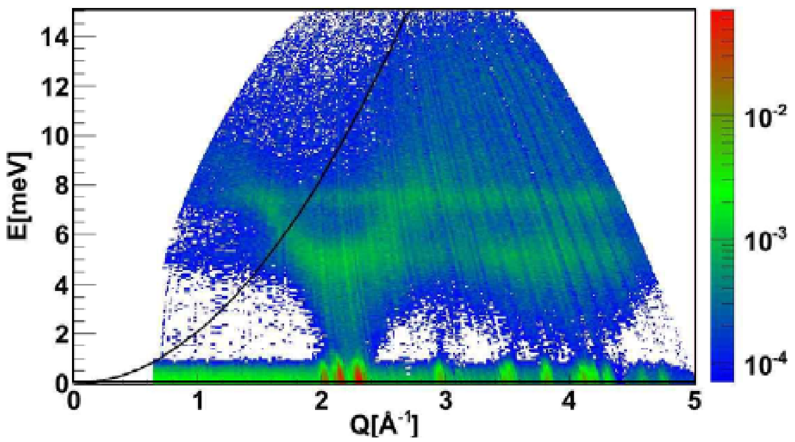

Figure 1.6: [10] $S(q, \omega)$ ($q = Q, \omega = E$) (arb. units) of 95.2% solid o-D_2 at $T = 4$ K. Data from IN4 measurements. Black parabola: dispersion of the free neutron.

where E_1 is the energy of the incoming neutrons in the downscattering process, σ_1 is a constant and $k_{\rm UCN}^{max}$ and $E_{\rm UCN}^{max}$ are the upper limits for the UCN momentum and energy. In order to obtain absolute cross-sections, $S(q, \omega)$ has to be calibrated to absolute values. The result of this calibration and the determination of the UCN production cross-section as a function of the energy of the incoming neutrons, and a comparison with the measurements of this cross-section is shown in Fig. 1.7. This plot also contains the data, which were obtained with higher incoming-neutron energy ($E_1 = 67$ meV).

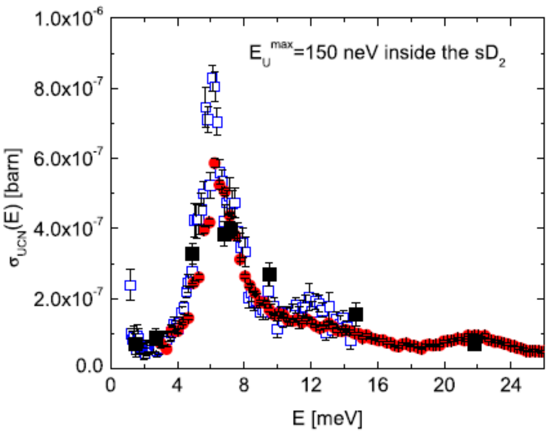

Figure 1.7: [10] UCN production cross-section solid o-D_2 of 95.2% [10]. A UCN energy range of 0-150 neV inside the solid D_2 is assumed. Sample: fast frozen solid deuterium ($T = 4$ K); data from IN4 measurements. Blue □: $E_0 = 17.2$ meV. Red filled ◯: $E_0 = 67$ meV, ■: direct UCN production data from measurements at PSI [9].

The comparison of the calculated UCN production cross-section, extracted from the incoherent approximation and parabola method, shows (see Fig. 1.5 and Fig. 1.7) a discrepancy in the region of $E \sim 6$ meV. The cross-section determined by the parabola method shows a pronounced maximum in the region of $E \sim 6$ meV as compared to the incoherent approximation result. This peak corresponds to the coherent phonon contribution to the UCN production cross-section. The double-peak structure in the UCN production cross-section by the incoherent approximation is not present in Fig. 1.7 and cannot be reproduced by the measured data shown in Figs. 1.5 and 1.7. This means, a new experiment at a more intense cold neutron beam with a better energy resolution would be desirable to study this effect further.

In Fig. 1.6, the parabola of the free neutron crosses the acoustical phonon dispersion curve at $E \sim 6$ meV. At this point, the UCN production cross-section is predominantly determined by coherent scattering. This can explain a deviation from the production cross-section in incoherent approximation. Nevertheless the general agreement of the incoherent approximation with the PSI data is remarkable (as shown in Fig. 1.5).

The result for the calculated UCN production rate in solid o-D_2, exposed to a Maxwellian shaped neutron flux for different effective neutron temperatures is shown in Fig. 1.8. The main conclusion from these results was the new understanding of possible higher energetic loss channels (one-quasi-particle and two-quasi-particle) in solid deuterium for the downscattering of cold neutrons in the conversion process to UCN. The best value for the effective neutron temperature is in the region of $T_n \sim 40$ K which is larger than what was previously expected ($T_n \sim 30$ K [**?**]).

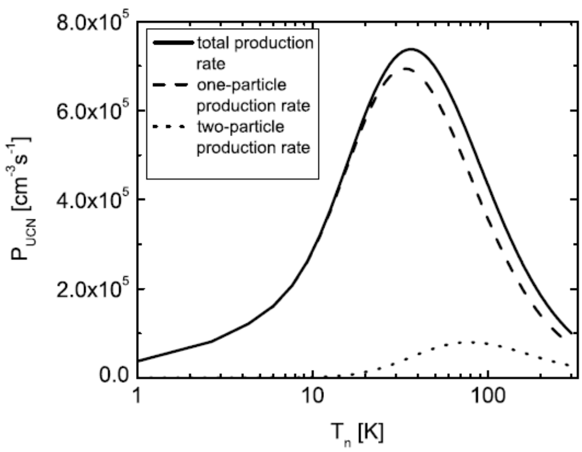

Figure 1.8: [10] Calculated UCN production rate of sD_2 with 98% ortho concentration for different Maxwellian neutron spectra with effective neutron temperature T_n. UCN energy range:0-150 neV inside the sD_2. Neutron capture flux 10^{14} /cm^{2}s. Solid line: total production rate (one- and two- particle excitations). Dashed line: one-particle production rate. Dotted line: two-particle production rate.

UCN upscattering and UCN lifetime in sD_2 [11, 76]

The different molecular species ortho-D_2 and para-D_2 have significantly different UCN-phonon annihilation cross-sections [76]. The presence of even small concentrations of para-D_2 can dominate the upscattering rate which gives rise to reduced UCN lifetimes in the solid and orders of magnitude reduction in the achievable UCN density. In a D_2 solid, the populations of ortho and para states are typically determined by the ortho/para population of the gas phase before the D_2 is frozen into solid. After cooling down the D_2 to the solid phase ($T \sim 6$ K), it normally takes months to reach the equilibrium of

99.999% o-D_2. necessary to achieve UCN lifetimes comparable to the nuclear absorption time in solid deuterium, using a para-D_2 to ortho-D_2 converter is crucial.

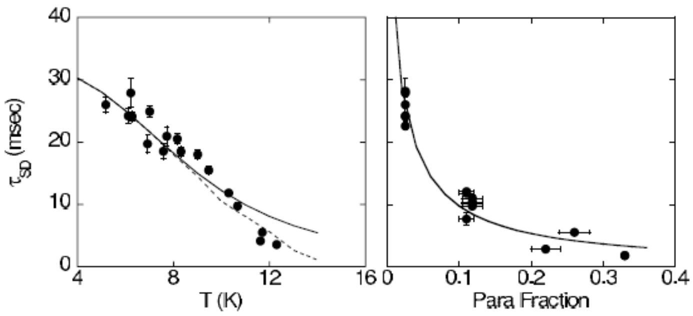

Figure 1.9: [11] Left- Data points are measured sD_2 lifetimes as a function of temperature, with the para-fraction fixed at 2.5%. Only the statistical errors are shown. Solid lines show the predicted temperature dependence. The dashed line is the predicted effect of departure from the solid lifetime model due to upscatter from D_2 gas in the guide. Right- sD_2 lifetimes as a function of para-fraction for all of the data taken below 6 K. The solid line is the model prediction of the para-fraction dependence at an average temperature of 5.6 K.

The lifetime of the UCN in sD_2 is limited by factors such as upscattering from phonons in the solid, upscattering from p-D_2 contamination and absorption inside the vessel. Reducing the time UCN spend inside the sD_2 can reduce the average absorption rate. This led to the proposal of a thin-film source where a thin layer of solid D_2 coats the inside of a storage bottle that is embedded in a cold neutron flux [77]. The possibility of a smaller source volume combined with the higher operating temperature of the thin film source offers significant technical simplification.

The UCN lifetime in the solid deuterium as a function of temperature and para/ortho fractions has been measured [11]. The total loss rate can be written as

$$\frac{1}{\tau_{SD}} = \frac{1}{\tau_{phonon}} + \frac{1}{\tau_{para}} + \frac{1}{\tau_{Dabs}} + \frac{1}{\tau_{Habs}} \tag{1.36}$$

where, $\frac{1}{\tau_{phonon}}$ is the upscattering rate from phonons in SD_2, $\frac{1}{\tau_{para}}$ is the upscattering rate from para deuterium molecules in the solid, $\frac{1}{\tau_{Dabs}}$ is the upscattering rate from the absorption on deuterium and $\frac{1}{\tau_{Habs}}$ is the upscattering rate from the absorption on the hydrogen impurities in the solid. The results for UCN lifetimes τ_{SD} in sD_2 as a function of the sD_2 temperature and para/ortho fractions are shown in Fig. 1.9. The difference between the solid and dashed line demonstrates the need to include the effect of deuterium vapor in the guide on the lifetime at higher temperatures. With this correction, the measured lifetimes agree well with theoretical predictions of the upscattering rate.

1.4.4 Comparison between sD_2 and superfluid helium sources

The main differences between sD_2 and superfluid helium sources are the UCN lifetime and the UCN production rate. While UCN can stay in superfluid helium until it β-decays, UCN in solid deuterium are absorbed by the deuteron in 150 ms after they are produced. Once a superfluid helium source is cooled down to temperatures below

Isotope	σ_a(barns)	σ_s/σ_a
^{2}D	0.000519	1.47×10^4
^{4}He	0	∞
^{15}N	0.000024	2.1×10^5
^{16}O	0.00010	2.2×10^4
^{208}Pb	0.00049	2.38×10^4

Table 1.2: Candidates for a superthermal source

0.75 K, the upscattering rate is suppressed to a level comparable to neutron β-decay. Solid deuterium has a production rate two orders of magnitude greater than superfluid helium. Therefore, solid deuterium sources output higher UCN current compared to superfluid helium sources. However, the limiting production time in superfluid helium is four orders of magnitude longer than sD_2. Thus, even with a smaller UCN production rate, superfluid ^{4}He can in principle achieve a UCN density larger than that of solid deuterium. The superthermal enhancement in solid deuterium is limited by the large nuclear absorption loss, and thus further cooling below 5 K will not significantly enhance the UCN yield.

1.4.5 Other UCN Sources [1–3]

Superthermal UCN sources may be compared by

$$\sigma_s/\sigma_a \tag{1.37}$$

where σ_s is the elastic scattering cross-section and σ_a is the absorption cross-section. At low energies (< 1 eV) $\sigma_a \sim 1/v$ where v is the speed of the neutrons. This means, the absorption cross-section is much larger at lower energies. Table 1.2 shows a list of possible superthermal UCN sources [3]. The values of σ_a are for thermal neutrons.

Solid $\alpha-^{15}N_2$ is a potential alternative to deuterium [1]. its absoption cross-section is only 5% of that of D_2, and it has a negligible incoherent scattering cross-section. Additionally, rotation of the N_2 molecules in the lattice is inhibited due to the anisotropy of the N_2 inter-molecular potential. This leads to dispersive modes for the rotational degrees of freedom (librons) which provide additional channels for neutron downscattering and eliminates the rotational incoherent upscattering. Measurements [1] show that the production cross-section peaks near 6 meV and the optimal incident cold neutron temperature is 40 K. It was found that the variation in the cross-section is no more than 18% in the range from 5 to 25 K (increasing slightly with increasing temperature). The measured cross-section was found to be somewhat lower than that of D_2 and O_2. A nitrogen-based source may benefit from operating at lower temperatures, if the upscattering cross-section can be further reduced at lower temperatures ($\sim$1 K) [1].

^{208}Pb and solid deuterium have similar nuclear absorption cross-sections. The natural solid form of ^{208}Pb would avoid the difficulties of growing cryogenic solids such as deuterium and oxygen. However, its heavy mass prevents the neutron momentum transfer to the solid phonon field. The heavy mass reduces the phonon creation cross-section by $1/M$. As a result one would expect its UCN yield to be two orders of magnitude less than solid deuterium.

As other options, the properties of the new candidate converter materials including solid heavy methane (CD_4) and solid oxygen (O_2) have been investigated in the temperature range 8 K to room temperature by measuring the production of UCN from a cold neutron beam and the cold neutron transmission through the converter materials [2]. The liquid O_2, D_2 and CD_4 have similar neutron scattering cross-sections.

^{4}He and D_2 are still the best commonly pursued options, although there is a chance that other materials could lead to a breakthrough.

1.5 Current Status of UCN sources Worldwide

1.5.1 It needs to be modified

New UCN sources using superthermal technology are under development at various laboratories across the world. Neutrons are produced by two methods: proton-induced spallation off a heavy nuclear target (e.g. tungsten), and fission where neutrons are produced by a nuclear reactor. Table 1.3 [78] shows a list of the present and future UCN sources worldwide.

Reactor sources place the moderators close to the reactor core (FRM II and Gatchina [79]) or use existing CN beam lines (ILL [80]). At FRM II, the sD_2 will be placed around a solid hydrogen cold-moderator close to the fuel element. The Gatchina superfluid ^{4}He source will be placed inside their thermal column, using immense pumping power to cool the converter to 1.1 K, making rapid extraction necessary due to increased UCN upscattering at this temperature.

The SuperSUN and SUN-2 experiments are the logical extensions of the early superthermal source geometry at ILL. A novel feature of the SuperSUN experiment at ILL [81] is a magnetic multipole reflector for a drastic enhancement of the UCN density with respect to an existing prototype superfluid-helium UCN source installed in a cold neutron beam. A multipole magnet can lead to a large gain in the saturated density of low-field-seeking UCNs because the presence of the field reduces the number of neutrons hitting the material walls and reduces the energy and wall collision rate of those that do. In addition, it acts as a source-intrinsic UCN polarizer without need to polarize the incident beam and hence avoiding associated losses.

The Los Alamos solid deuterium source [82] uses a proton beam of 900 MeV and a W target to produce neutrons. The neutrons get cooled down in a polyethylene cold moderator. The new design includes a flapper valve to isolate the neutrons from the sD_2 after the proton beam pulse.

The PSI UCN source [83] uses a 600 MeV proton beam to hit a Pb/Zr target for neutron production. They use a 30 L volume of sD_2 at 5 K as moderator and converter to produce UCN. This volume is surrounded by D_2O thermal moderator. They also use a flapper valve for UCN extraction between the proton beam pulses to limit the losses. The UCN production has been running since 2012 with an on-going EDM experiment, with a peak density of 23 UCN/cm^3.

The Mainz UCN source [84] is the only source that operates at a low power university reactor and is the newest production source. The solid deuterium converter with a volume of $V = 160$ cm^3, which is exposed to a thermal neutron fluence of 4.5×10^{13} n/cm^2, delivers up to 240000 UCN ($v \leq 6$ m/s) per pulse outside the biological shield at the experimental area. UCN densities of $\approx 10/$ cm^3 are obtained in stainless-steel bottles of $V \approx 10$ L. Their pulsed operation permits the production of high densities for storage experiments.

The UCN source at TRIUMF will use a W target to produce spallation neutrons from a 500 MeV proton beam on site. The cold neutrons will be converted to UCN in superfluid helium. this source is projected to compete with the capabilities of the best planned future UCN sources. If TRIUMF's estimated UCN density of 680 UCN cm^{-3} is achieved, it will be a new world record. Other sources and nEDM experiments aim at similar goals of hundreds to thousands of UCN cm^{-3} in the measurement volume. However, to date, superthermal sources have not produced considerably more UCN than the ILL turbine source.

1.6 Conclusion

Precision experiments involving UCN provide an attractive avenue to investigate physics beyond the standard model. For such studies high density UCN are needed. UCN are very slow neutrons with velocities < 8 m/s that can be trapped in matter, magnetic and gravitational fields. High density of UCN sources are produced in the superthermal UCN sources. A superthermal UCN sources should have a very small neutron absorption cross-section and upscattering rate while having a high UCN production rate. So far, the best candidates are superfluid helium and solid deuterium.

Both ^{4}He and solid D_2 UCN sources use quantum excitations in the converter medium to create the UCN; these are phonons in the case of superfluid sD_2 and phonons and rotons in the case of ^{4}He. Since ^{4}He does not capture neutrons and has a small upscattering probability for UCN, the superfluid ^{4}He source can be operated at lower currents for longer times, allowing a large density of neutrons to accumulate. In the case of superfluid helium, storage times of hundreds of seconds are achievable. The production rate in sD_2 is higher than in supefruid 4He, but the neutron storage lifetime is only tens of milliseconds.

The TRIUMF UCN project is the only spallation-driven superfluid-^{4}He source proposed at this time in the world [85]. The spallation-driven UCN sources at PSI [83] and LANL [82] use the phonons in solid deuterium as an alternative method of UCN production. The TRIUMF's UCN source uses an optimum proton beam structure on the minute scale to produce the highest density of UCN in the world, while sD_2 spallation sources benefit from pulsing the beam, then isolate any UCN produced as quickly as possible to achieve high UCN densities.

Name	Source Type	Technology	Status
ILL	Turbine	Reactor, CN beam	Running
ILL SUN-2	LHe	Reactor, CN beam	Running
ILL SuperSUN	LHe	Reactor, CN beam	Future
RCNP/TRIUMF/KEK	LHe	Spallation	Installing/Future
Gatchina WWR-M	LHe	Reactor	Future
LANL	sD_2	Spallation	Running/Upgrading
PSI	sD_2	Spallation	Running
Mainz	sD_2	Reactor	Running
FRM II	sD_2	Reactor	Future
NCSU PULSTAR	sD_2	Reactor	Installing

Table 1.3: Existing and future superthermal UCN sources worldwide. The existing or proposed sources at the following sites is listed: Institut Laue-Langevin (ILL) in France, Reasearch Center for Nuclear Physics (RCNP) in Japan, KEK in Japan, TRIUMF in Canada, Gatchina WWR-M in Russia, Los Alamos National Lab (LANL) and PULSTAR in the US, Mainz and FRM II in Germany.

Chapter 2

Future nEDM Measurement at TRIUMF

Finding a non-zero neutron EDM is directly linked to the extra sources of CP violation beyond the standard model. The TUCAN collaboration proposes a world-leading experiment to measure the nEDM, improving the precision by a factor of thirty compared to the present world's best experimental result. The current nEDM experiments suffer from low UCN statistics. As a result, TUCAN has intended to build the strongest UCN source in the world. To achieve this goal extensive studies of the current vertical UCN source have been conducted (See Chapters 4 and 5).

To measure the neutron EDM, an ensemble of polarized UCN are put in the presence of aligned electric and magnetic fields. The hamiltonian of the interaction of the UCN with electric and magnetic fields are described in Eqn. 1.1. The larmor precession frequency of UCN is then measured in two oriantations of parallel and anti-parallel electric and magnetic fields. For the parallel **E** and **B** fields the Larmor precession frequency of UCN is written as

$$h\nu_{\uparrow\uparrow} = 2\mu_n|\mathbf{B}^{\uparrow\uparrow}| + 2d_n|\mathbf{E}^{\uparrow\uparrow}| \tag{2.1}$$

and for anti-parallel **E** and **B** fields it is

$$h\nu_{\uparrow\downarrow} = 2\mu_n|\mathbf{B}^{\uparrow\downarrow}| + 2d_n|\mathbf{E}^{\uparrow\downarrow}|. \tag{2.2}$$

Here $\uparrow\uparrow$ indicates the parallel Electric and Magnetic fields and $\uparrow\downarrow$ represent the anti-parallel orientation of those fields. A nonzero nEDM is then extracted from any frequecy shift between these two measurements:

$$d_n = \frac{h\left(\nu_{\uparrow\uparrow} - \nu_{\uparrow\downarrow}\right) - 2\mu_n\left(|\mathbf{B}^{\uparrow\uparrow}| - |\mathbf{B}^{\uparrow\downarrow}|\right)}{2\left(|\mathbf{E}^{\uparrow\uparrow}| - |\mathbf{E}^{\uparrow\downarrow}|\right)} \tag{2.3}$$

The main reason to employ this method is because it is impossible to completely eliminate the **B** field to extract the neutron EDM. These measurements are either performed in two adjacent volumes with $|E^{\uparrow\uparrow}| = -|E^{\uparrow\downarrow}|$ and $|B^{\uparrow\uparrow}| - |B^{\uparrow\downarrow} = 0$ or measured in the same volume where the configuration of the fields change in time. In the first case it is essential to make sure that the magnetic field inside both volumes are the same and there is no field gradient and in the second method it is essential to make sure that the magnetic field is stable in time.

2.1 Ramsey Method of Separated Oscillating Fields

The Ramsey method of separated oscillating fields is the well-known measurement technique to extract the neutron EDM. Ramsey obtained an expression for the quantum mechanical transition probability of a system between two states when the system subjected to such separated oscillating fields [86]. Fig. 2.1 [87] left shows a cycle of measurement. An ensemble of polarized UCN with the inital spin $|\uparrow\rangle$ are exposed to a DC magnetic field of B_0. A first RF pulse of $B_1 \cos(\omega_{rf} t)$ prependicular to the B_0 field tips the spin of the neutrons to the transverse plane. The neutrons precess freely with their Larmor precession frequency ω_0 for some time T while accumulating a phase of $\phi = \gamma_n BT$. Then again the second oscillating magnetic field pulse of $B_1 \cos(\omega_{rf} t)$ is applied to the neutron ensemble. The essential idea is to compare the phase ϕ with $\omega_{rf} T$ and if they are identical then $B = \omega_{rf}/\gamma_n$.

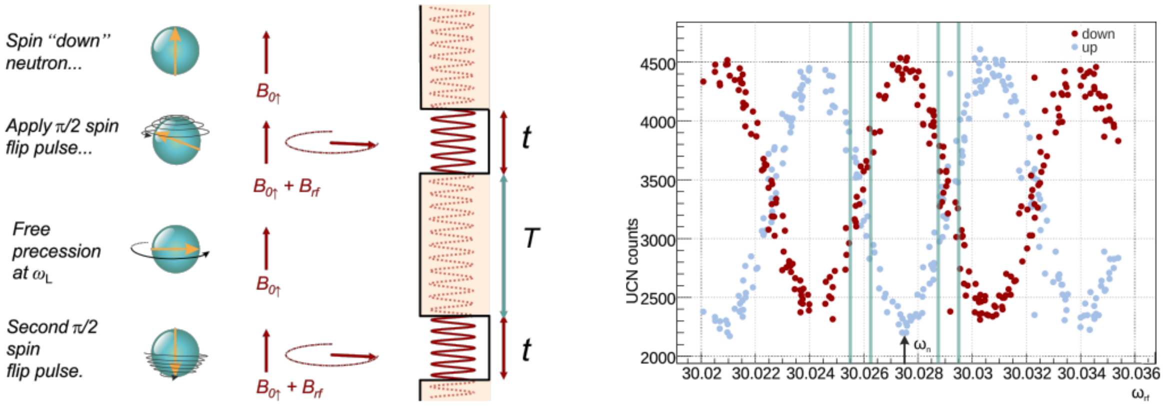

Figure 2.1: Ramsey method of separated oscillating fields. Left shows the scheme of a measurement procedure and right shows the data points. The blue points are the UCN counts with the spin up and the red points are the UCN with spin down (data from the PSI-nEDM collaboration). The width at half height $\Delta\nu$ of the central fringe is approximately $1/2T$, the four vertical lines indicate the working points.

The probability to find the UCN with spin up is

$$P(T, \omega_{rf}) = \langle\uparrow| U(T, \omega_{rf}) |\uparrow\rangle = 1 - \frac{4\omega_1^2}{\Omega^2} \sin^2 \frac{\Omega t_{\pi/2}}{2} \left[\frac{\Delta}{\Omega} \sin \frac{\Omega t_{\pi/2}}{2} \sin \frac{T\Delta}{2} - \cos \frac{\Omega t_{\pi/2}}{2} \cos \frac{T\Delta}{2} \right]^2, \tag{2.4}$$

where $U(T, \omega_{rf})$ is the time evolutions operator, $\omega_1 = -\gamma_n B_1$, $\Delta = \omega_{rf} - \omega_0$, and $\Omega = \sqrt{\Delta^2 + \omega_1^2}$. When the spin-flipping pulses are optimized we would have $\gamma_n B_1 t_{\pi/2} = \pi/2$. In this case the central fringe range ($\Delta \ll \omega_1$) and Eqn. 2.4 simplifies to

$$P(T, \omega_{rf}) = \frac{1}{2} (1 - \cos(T\Delta)). \tag{2.5}$$

In a real measurement with N UCN inside a magnetic field region this becomes

$$N^{\uparrow} = \frac{N}{2} \left\{ 1 - \alpha(T) \cos \left[(\omega_{rf} - \gamma_n B_0) \cdot \left(T + \frac{T + 4t_{\pi/2}}{\pi} \right) \right] \right\}, \tag{2.6}$$

where α is the visibility of the central fringe with spin either up or down

$$\alpha^{\uparrow/\downarrow} = \frac{N_{max}^{\uparrow/\downarrow} - N_{min}^{\uparrow/\downarrow}}{N_{max}^{\uparrow/\downarrow} + N_{min}^{\uparrow/\downarrow}}. \tag{2.7}$$

The term $4t_{\pi/2}/\pi$ is necessary to account for field inhomogeneities of B_1 and B_0 which become relevant when the pulse lenght $t_{\pi/2}$ is finite. The graph in Fig. 2.1 shows the Ramsey interference pattern by scanning ω_{rf} while everything else is kept the same. In actual nEDM measurements, only 4 points with the highest sensitivity are measured. These points are refered to as the working points. For each configuration of the electric and magnetic fields (parallel or anti-parallel) Eqn. 2.6 is fitted to the data to extract the Larmor frequency. Taking the differences of those Larmor frequencies then give access to the neutron EDM

$$d_n = \frac{\hbar(\omega_0^{\uparrow\uparrow} - \omega_0^{\uparrow\downarrow})}{2(E^{\uparrow\uparrow} - E^{\uparrow\downarrow})} = \frac{\hbar\Delta\omega}{4E}. \tag{2.8}$$

with the assumption that the magnetic field is constant (see Eqn. 2.3).

2.2 Statistical and Systematic Errors

2.2.1 Statistical Sensitivity

The statistical sensitivity of nEDM measurement per cycle is

$$\sigma(d_n) = \frac{\hbar}{2\alpha T E\sqrt{\bar{N}}} \tag{2.9}$$

where visibility α is a factor related to the neutrons polarization, $\bar{N}$ is the average total number of detected UCN, T is the free precession time and E is the electric field. The visibility depends on the longitudinal and transverse spin relaxation times T_1 and T_2 respectively. The transverse spin relaxation time T_2 arises from inhomogeneities in the magnetic field as well as the T_1 relaxation time as

$$\frac{1}{T_2} = \frac{1}{T_2'} + \frac{1}{T_1} \tag{2.10}$$

where T_2' is the transverse relaxation time only due to the field inhomogeneities.

2.2.2 Systematic Errors

The dominant systematic errors in the previous best experiment arose due to magnetic field instability (uncorrelated with the electric field E), and magnetic field inhomogeneity through the geometric phase effect (GPE). The GPE arises due to a combination of magnetic field inhomogeneity and motion of the particles in the electric field during the measurement time, when the neutrons and co-magnetometer atoms are confined in the trap. The spins of the species in the trap acquire phases relative to one another resulting in a false EDM signal [88] (see Appendix B).

2.3 TRIUMF nEDM Components

The future nEDM experiment at TRIUMF will use a room-temperature nEDM apparatus, connected to a horizontal cryogenic UCN source Fig 2.2. The cyclotron at TRIUMF produces a $\sim$ 500 MeV proton beam. Protons are guided to the spallation target using a variety of magnets. Spallation neutrons are moderated and converted to UCN in a superfluid He-II volume, which diffuse through UCN guides to the nEDM measurement cell.

In 2016 the vertical UCN source from RCNP in Japan was shipped to TRIUMF for the resarch towards the developement of the new horizontal UCN source. The UCN beamline and the current vertical UCN source are described in Chapter 4. The result of the first set of UCN experiments with the vertical source is available in Chapter 5.

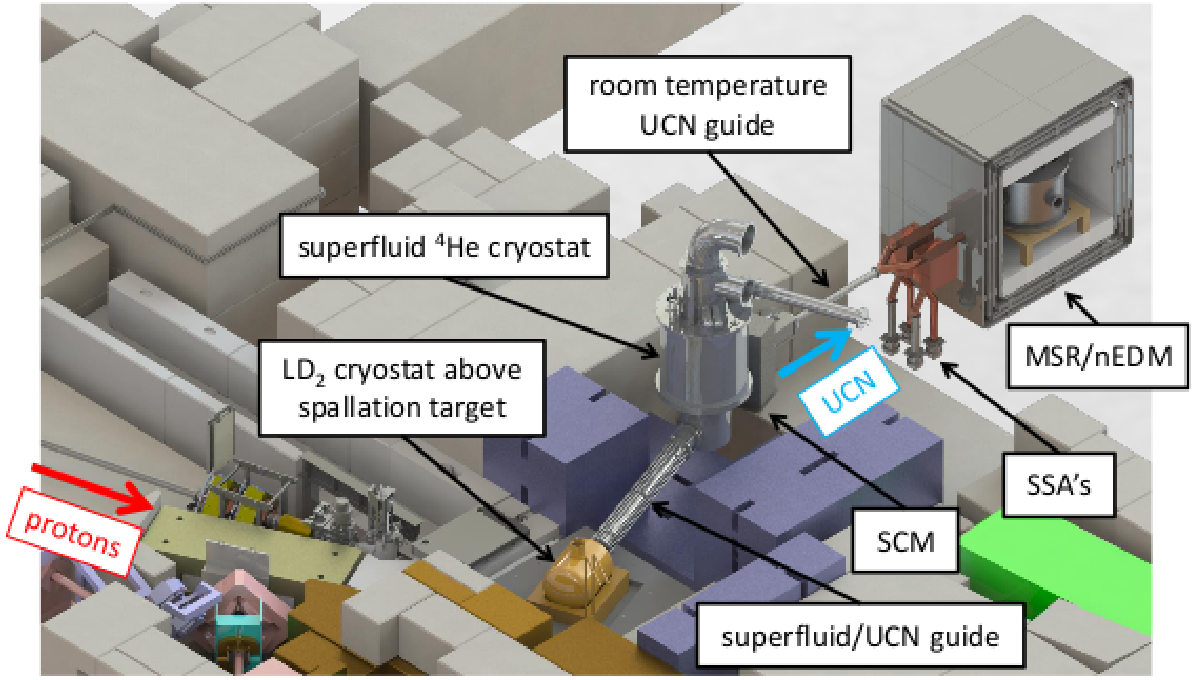

Figure 2.2: Conceptual design of the proposed UCN source and nEDM experiment. Protons strike a tungsten spallation target. Neutrons are moderated in the LD_2 cryostat and become UCN in a superfluid ^{4}He bottle, which is cooled by another cryostat located farther downstream. UCN pass through guides and the superconducting magnet (SCM) to reach the nEDM experiment located within a magnetically shielded room (MSR). Simultaneous spin analyzers (SSA's) detect the UCN at the end of each nEDM experimental cycle.

A brief description of each nEDM component is presented below.

2.3.1 Neutron Handling

2.3.2 UCN Detection

2.3.3 Magnetic Components

To chieve the desired sensitivity of 10^{-27} e·cm an extremely stable and homogeneuos B_0 magnetic field is required. The magnetic stability upper limit for TUCAN's nEDM measurement is 1 pT and the homogeneity of 1 nT/m. Because of the challenges to achieve this level of magnetic stability co-magnetometers will be used to correct for the B_0 field fluctuations. To achieve these specifications, both active and passive shielding will be utilized to nullify the uncontrolled and time-varying external fields. The desired internal magnetic field will be generated by using uniform and shim coils. Fig. 2.3 shows the schematic drawing of the magnetic components of the TUCAN nEDM experiment. Each magnetic component is explained below.

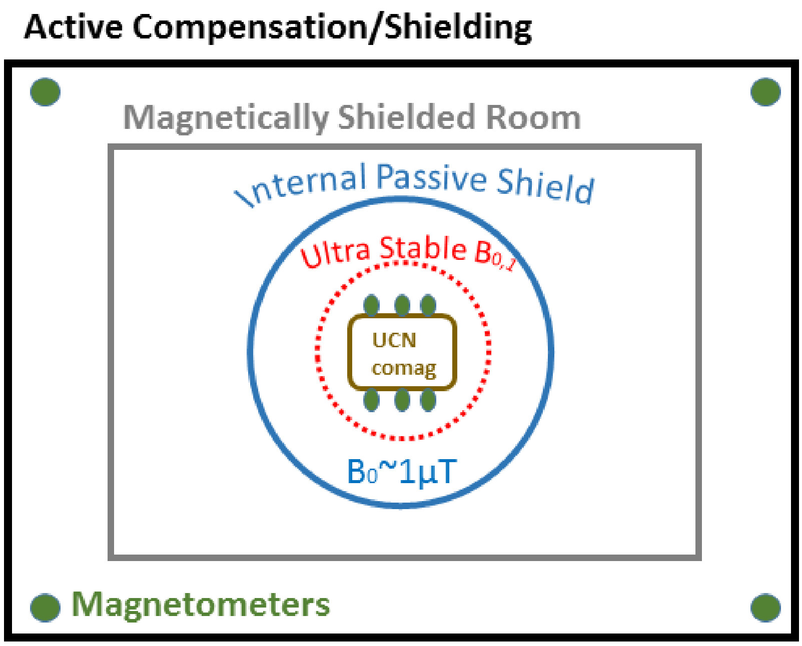

Figure 2.3: Schematic drawing for the TUCAN nEDM magnetics. From Outside in: The active compensation system followed by several layers of magnetically shielded room and passive shields nullify the environmental magnetic field. The magnetometers inside the active shielding monitor the changes in the magnetic field internal to that region. The internal coil system (B_0 and B_1 coils) generate the magnetic fields for the Ramsey cycle. The UCN and the co-magnetometers are internal to the coils.

Active Shielding

The magnetic environment at the location of the planned nEDM experiment at TRIUMF is dominated by a 400 μT static field due to the main cyclotron at TRIUMF with 1 to 100-nT fluctuations due to the other external magnetic sources such as the electrical equipment or the displacement of large magnetic objects (e.g., vehicle traffic). The TUCAN's plan is to reduce the static field to less than 1 μT using dedicated compensation coils and constant-current supplies with a readily achievable steability of 10^{-3} and to reduce the remaining static field and fluctuations by up to a factor of 100 through a separate set of compensation coils and current supplies using fluxgate magnetometers for magnetic feedback. The fluxgate sensors will be placed in the region between the compensation coils and the passive shields as shown in Fig. 2.3. A prototype active compensation system has been built at the University of Winnipeg based on Refs. [38, 89]. The system employs a set of coils centered around a cylindrical passive magnetic shield system using four 3-axis fluxgates for feedback (See Fig. **??**). Overall, the active shielding system should be able to reduce the net background magnetic field to the level of tens of nT over the volume of the nEDM cell.

Passive Shielding

The passive shielding system nullifies the residual background fields to the pT level. It will be a two-stage system: (1) a 2-layer magnetically shielded room (MSR) with (2) a smaller 3-layer shield that fits inside the room and surrounds the nEDM apparatus. The innermost layer also serves as a return yoke for the magnetic flux generated by the internal coils for the shield-coupled coil desings. A degaussing (idealization) system will be used to stabilize the shields. A combined DC shielding factor of the order of 10^6 is expected. In principle, by utilizing both active and passive shielding, the magnetic field from external sources will be reduced to the level of tens of fT over the volume of the nEDM cell. There are two prototype four-layer passive shields at the University of Winnipeg. The shields are now used to facilitate a variety of magnetic field R&D. These are made of high permeability material. In addition, there are three small witness cylinders which are made of the same material and annealed in the same oven as the large passive shields. The design principles behind the small shield, shielding factor measurements, and comparison to simulation are described in Ref. [90]. The witness cylinders are used to evaluate the temperature dependence of the shield material properties, which could be an important consideration for internal field stability (See Chapter **??**).

Internal Coils

For internal coils, self-shielded B_0 coils and shim coils are considered surrounding the nEDM cells since they provide immunity from the field perterbations induced by changes in the magnetic permeability of the passive shields arising from temperature fluctuations (See Chapter 3). High-precision current supplies ($\sim$ 1 ppm) will be used to drive all internal coils, regardless of design. AC coils will apply $\pi/2$ pulses for the UCN and comagnetometer species, to initiate free spin precession.

also add field mapping and magnetometers???

2.3.4 EDM Cells and High Voltage System

The nEDM measurement volume, consists of two storage cells to enable simultaneous measurements with both up and down orientations of the electric field (See Fig. 2.4). Each cell consists of electrodes separated by a cylindrical wall of dielectric insulator, appropriately coated for UCN compatibility. An electric field of 12 kV/cm will be created between the electrodes with minimal leakage current (< 10 pA). The storage cells will be housed inside a non-magnetic vacuum chamber providing insulating vacuum for the high voltage applied to the central electrode which separates the two cells.

There are two grounded electrodes integrated into the lids of a vacuum chamber. These electrodes are separated by an insulating side wall, containing the particles of interest, with inlets for UCN, Xe and Hg. The insulator must have a large dielectric strength and low permittivity. Therefore, it is designed to be made of deuterated polystyrene with quartz windows to allow optical access, coated by deuterated polyethylene. These materials combine high Fermi potentials, UV transparency as well as good dielectric strength. Ports will allow the introduction of the ^{199}Hg comagnetometer atoms and UCN into the cell. The optical readout of the comagnetometers requires UV-transparent windows in the insulating side wall. The use of two cells with a central electrode allows first-order compensation of magnetic field drifts and a measurement of the magnetic field gradient.

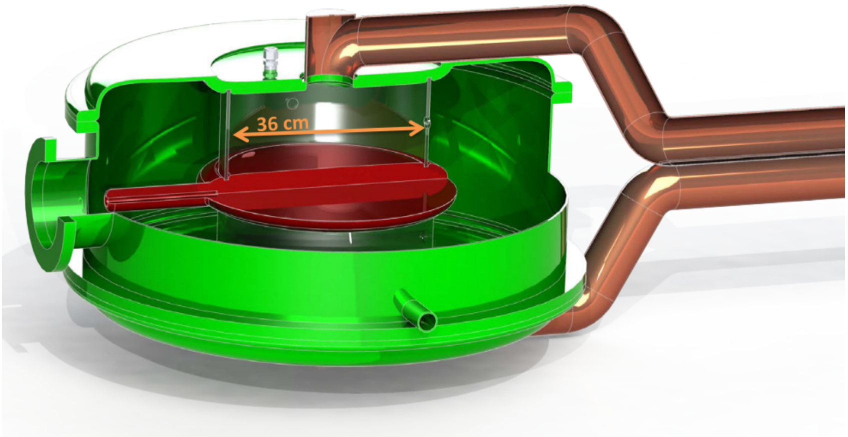

Figure 2.4: 3D drawing of the double EDM cell with vacuum chamber and UCN guides

2.3.5 Comagnetometry

To measure any changes in the precesion B_0 field, a dual-species ^{129}Xe/ ^{199}Hg Comagnetometer will be used. Here, polarized ^{129}Xe and ^{199}He are simultaneously introduced along with the UCN in the nEDM cell. Comagnetometry offers the only way to correct for false EDMs caused by leakage currents. Each atomic species is polarized using optical pumping techniques. Polarized atoms are introduced into the nEDM cell at the same time as UCN, and the spin-precession frequencies of both species are measured simultaneously. The atoms are expected to have smaller EDMs than the neutrons, and so their precession frequencies may be used to normalize magnetic field drifts. The design of the ^{199}Hg comagnetometer will be similar to that employed in the previous ILL experiment [43, 91]. The nuclear magnetization of Xe will be measured by sensing decay light after two-photon excitation [92].

2.3.6 UCN Handling and Transport

Fig. 2.5 shows the UCN transport to the EDM cell. UCN will be transported out of the source by specular reflection via guides with special coatings compatible with UCN transport and polarization. Special coatings such as NiMo, NiP and DLC are top candidates because of their high Fermi potential , small absorption and inelastic upscattering, and good specularity. A superconducting magnet (SCM) accelerates polarized UCN through barrier foils to a vacuum volume at room temperature. The UCN are then transported to the nEDM experiment by additional guides.

2.3.7 UCN Detection

The detector system will consist of a split UCN guide, two magnetized iron foils, adiabatic-fast- passage spin-flippers, and UCN counters based on ^{6}Li scintillating glass coupled to photomultiplier tubes. This is based on the detector used in the PSI UCN experiments [93]. This configuration allows simultaneous counting of both UCN spin states and hence extraction of the UCN polarization with maximum efficiency. A prototype detector, based on scintillating lithium glass, and capable of handling the highest rates of UCN expected with the TRIUMF source has been developed and tested in the highest

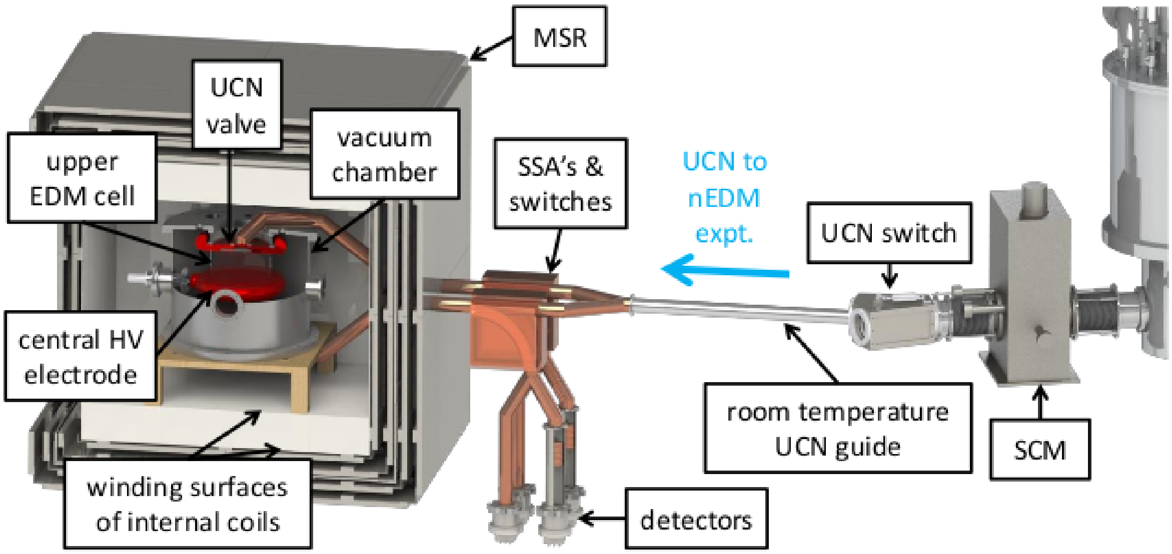

Figure 2.5: UCN delivery and the nEDM experiment. UCN exit the source by passing through the SCM spin polarizer and UCN switch and detector system, where they then enter the proposed Phase 2 nEDM experiment. UCN are loaded into the measurement cells within a MSR/coil system. At the end of the measurement cycle, UCN are counted by simultaneous spin analyzers (SSA's) including detectors. An ambient magnetic compensation system and thermally controlled room which will surround the nEDM apparatus (not shown). For scale, the innermost layer of the MSR is a 1.8 m side-length cube.

rate UCN beam available at PSI [94] (See Chapter 4).

2.3.8 UCN Source

2.3.9 DAQ?

Chapter 3

Temperature Dependence of Magnetic Permeability

3.1 Introduction

The next generation of neutron electric dipole moment (nEDM) experiments aim to measure the nEDM d_n with proposed precision $\delta d_n \lesssim 10^{-27}$ e·cm [32, 37, 40, 95–99]. In the previous best experiment [47**?**] which discovered $d_n < 3.0 \times 10^{-26}$ e·cm (90% C.L), effects related to magnetic field homogeneity and instability were found to dominate the systematic error. A detailed understanding of passive and active magnetic shielding, magnetic field generation within shielded volumes, and precision magnetometry is expected to be crucial to achieve the systematic error goals for the next generation of experiments. Much of the research and development efforts for these experiments are focused on careful design and testing of various magnetic shield geometries with precision magnetometers [34, 89, 100**?** , 101].

In nEDM experiments, the spin-precession frequency ν of neutrons placed in static magnetic B_0 and electric E fields is measured. The measured frequencies for parallel ν_+ and antiparallel ν_- relative orientations of the fields is sensitive to the neutron electric dipole moment d_n

$$h\nu_\pm = 2\mu_n B_0 \pm 2d_n E \tag{3.1}$$

where μ_n is the magnetic moment of the neutron.

A problem in these experiments is that if the magnetic field B_0 drifts over the course of the measurement period, it degrades the statistical precision with which d_n can be determined. If the magnetic field over one measurement cycle is determined to $\delta B_0 = 10$ fT, it implies an additional statistical error of $\delta d_n \sim 10^{-26}$ e·cm (assuming an electric field of $E = 10$ kV/cm which is reasonable for a neutron EDM experiment). Over 100 days of averaging, this would make a $\delta d_n \sim 10^{-27}$ e·cm measurement possible. Unfortunately the magnetic field in the experiment is never stable to this level. For this reason, experiments use a comagnetometer and/or surrounding atomic magnetometers to measure and correct the magnetic field to this level [89, 100**?**]. Drifts of 1-10 pT in B_0 may be corrected using the comagnetometer technique, setting a goal magnetic stability for the B_0 field generation system in a typical nEDM experiment.

In such experiments, typically $B_0 = 1$ μT is used to provide the quantization axis for the ultracold neutrons. The B_0 magnetic field generation system typically includes a coil placed within a passively magnetically shielded volume. The passive magnetic shield is generally composed of a multi-layer shield formed from thin shells of material with high magnetic permeability (mu-metal). The outer layers of the shield are normally cylindrical [32, 95] or form the walls of a magnetically shielded room [34, 36]. The innermost magnetic shield is normally a specially shaped shield, where the design of the coil in relation to shield is carefully taken into account to achieve adequate homogeneity [37, 97**?**].

Mechanical and temperature changes of the passive magnetic shielding [102**?**], and the degaussing procedure [36, 103**?**] (also known as demagnetization, equilibration, or idealization), affect the stability of the magnetic field within magnetically shielded rooms. Active stabilization of the background magnetic field surrounding magnetically shielded rooms can also improve the internal stability [89, 102, 104]. The current supplied to the B_0 coil is generated by an ultra-stable current source [100]. The coil must also be stabilized mechanically relative to the magnetic shielding.

One additional effect, which is the subject of this paper, relates to the fact that the B_0 coil in most nEDM experiments is magnetically coupled to the innermost magnetic shield. If the magnetic properties of the innermost magnetic shield change as a function of time, it then results in a source of instability of B_0. In the present work, we estimate this effect and characterize one possible source of instability: changes of the magnetic permeability μ of the material with temperature.

While the sensitivity of magnetic alloys to temperature variations has been characterized in the past [105, 106], we sought to make these measurements in regimes closer to the operating parameters relevant to nEDM experiments. For these alloys, it is also known that the magnetic properties are set during the final annealing process [106–108]. In this spirit we performed our measurements on "witness" cylinders, which are small open-ended cylinders made of the same material and annealed at the same time as other larger shields are being annealed.

The paper proceeds in the following fashion:

- The dependence of the internal field on magnetic permeability of the innermost shielding layer for a typical nEDM experiment geometry is estimated using a combination of analytical and finite element analysis techniques. This sets a scale for the stability problem.

- New measurements of the temperature dependence of the magnetic permeability are presented. The measurements were done in two ways in order to study a variety of systematic effects that were encountered.

- Finally, the results of the calculations and measurements are combined to provide a range of temperature sensitivities that takes into account sample-to-sample and measurement-to-measurement variations.

3.2 Sensitivity of Internally Generated Field to Permeability of the Shield $B_0(\mu)$

The presence of a coil inside the innermost passive shield turns the shield into a return yoke, and generally results in an increase in the magnitude of B_0. The ratio of this field inside the coil in the presence of the magnetic shield to that of the coil in free space is referred to as the reaction factor C, and can be calculated analytically for spherical and infinite cylindrical geometries [12**?**]. The key issue of interest for this work is the dependence of the reaction factor on the permeability μ of the innermost shield. Although this dependence can be rather weak, the constraints on B_0 stability are very stringent. As a result, even a small change in the magnetic properties of the innermost shield can result in an unacceptably large change in B_0.

To illustrate, we consider here the model of a sine-theta surface current on a sphere of radius a, inside a spherical shell of inner radius R, thickness t, and linear permeability μ. The uniform internal field generated by this ideal spherical coil is augmented by the reaction factor in the presence of the shield, but is otherwise left undistorted. The general reaction factor for this model is given by Eq. (38) in Ref. [12]. In the high-μ limit, with $t \ll R$, the reaction factor can be approximated as

$$C \simeq 1 + \frac{1}{2}\left(\frac{a}{R}\right)^3 \left(1 - \frac{3}{2}\frac{R}{t}\frac{\mu_0}{\mu}\right), \tag{3.2}$$

which highlights the dependence of B_0 on the relative permeability $\mu_r = \mu/\mu_0$ of the shield.

Fig. 3.1 (upper) shows a plot of B_0 versus μ_r for coil and shield dimensions similar to the ILL nEDM experiment [39**?**]: $a = 0.53$ m, $R = 0.57$ m, and $t = 1.5$ mm. In addition to analytic calculations, we also include the results of two axially symmetric simulations conducted using FEMM [109] to assess the effects of geometry and discretization of the surface current. The differences are small, suggesting that the ideal spherical model of Ref. [12] and the high-μ approximation of Eq. 3.2 provide valuable insight for the design and analysis of shield-coupled coils.

In the first simulation, the same spherical geometry was used as for the analytic calculations. However, the surface current was discretized to 50 individual current loops, inscribed onto a sphere, and equally spaced vertically (i.e. a discrete sine-theta coil). A square wire profile of side length 1 mm was used. As shown in Fig. 3.1, this simulation gave excellent agreement with the analytic calculations. In the second simulation, a solenoid coil and cylindrical shield (length/radius = 2) were used with the same dimensions as above. Similarly, the coil was modelled as 50 evenly spaced current loops, with the distance from an end loop to the inner face of the shield endcap being half the inter-loop spacing. In the limit of tight-packing (i.e., a continuous surface current) and infinite μ, the image currents in the end caps of the shield act as an infinite series of current loops, giving the ideal uniform field of an infinitely long solenoid [110, 111]. As shown in Fig. 3.1, the result is similar to the spherical case, with differences of order one part per thousand and a somewhat steeper slope of $B_0(\mu_r)$.

Fig. 3.1 (lower) shows the normalized slope $\frac{\mu}{B_0}\frac{dB_0}{d\mu}$ of the curves from Fig. 3.1 (upper). In ancillary measurements of shielding factors (discussed briefly in Section 3.3.1), we found $\mu_r = 20,000$ to offer a reasonable description of the quasistatic shielding factor of our shield. Using this value as the magnetic permeability of our shield material, Fig. 3.1 (lower) shows that $\frac{\mu}{B_0}\frac{dB_0}{d\mu}$ varies by about 20% (from 0.008 to 0.01) for the spherical vs. solenoidal geometries. We adopt the value $\frac{\mu}{B_0}\frac{dB_0}{d\mu} = 0.01$ as an estimate of this slope in our discussions in Section 3.4, acknowledging that the value depends on the coil and shield design.

For a high-μ innermost shield, the magnetic field lines emanating from the coil all return through the shield. This principle can be used to estimate the magnetic field B_m inside the shield material, and in our studies gave good agreement with FEA-based simulations. For the solenoidal geometry previously described and used for the calculations

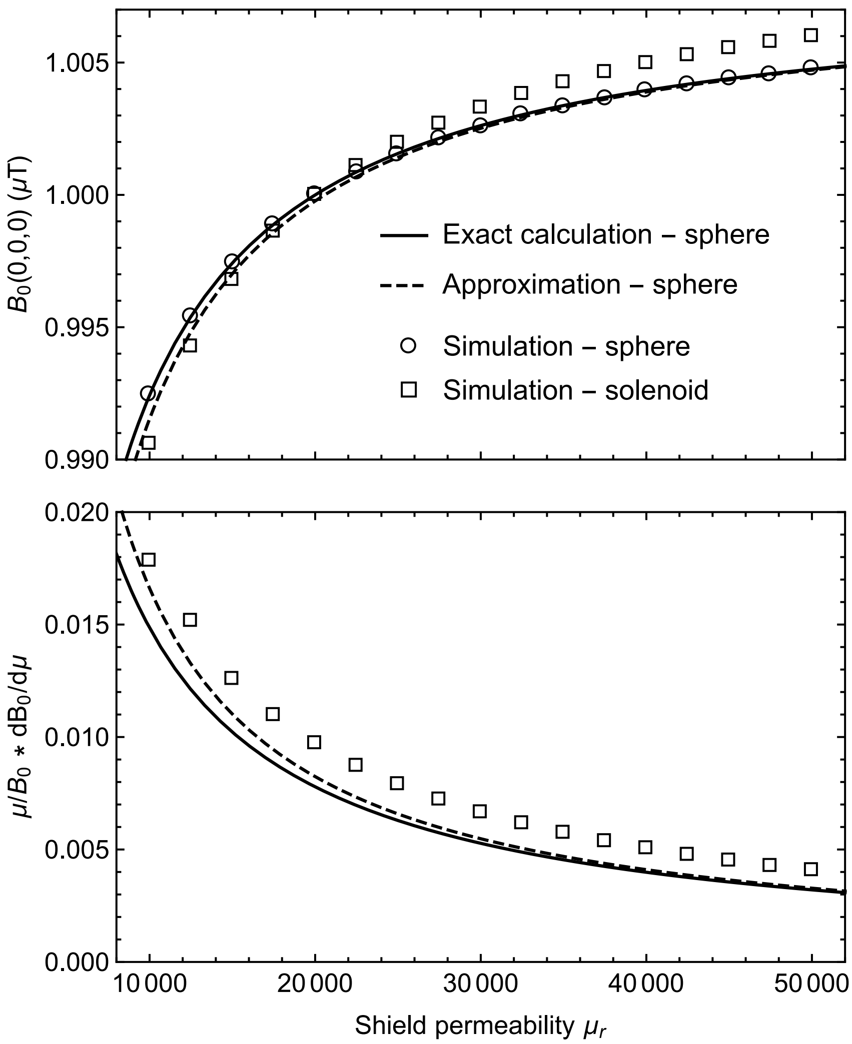

Figure 3.1: Upper: Magnetic field at the coil center as a function of magnetic permeability of the surrounding magnetic shield for a geometry similar to the ILL nEDM experiment as discussed in the text. Lower: $\frac{\mu}{B_0}\frac{dB_0}{d\mu}$ vs. permeability. The solid curve is the exact calculation for the ideal spherical coil and shield from Ref. [12]; the dashed curve is the approximation of Eq. 3.2. The circles and squares are the FEMM-based simulations for the spherical and solenoidal geometries with discrete currents. Since the spherical simulation was in agreement with the calculation, it is omitted from the lower graph. For the exact calculation and the two simulations, currents were chosen to give $B_0 = 1$ μT at $\mu_r = 20,000$.

in Fig. 3.1, B_m is largest in the side walls of the solenoidal flux return, attaining a maximum value of 170 μT. If we assume μ_r=20,000, the H_m field is 0.007 A/m. Typically the shield is degaussed (idealized) with the internal coil energized. After degaussing, B_m must be approximately the same, since essentially all flux returns through the shield. However, the H_m field may become significantly smaller because after degaussing, it must fall on the ideal magnetization curve in $B_m - H_m$ space. (For a discussion of the ideal magnetization curve, we refer the reader to Ref. [**?**].) In principle, the H_m field could be reduced by an order of magnitude or more, depending on the steepness of the ideal magnetization curve near the origin. Thus $B_m = 170$ μT and $H_m < 0.007$ A/m set a scale for the relevant values for nEDM experiments. Furthermore, the field in the nEDM measurement volume, as well as in the magnetic shield, must be stable for periods of typically hundreds of seconds (corresponding to frequencies < 0.01 Hz). This sets the relevant timescale for magnetic properties most relevant to nEDM experiments.

3.3 Measurements of $\mu(T)$

3.3.1 Previous Measurements and their Relationship to nEDM Experiments

Previous measurements of the temperature dependence of the magnetic properties of high-permeability alloys have been summarized in Refs. [105, 108, 112]. These measurements are normally conducted using a sample of the material to create a toroidal core, where a thin layer of the material is used in order to avoid eddy-current and skin-depth effects [106, 112]. A value of μ is determined by dividing the amplitude of the sensed B_m-field by the amplitude of the driving AC H_m-field (similar to the method described in Section 3.3.3). Normally the frequency of the H_m-field is 50 or 60 Hz. The value of μ is then quoted either at or near its maximum attainable value by adjusting the amplitude of H_m. Depending on the details of the $B_m - H_m$ curve for the material in question, this normally means that μ is quoted for the amplitude of H_m being at or near the coercivity of the material [105, 106], resulting in large values up to $\mu_r = 4 \times 10^5$.

It is well known that μ measured in this fashion for toroidal, thin metal wound cores depends on the annealing process used for the core. There is a particularly strong dependence on the take-out or tempering temperature after the high-temperature portion of the annealing process has been completed [105, 106, 112]. Such studies normally suggest a take-out temperature of 490-500°C. This ensures that the large $\mu_r = 4 \times 10^5$ is furthermore maximal at room temperature. Slight variations around room temperature, and assuming the take-out temperature is not controlled to better than a degree, imply a scale of possible temperature variation of μ of approximately $\left|\frac{1}{\mu}\frac{d\mu}{dT}\right| \simeq$ 0.3-1%/K at room temperature [105, 106].

A challenge in applying these results to temperature stability of nEDM experiments is that, when used as DC magnetic shielding, the high-permeability alloys are usually operated for significantly different parameters (B_m, H_m, and frequencies).

For example, when used in a shielding configuration, the effective permeability is often measured to be typically $\mu_r = 20,000$ rather than 4×10^5. This arises in part because H_m is well below the DC coercivity. As noted in Section 3.2, a more appropriate H_m for the innermost magnetic shield of an nEDM experiment is < 0.007 A/m, whereas the coercivity is $H_c = 0.4$ A/m [106]. The frequency dependence of the measurements could also be an issue. Typically, nEDM experiments are concerned with slow drifts at < 0.01 Hz timescales whereas the previously reported $\mu(T)$ measurements are performed in an AC mode at 50-60 Hz.

The goal of our experiments was to develop techniques to characterize the material properties of our own magnetic shields post-annealing, in regimes more relevant to nEDM experiments.

We created a prototype passive magnetic shield system in support of this and other precision magnetic field research for the future nEDM experiment to be conducted at TRIUMF. The shield system is a four-layer mu-metal shield formed from nested right-circular cylindrical shells with endcaps. The inner radius of the innermost shield is 18.44 cm, equal to its half-length. The radii and half-lengths of the progressively larger outer shields increase geometrically by a factor of 1.27. Each cylinder has two endcaps which possess a 7.5 cm diameter central hole. A stove-pipe of length 5.5 cm is placed on each hole was designed to minimize leakage of external fields into the progressively shielded inner volumes. The design is similar to another smaller prototype shield discussed in Ref. [90]. The magnetic shielding factors of each of the four cylindrical shells, and of various combinations of them, were measured and found to be consistent with $\mu_r \sim 20,000$.

In our studies of the material properties of these magnetic shields, two different approaches to measure $\mu(T)$ were pursued. Both approaches involved experiments done using witness cylinders made of the same material and annealed at the same time as the prototype magnetic shields. We therefore expect they have the same magnetic properties as the larger prototype shields, and they have the advantage of being smaller and easier to perform measurements with.

The two techniques employed to determine $\mu(T)$ were the following:

1. measuring the low-frequency AC axial magnetic shielding factor of the witness cylinder as a function of temperature, and

2. measuring the temperature-dependence of the slope of a minor B-H loop, using the witness cylinder as a transformer core, similar to previous measurements of the temperature dependence of μ, but for parameters closer to those encountered in nEDM experiments.

We now discuss the details and results of each technique.

3.3.2 Axial Shielding Factor Measurements

In these measurements, a witness cylinder was used as a magnetic shield. The shield was subjected to a low-frequency AC magnetic field of ~ 1 Hz. The amplitude of the shielded magnetic field B_s was measured at the center of the witness cylinder using a fluxgate magnetometer. Changes in B_s with temperature signify a dependence of the permeability μ on temperature. The relative slope of $\mu(T)$ can then be calculated using

$$\frac{1}{\mu}\frac{d\mu}{dT} = -\frac{\frac{1}{B_s}\frac{dB_s}{dT}}{\frac{\mu}{B_s}\frac{dB_s}{d\mu}}. \tag{3.3}$$

The numerator was taken from the measurements described above. The denominator was taken from finite-element simulations of the shielding factor for this geometry as a function of μ.

This measurement technique was sufficiently robust to extract the temperature dependence of the shielding factor with some degree of certainty. Possible drifts and temperature depends of the fluxgate magnetometer offset were mitigated by using an AC magnetic field. Any temperature coefficients in the rest of the instrumentation were controlled by performing the same measurements with a copper cylindrical shell in place of the mu-metal witness cylinder.

This technique is quite different than the usual transformer core measurements conducted by other groups. As shall be described, it offers an advantage that considerably smaller B_m and H_m fields can be accessed. Measuring the temperature dependence of the shielding factor is also considerably easier than measuring the temperature dependence of the reaction factor, since the sensitivity to changes in $\mu(T)$ is considerably larger in magnitude for the shielding factor case where $\frac{\mu}{B_s}\frac{dB_s}{d\mu} \sim -1$ compared to the reaction factor case where $\frac{\mu}{B_0}\frac{dB_0}{d\mu} \sim 0.01$.

Experimental Apparatus for Axial Shielding Factor Measurements

The witness cylinder was placed within a homogeneous AC magnetic field. The field was created within the magnetically shielded volume of the prototype magnetic shielding system (described previously in Section 3.3.1) in order to provide a controlled magnetic environment. A short solenoid inside the shielding system was used to produce the magnetic field. The solenoid has 14 turns with 2.6 cm spacing between the wires. The solenoid was designed so that the field produced by the solenoid plus innermost shield approximates that of an infinite solenoid. The magnetic field generated by the solenoid was typically 1 μT in amplitude. The solenoid current was varied sinusoidally at typically 1 Hz.

The witness cylinder was placed into this magnetic field generation system as shown schematically in Fig. 3.2. The cylinder was held in place by a wooden stand.

A Bartington fluxgate magnetometer Mag-03IEL70 [113] (low noise) measured the axial magnetic field at the center of the witness cylinder. The fluxgate was a "flying lead" model, meaning that each axis was available on the end of a short electrical lead, separable from the other axes. One flying lead was placed in the center of the witness cylinder, the axis of the fluxgate being aligned with that of the witness cylinder. The fluxgate was held in place rigidly by a plastic mounting fixture, which was itself rigidly mounted to the witness cylinder.

To increase the resolution of the measured signal from the fluxgate, a Bartington Signal Conditioning Unit (SCU) was used with a low-pass filter set to typically 10-100 Hz and a gain set to typically > 50. The signal from the SCU was demodulated by an SR830 lock-in amplifier [114] providing the in-phase and out-of-phase components of the signal. The sinusoidal output of the lock-in amplifier reference output itself was normally used to drive the solenoid generating the magnetic field. The time constant on the lock-in was typically set to 3 seconds with 12 dB/oct rolloff.

As shall be described in Section 3.3.2, a concern in the measurement was changes in the field measured by the fluxgate that could arise due to motion of the system components, or other temperature dependences. This could generate a false slope with temperature that might incorrectly be interpreted as a change in the magnetic properties of the witness cylinder.

To address possible motion of the witness cylinder with respect to the field generation system, another coil (the loop coil, also shown in Fig. 3.2) was wound on a plastic holder mounted rigidly to the witness cylinder. The coil was one loop of copper wire with a diameter of 9.7 cm. Plastic set screws in the holder fixed the loop coil to be coaxial with the witness cylinder.

Systematic differences in the results from the two coils (the solenoidal coil, and the loop coil) were used to search for motion artifacts. As well, some differences could arise due to the different magnetic field produced by each coil, and so such measurements could reveal a dependence on the profile of the applied magnetic field. This is described further in Section 3.3.2.

The temperature of the witness cylinder was measured by attaching four thermocou-

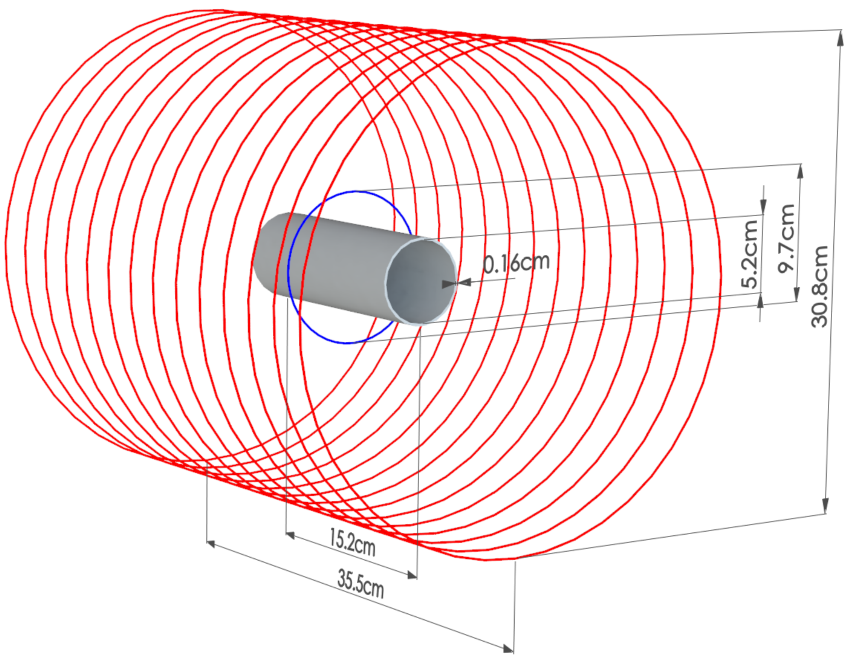

Figure 3.2: (color online) Axial shielding factor measurement setup. The witness cylinder with an inner diameter of 5.2 cm and a length of 15.2 cm is placed inside a solenoid (shown in red) with a diameter of 30.8 cm and a length of 35.5 cm, containing 14 turns. The thickness of the witness cylinder is $1/16'' = 0.16$ cm. The loop coil (shown in blue) is mechanically coupled to the witness cylinder and has a diameter of 9.7 cm.

ples at different points along the outside of the cylinder. This allowed us to observe the temperature gradient along the witness cylinder. To reduce any potential magnetic contamination, T-type thermocouples were used, which have copper and constantan conductors. (K-type thermocouples are magnetic.)

Thermocouple readings were recorded by a National Instruments NI-9211 temperature input module. The magnetic field (signified by the lock-in amplifier readout) and the temperature were recorded at a rate of 0.2 Hz.

Temperature variations in the experiment were driven by ambient temperature changes in the room, although forced air and other techniques were also tested. These are described further in Section 3.3.2.

Data and Interpretation

An example of the typical data acquired is shown in Fig. 3.3. For these data, the field applied by the solenoid coil was 1 μT in amplitude, at a frequency of 1 Hz. Fig. 3.3(a) shows the temperature of the witness cylinder over a 70-hr measurement. The temperature changes of 1.4 K are caused by diurnal variations in the laboratory. The shielded magnetic field amplitude B_s within the witness cylinder is anti-correlated with the temperature trend as shown in Fig. 3.3(b). Here, B_s is the sum in quadrature of the amplitudes of the in-phase and out-of-phase components (most of the signal is in phase). The magnetic field is interpreted to depend on temperature, and the two quantities are graphed as a function of one another in Fig. 3.3(c). The slope in Fig. 3.3(c) has been calculated using a linear fit to the data. The relative slope at 23°C was found to be

$\frac{1}{B_s}\frac{dB_s}{dT} = -0.75\%/\mathrm{K}$.

Figs. 3.3(d), (e), and (f) show the same measurement with essentially the same settings, when the mu-metal witness cylinder is replaced by a copper cylinder. A similar relative vertical scale has been used in Figs. 3.3(e) and (f) as Figs. 3.3(b) and (c). This helps to emphasize the considerably smaller relative slope derived from panel (f) compared to panel (c). A variety of measurements of this sort were carried out multiple times for different parameters such as coil current. Running the coil at the same current tests for effects due to heating of the coil, whereas running the coil at a current which equalizes the fluxgate signal to its value when the mu-metal witness cylinder is present tests for possible effects related to the fluxgate. For all measurements the temperature dependence of the demodulated magnetic signal was $< 0.1\%/\mathrm{K}$, giving confidence that unknown systematic effects contribute below this level.

Some deviations from the linear variation of B_s with T can be seen in the data, particularly in Figs. 3.3(a), (b), and (c). For example, when the temperature changes rapidly, the magnetic field takes some time to respond, resulting in a slope in $B_s - T$ space that is temporarily different than when the temperature is slowly varying. This is typical of the data that we acquired, that the data would generally follow a straight line if the temperature followed a slow and smooth dependence with time, but the data would not be linear if the temperature varied rapidly or non-monotonically with time. We also tried other methods of temperature control, such as forced air, liquid flowing through tubing, and thermo-electric coolers. The diurnal cycle driven by the building's air conditioning system gave the most stable method of control and the most reproducible results for temperature slopes.

As mentioned earlier, data were acquired for both the solenoid coil and the loop coil. A summary of the data is provided in Table 3.1. Repeated measurements of temperature slopes using the loop coil fell in the range $0.4\%/\mathrm{K} < |\frac{1}{B_s}\frac{dB_s}{dT}| < 1.5\%/\mathrm{K}$. Similar measurements for the solenoidal coil yielded $0.3\%/\mathrm{K} < |\frac{1}{B_s}\frac{dB_s}{dT}| < 0.8\%/\mathrm{K}$.

In general, the slopes measured with the loop coil were larger than for the solenoidal coil. This is particularly evident for measurements 6-12, which were acquired daily over the course of a few weeks alternating between excitation coils but all used the same witness cylinder and otherwise without disturbing the measurement apparatus. A partial explanation of this difference is offered by the field profile generated by each coil, and its interaction with the witness cylinder. This is addressed further in Section 3.3.2.

The other difference between the loop coil and the solenoidal coil was that the loop coil was rigidly mounted to the witness cylinder, reducing the possibility of artifacts from relative motion. Given that this did not reduce the range of the measured temperature slopes we conclude that relative motion was well controlled in both cases.

Several other possible systematic effects were considered, all of which were found to give uncertainties on the measured slopes $< 0.1\%/\mathrm{K}$. These included: thermal expansion of components including the witness cylinder itself, temperature variations of the magnetic shielding system within which the experiments were conducted, degaussing of the witness cylinder, and temperature slopes of various components e.g. the fluxgate magnetometer and the lock-in amplifier.

As mentioned earlier in reference to Fig. 3.3(d), (e), and (f), the stability of the system was also tested by replacing the mu-metal witness cylinder with a copper cylinder and in all cases temperature slopes $< 0.1\%/\mathrm{K}$ were measured, giving confidence that other unknown systematic effects contribute below this level.

Based on the systematic effects that we studied, we conclude that they do not explain

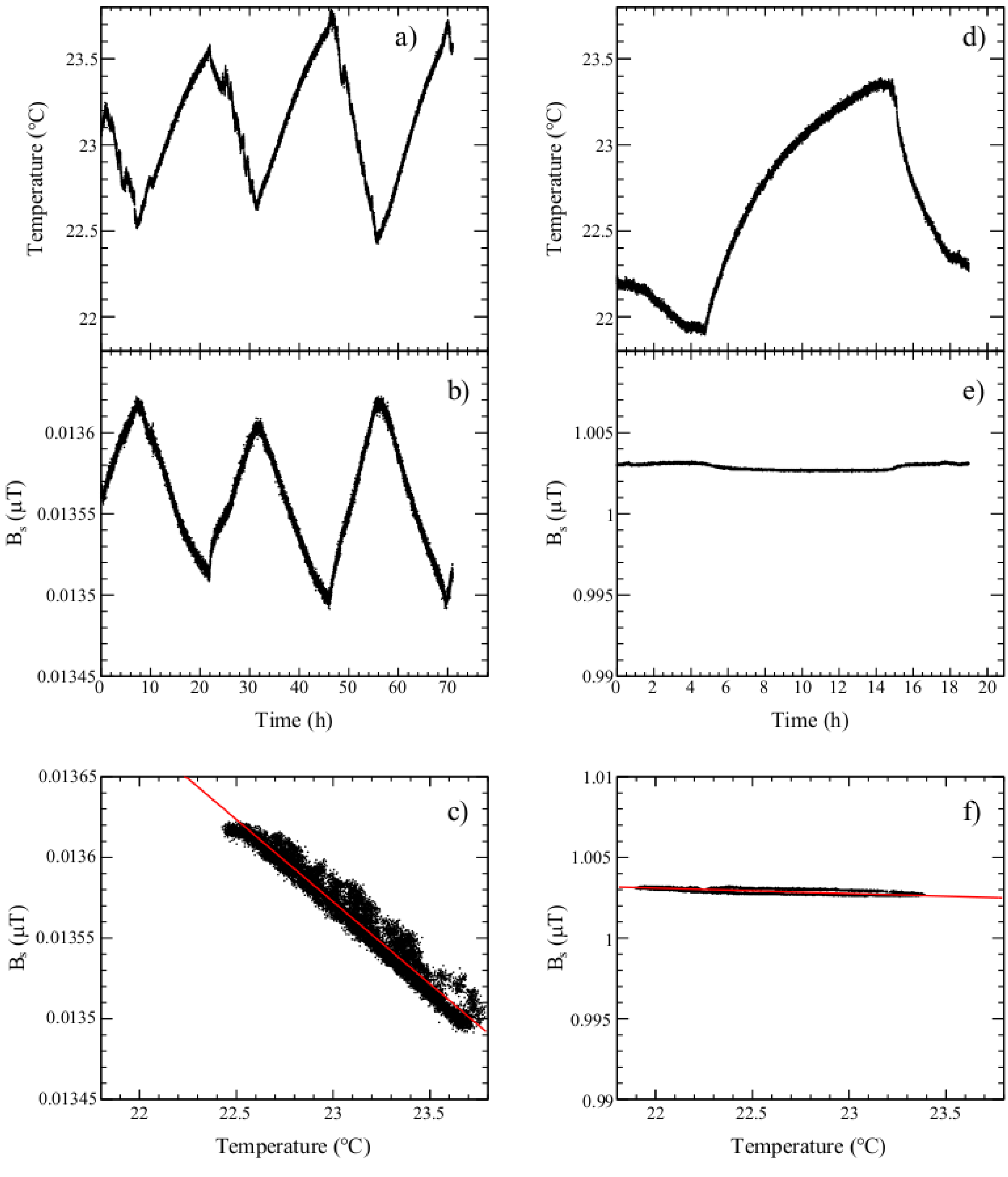

Figure 3.3: Ambient temperature and shielded magnetic field amplitude, measured over a 70 hour period. (a) temperature of the witness cylinder as a function of time. (b) magnetic field amplitude measured by fluxgate at center of witness cylinder vs. time. (c) magnetic field vs. temperature with linear fit to data giving $\frac{1}{B_s}\frac{dB_s}{dT} = -0.75\%/\mathrm{K}$ (evaluated at 23°C). In panels (d), (e), and (f), the same quantities are shown for a 20-hour run with a copper cylinder in place of the witness cylinder with the linear fit giving $\frac{1}{B_s}\frac{dB_s}{dT} = -0.03\%/\mathrm{K}$.

Trial #	$\frac{1}{B_s}\frac{dB_s}{dT}$ (%/K)	Coil type
1	-0.32	solenoid
2	-0.30	solenoid
3	-0.33	solenoid
4	-1.53	loop
5	-0.42	loop
6	-1.30	loop
7	-0.74	solenoid
8	-1.05	loop
9	-0.73	solenoid
10	-1.23	loop
11	-0.75	solenoid
12	-1.12	loop

Table 3.1: Summary of data acquired for the AC axial shielding factor measurements, in chronological order. Data with an applied field of $\sim 1-6\mu T$ and a measurement frequency of 1 Hz are included. Data which used daily fluctuations of the temperature from 21-24°C over a 10-80 hour period are included. Other data acquired for systematic studies are not included in the table.

the ranges of values measured for $\frac{1}{B_s}\frac{dB_s}{dT}$. We suspect that the range measured is either some yet uncharacterized systematic effect, or a complicated property of the material. We use this range to set a limit on the slope of $\mu(T)$

Geometry correction and determination of $\mu(T)$

To relate the data on $B_s(T)$ to $\mu(T)$, the shielding factor of the witness cylinder as a function of μ must be known. Finite element simulations in FEMM and OPERA were performed to determine this factor. The simulations are also useful for determining the effective values of B_m and H_m in the material, which will be useful to compare to the case for typical nEDM experiments when the innermost shield is used as a flux return.

For closed objects, such as spherical shells [**?** **?**], the shielding factor approaches infinity as $\mu \to \infty$, and $|\frac{\mu}{B_s}\frac{dB_s}{d\mu}| \to 1$. Because the witness cylinders are open ended, the shielding factor asymptotically approaches a constant rather than infinity in the high-μ limit, and as a result $|\frac{\mu}{B_s}\frac{dB_s}{d\mu}| < 1$ here. From the simulations the ratio $\frac{\mu}{B_s}\frac{dB_s}{d\mu}$ was calculated. A linear model of the material was used where $\mathbf{B_m} = \mu\mathbf{H_m}$ with μ constant.

The simulations differed slightly in their results, dependent on whether OPERA or FEMM was used, and whether the solenoidal coil or loop coil were used. Based on the simulations, the result is $|\frac{\mu}{B_s}\frac{dB_s}{d\mu}| = 0.42-0.50$ for the solenoidal coil, with the lower value being given by FEMM and the upper value being given by a 3D OPERA simulation, for identical geometries. This is somewhat lower than the value suggested by Ref. [115] with fits to simulations performed in OPERA, which we estimate to be 0.6. We adopt our value since it is difficult to determine precisely from Ref. [115]. For the loop coil, we determine $|\frac{\mu}{B_s}\frac{dB_s}{d\mu}| = 0.56-0.65$, the range being given again by a difference between FEMM and OPERA.

Combining the measurement and the simulations, the temperature dependence of the effective μ (at $\mu_r = 20,000$ which is consistent with our measurements) can be calculated

	$\lvert\frac{\mu}{B_s}\frac{dB_s}{d\mu}\rvert$ (simulated)	$\lvert\frac{1}{B_s}\frac{dB_s}{dT}\rvert$ (%/K) (measured)	$\frac{1}{\mu}\frac{d\mu}{dT}$ (%/K) (extracted)
Solenoidal Coil	0.42-0.50	0.3-0.8	0.6-1.9
Loop Coil	0.56-0.65	0.4-1.5	0.6-2.7

Table 3.2: Summary of OPERA and FEMM simulations and shielding factor measurements, resulting in extracted temperature slopes of μ.

by equation (3.3). The results of the simulations and measurements are presented in Table 3.2. Combining the loop coil and solenoidal coil results, we find $0.6\%/\mathrm{K} < \frac{1}{\mu}\frac{d\mu}{dT} < 2.7\%/\mathrm{K}$ to represent the full range for the possible temperature slope of μ that observed in these measurements.

As stated earlier, the simulations also provided a way to determine the typical B_m and H_m internal to the material of the witness cylinder. According to the simulations, the B_m amplitude was typically 100 μT and the H_m amplitude was typically 0.004 A/m. These are comparable to the values normally encountered in nEDM experiments, recalling from Section 3.2 that $H_m < 0.007$ A/m for the innermost magnetic shield of an nEDM experiment. A caveat is that these measurements were typically conducted using AC fields at 1 Hz, as opposed to the DC fields normally used in nEDM experiments.

3.3.3 Transformer Core Measurements

An alternative technique similar to the standard method of magnetic materials characterization via magnetic induction was also used to measure changes in μ. In this measurement technique, the witness cylinder was used as the core of a transformer. Two coils (primary and secondary) were wound on the witness cylinder using multistranded 20-gauge copper wire. The windings were made as tight as possible, but not so tight as to potentially stress the material. The windings were not potted in place. Three witness cylinders were tested. Data were acquired using different numbers of turns on both the primary and secondary coils (from 6 to 48 on the primary, and from 7 to 24 on the secondary).

Fig. 3.4 shows a picture of one of the witness cylinders, wound as described. It also shows a schematic diagram of the measurement setup, which we now use to describe the measurement principle.

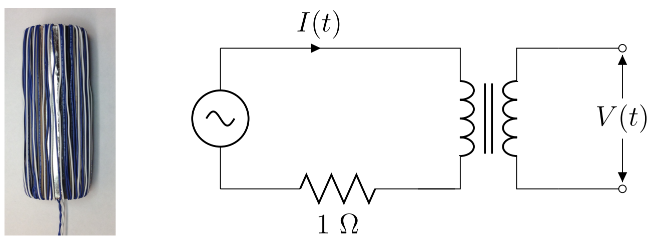

Figure 3.4: Photograph of a witness cylinder showing transformer windings (left) and schematic of the transformer measurement (right). The primary coil was driven by the sine-out of an SR830 lock-in amplifier, which was also used to demodulate induced voltage $V(t)$ in the secondary coil. The driving current $I(t)$ was sensed by measuring the voltage across a stable 1 Ω resistor.

The primary coil generated an AC magnetic field as a function of time $H(t)$, while the secondary coil was used to measure the emf induced by the time-varying magnetic flux proportional to $dB(t)/dt$. To a good approximation

$$H_m(t) = \frac{N_p I(t)}{2\pi R} \tag{3.4}$$

where N_p is the number of turns in the primary, $I(t)$ is the current in the primary, and R is the radius of the witness cylinder, and

$$\frac{dB_m(t)}{dt} = \dot{B}_m(t) = \frac{V(t)}{b\ell} \tag{3.5}$$

where $V(t)$ is the voltage generated in the secondary, and b and ℓ are the thickness and length of the witness cylinder respectively. For a sinusoidal drive current $I(t)$, and under the assumption that $B_m(t) = \mu H_m(t)$ with μ being a constant, the voltage generated in the secondary $V(t)$ should be sinusoidal and out of phase with the primary current.

The internal oscillator of an SR830 lock-in amplifier was used to generate $I(t)$. This was monitored by measuring the voltage across a 1 Ω resistor with small temperature coefficient in the primary loop. The lock-in amplifier was then used to demodulate $V(t)$ into its in-phase V_X and out-of-phase V_Y components (or equivalently $\dot{B}_m(t)$ being demodulated into $\dot{B}_{m,X}$ and $\dot{B}_{m,Y}$, as in equation (3.5)). The experiment was done at 1 Hz with $H_m(t)$ as small as possible, typically 0.1 A/m in amplitude, to measure the slope of the minor $B_m - H_m$ loops near the origin of the $B_m - H_m$ space.

The temperature of the core was measured continuously using the same thermocouple arrangement described previously. Measurements of V_Y as a function of temperature would then signify a change in μ with temperature. In general, we used ambient temperature variations for the measurements, similar to the procedure used for our axial shielding factor measurements.

The naive expectation is that the out-of-phase V_Y component should signify a nonzero μ, and the in-phase V_X component should be zero. In practice, due to a combination of saturation, hysteresis, eddy-current losses, and skin-depth effects, the V_X component is nonzero. It was found experimentally that keeping the amplitude of $H_m(t)$ small compared to the apparent coercivity ($\sim$ 3 A/m for the 0.16 cm thick material at 1 Hz frequencies) ensured that the V_Y component was larger than the V_X component. This is displayed graphically in Fig. 3.5, where the dependence of $\dot{B}_{m,Y}$ and $\dot{B}_{m,X}$ on the amplitude of the applied $H_m(t)$ is displayed, for a driving frequency of 1 Hz. Clearly the value of $\dot{B}_{m,X}$ can be considerable compared to $\dot{B}_{m,Y}$, for larger H_m amplitudes near the coercivity. At larger amplitudes, the material goes into saturation. Both $\dot{B}_{m,Y}$ and $\dot{B}_{m,X}$ eventually decrease as expected at amplitudes much greater than the coercivity.

To understand the behavior in Fig. 3.5, a theoretical model of the hysteresis based on the work of Jiles [116] was used. The model contains a number of adjustable parameters. We adjusted the parameters based on our measurements of $B_m - H_m$ loops including the initial magnetization curve. These measurements were performed separately from our lock-in amplifier measurements, using an arbitrary function generator and a digital oscilloscope to acquire them. The measurements were done at frequencies from 0.01 to 10 Hz. It was found that the frequency dependence predicted by Ref. [116] gave relatively good agreement with the measured $B_m - H_m$ loops once the five original (Jiles-Atherton [117, 118]) parameters were tuned.

For the parameters of the (static) Jiles-Atherton model, we used $B_s = 0.45$ T, $a =$ 3.75 A/m, $k = 2.4$ A/m, $\alpha = 2 \times 10^{-6}$, $c = 0.05$, which were tuned to our $B_m - H_m$ curve measurements. For classical losses, we used the parameters $\rho = 5.7 \times 10^{-7}$ Ω·m, $d =$ 1.6 mm (the thickness of the material), and $\beta = 6$ (geometry factor). These parameters were not tuned, but taken from data. For anomalous losses we used the parameters $w = 0.005$ m and $H_0 = 0.0075$ A/m, which we also did not tune, instead relying on the tuning performed in Ref. [116].

These parameters were then used to model the measurement presented in Fig. 3.5, including the lock-in amplifier function. As shown in Fig. 3.5, trends in the measurements and simulations are fairly consistent. The sign of $\dot{B}_{m,X}$ relative to $\dot{B}_{m,Y}$ is also correctly predicted by the model (we have adjusted them both to be positive, for graphing purposes). We expect that with further tuning of the model, even better agreement could be achieved.

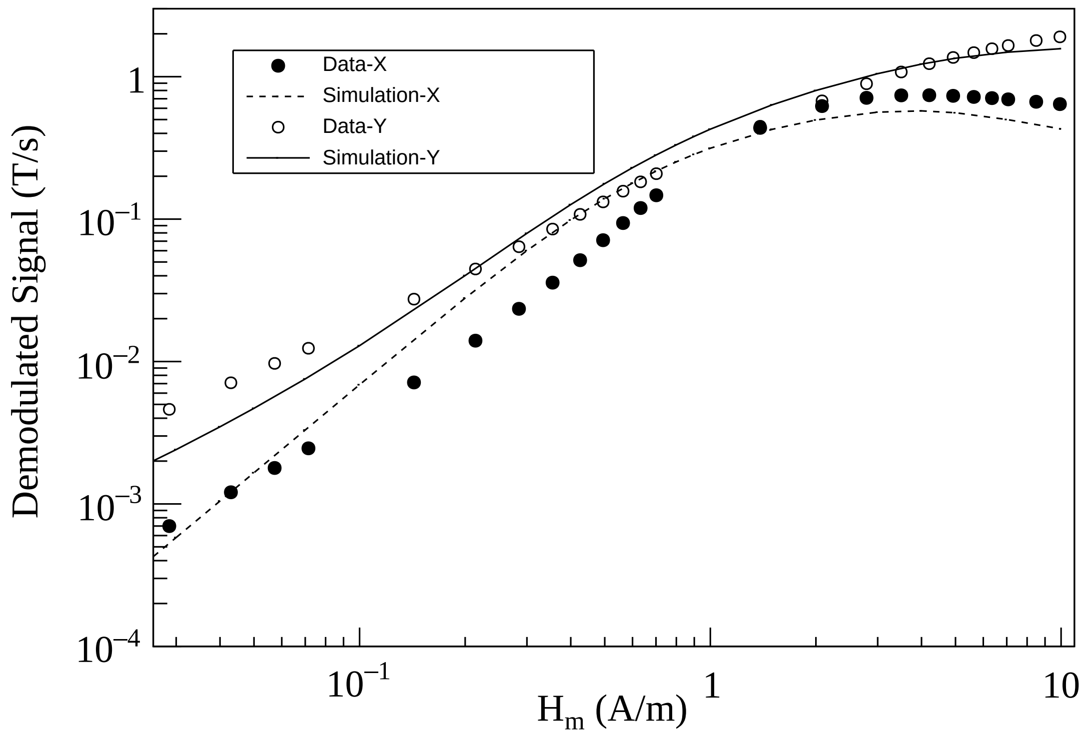

Figure 3.5: $\dot{B}_{m,X}$ and $\dot{B}_{m,Y}$ as a function of amplitude of the applied H_m field at 1 Hz. Points show the acquired data. Curves display the simulation based on the model described in the text.

The model of Ref. [116] makes no prediction of the temperature dependence of the parameters. Ideally, the temperature dependence of $\dot{B}_{m,Y}$ and $\dot{B}_{m,X}$ under various conditions could be used to map out the temperature dependence of the parameters. However, this is beyond the scope of the present work.

We make the simplifying assumption that temperature dependence of $\dot{B}_{m,Y}$ may be approximately interpreted as the temperature dependence of a single parameter μ, i.e. that

$$\frac{1}{\dot{B}_{m,Y}} \frac{d\dot{B}_{m,Y}}{dT} = \frac{1}{\mu} \frac{d\mu}{dT}. \tag{3.6}$$

Trial #	$\frac{1}{\dot{B}_{m,Y}}\frac{d\dot{B}_{m,Y}}{dT}$ (%/K)	core used
1	0.15	α
2	0.03	α
3	0.04	α
4	0.06	α
5	1.07	β
6	0.93	β
7	0.88	β
8	0.88	β
9	0.09	α
10	1.23	β
11	2.15	β
12	1.85	β
13	1.20	β
14	0.77	γ

Table 3.3: Summary of data acquired for the transformer core measurements. Three different witness cylinders, arbitrarily labeled α, β, and γ, were used for the measurements. A 1 Hz excitation frequency was used with amplitudes for H_m ranging from 0.1 to 0.3 A/m. Fluctuations in the temperature ranged from 21-24°C and measurement times over a 10-80 hour period are included. Other data acquired for systematic studies are not included in the table.

This is justified in part by our selection of measurement parameters (the amplitude of $H_m = 0.1$ A/m and a measurement frequency of 1 Hz) which ensure that $\dot{B}_{m,Y}$ dominates over $\dot{B}_{m,X}$.

We assign no additional systematic error for this simplification, and all our results are subject to this caveat. We comment further that in our measurements of the axial shielding factor (presented in Section 3.3.2), the same caveat exists. In that case the in-phase component dominates the demodulated fluxgate signal. In a sense, measuring $\mu(T)$ itself is always an approximation, because it is actually the parameters of minor loops in a hysteresis curve which are measured. In reality, our results may be interpreted as a measure of the temperature-dependence of the slopes of minor loops driven by the stated H_m.

Measurements of $\frac{1}{\dot{B}_{m,Y}}\frac{d\dot{B}_{m,Y}}{dT}$ as a function of T were made. In general, the data mimicked the behavior of the axial shielding factor measurements, giving a similar level of linearity with temperature as the data displayed in Fig. 3.3. Other similar behaviors to those measurements were also observed, for example: (a) when the temperature slope changed sign, $\dot{B}_{m,Y}$ would temporarily give a different slope with temperature, (b) the measured value of $\frac{1}{\dot{B}_{m,Y}}\frac{d\dot{B}_{m,Y}}{dT}$ depended on a variety of factors, most notably a dependence on which of the three witness cylinders was used for the measurement, and on differences between subsequent measurements using the same cylinder.

Table 3.3 summarizes our measurements of the relative slope $\frac{1}{\dot{B}_{m,Y}}\frac{d\dot{B}_{m,Y}}{dT}$ for a variety of trials, witness cylinders, and numbers of windings. The data show a full range of

$0.03 - 2.15\%/\text{K}$ for $\frac{1}{\mu}\frac{d\mu}{dT} = \frac{1}{\dot{B}_{m,Y}}\frac{d\dot{B}_{m,Y}}{dT}$, again naively assuming the material to be linear as discussed above. The sign of the slope of $\mu(T)$ was the same as the axial shielding factor technique.

A dominant source of variation between results in this method arose from properties inherent to each witness cylinder. One of the cylinders (referred to as β in Table 3.3) gave temperature slopes consistently larger $\frac{1}{\mu}\frac{d\mu}{dT} \sim 0.88 - 2.15\%/\text{K}$ than the other two $\frac{1}{\mu}\frac{d\mu}{dT} \sim 0.03 - 0.77\%/\text{K}$ (referred to as α and γ, with some evidence that γ had a larger slope than α). We expect this indicates some difference in the annealing process or subsequent treatment of the cylinders, although to our knowledge the treatment was controlled the same as for all three cylinders. Since our goal is to provide input to future EDM experiments on the likely scale of the temperature dependence of μ that they can expect, we phrase our result as a range covering all these results.

Detailed measurements of the effect of degaussing were conducted for this geometry. The ability to degauss led us ultimately to select a larger number of primary turns (48) so that we could fully saturate the core using only the lock-in amplifier reference output as a current source. A computer program was used to control the lock-in amplifier in order to implement degaussing. A sine wave with the measurement frequency (typically 1 Hz) was applied at the maximum lock-in output power. Over the course of several thousand oscillations, the amplitude was decreased linearly to the measurement amplitude (~ 0.1 A/m). After degaussing with parameters consistent with the recommendations of Refs. [**?** **?**], the measured temperature slopes were consistent with our previous measurements where no degaussing was done.

Other systematic errors found to contribute at the $< 0.1\%/\text{K}$ level were: motion of the primary and secondary windings, stability of the lock-in amplifier and its current source, and stability of background noise sources.

To summarize, the dominant systematic effects arose due to different similarly prepared cores giving different results, and due to variations in the measured slopes in multiple measurements on the same core. The second of these is essentially the same error encountered in our axial shielding factor measurements. We expect it has the same source; it is possibly a property of the material, or an additional unknown systematic uncertainty.

3.4 Relationship to nEDM experiments

Neutron EDM experiments are typically designed with the DC coil being magnetically coupled to the innermost magnetic shield. As discussed in Section 3.2, if the magnetic permeability of the shield changes, this results in a change in the field in the measurement region by an amount $\frac{\mu}{B_0}\frac{dB_0}{d\mu} = 0.01$.

The temperature dependence of μ has been constrained by two different techniques using open-ended mu-metal witness cylinders annealed at the same time as our prototype magnetic shields. We summarize the overall result as $0.0\%/\text{K} < \frac{1}{\mu}\frac{d\mu}{dT} < 2.7\%/\text{K}$, where the range is driven in part by material properties of the different mu-metal cylinders, and in part by day-to-day fluctuations in the temperature slopes.

We note the following caveats in relating this measurement to nEDM experiments:

- Although the measurement techniques rely on considerably larger frequencies and different H_m-fields than those relevant to typical nEDM experiments, we think it reasonable to assume the temperature dependence of the effective permeability should be of similar scale. For frequency, both techniques typically used a 1 Hz AC field, whereas for nEDM experiments the field is DC and stable at the 0.01 Hz level. Furthermore, in one measurement technique the amplitude of H_m was ~ 0.004 A/m and in the other was ~ 0.1 A/m. For nEDM experiments $H_m < 0.007$ A/m and is DC.

- Both measurement techniques extract an effective μ that describes the slope of minor loops in $B_m - H_m$ space. A more correct treatment would include a more comprehensive accounting of hysteresis in the material, which is beyond the scope of this work.

Assuming our measurement of $0.0\%/\mathrm{K} < \frac{1}{\mu}\frac{d\mu}{dT} < 2.7\%/\mathrm{K}$ and the generic EDM experiment sensitivity of $\frac{\mu}{B_0}\frac{dB_0}{d\mu} = 0.01$ results in a temperature dependence of the magnetic field in a typical nEDM experiment of $\frac{dB_0}{dT} = 0 - 270$ pT/K. To achieve a goal of ~ 1 pT stability in the internal field for nEDM experiments, the temperature of the innermost magnetic shield in the nEDM experiment should then be controlled to the < 0.004 K level if the worst-case dependence is to be taken into account. This represents a potentially challenging design constraint for future nEDM experiments.

As noted by others [119], the use of self-shielded coils to reduce the coupling of the B_0 coil to the innermost magnetic shield is an attractive option for EDM experiments. The principle of this technique is to have a second coil structure between the inner coil and the shield, such that the net magnetic field generated by the two coils is uniform internally but greatly reduced externally. For a perfect self-shielded coil, the field at the position of the magnetic shield would be zero, resulting in perfect decoupling, which is to say a reaction factor that is identically unity. For ideal geometries, such as spherical coils [120–122] or infinitely long sine-phi coils [123–125], the functional form of the inner and outer current distributions are the same, albeit with appropriately scaled magnitudes and opposite sign. More sophisticated analytical and numerical methods have been used extensively in NMR and MRI to design self-shielded gradient [126, 127], shim [128, 129], and transmit coils [125, 130], and should be of value in the context of nEDM experiments, as well. We are also pursuing novel techniques for the design of self-shielded coils of any arbitrary field profile and geometric shape [131].

3.5 Conclusion

In the axial shielding factor measurement, we found $0.6\%/\mathrm{K} < \frac{1}{\mu}\frac{d\mu}{dT} < 2.7\%/\mathrm{K}$, with the measurement being conducted with a typical H_m-amplitude of 0.004 A/m and at a frequency of 1 Hz. In the transformer core case, we found $0.0\%/\mathrm{K} < \frac{1}{\mu}\frac{d\mu}{dT} < 2.2\%/\mathrm{K}$, with the measurement being conducted with a typical H_m-amplitude of 0.1 A/m and at a frequency of 1 Hz.

The primary caveat to these measurements is that both measurements (transformer core and axial shielding factor) do not truly measure μ. Rather they measure observables related to the slope of minor hysteresis loops in $B_m - H_m$ space. They would be more appropriately described by a hysteresis model like that of Jiles [**?**], but to extract the temperature dependence of all the parameters of the model is beyond the scope of this work. Instead we acknowledge this fact and relate the temperature dependence of the effective μ measured by each experiment.

We think it is interesting and useful information that the two experiments measure the same scale and sign of the temperature dependence of their respective effective μ's. This is a principal contribution of this work.

In future work, we plan to measure $B_0(T)$ directly for nEDM-like geometries using precision atomic magnetometers. We anticipate based on the present work that self-shielded coil geometries will achieve the best time and temperature stability.

Chapter 4

Current UCN Facility at TRIUMF

The current vertical UCN cryostat at TRIUMF is the same UCN cryostat developed and tested at RCNP, Japan [132, 133]. In 2016, the cryostat was shipped to triumf and in 2017 it was installed at a dedicated a dedicated spallation neutron source for further UCN experiments. The main purpose of such experiments were for better understanding of the vertical UCN source and the design of the next generation UCN source. The 520 MeV cyclotron at TRIUMF provides up to 40 μA of proton beam that can be diverted onto a tungsten spallation target. The vertical UCN source is placed above the target and is surrounded by graphite blocks serving as neutron reflectors.

The vertical source was modified to fulfill the Canadian safety requirements at TRIUMF. Those include installing pressure relief valves on the cryostat and the UCN guides and additional radiation shielding requiring much longer UCN guides compared to RCNP. The current location of the vertical source is at the meson hall experimental area. A map of TRIUMF is shown in Fig. 4.1.

The unique feature of the UCN source at TRIUMF is the combination of spallation neutrons and superfluid helium for UCN production. Diffenet elements of the UCN facility at TRIUMF are presented below.

4.1 UCN Beam Line

TRIUMF produces negatively charged hydrogen ions from an ion source. These ions are then accelerated in the 520 Mev cyclotron in an outward spiral trajectory. A thin graphite stripper foil removes the electrons from the hydrogen ion while protons can pass through. The proton, because it is a positively charged particle, is deflected in the outward direction due to the magnetic field and is directed to a proton beam line. TRIUMF has four independent extraction probes with various sizes of foils to provide protons simultaneously to up to four beam lines.

The 120 μA beam (BL1A) enters the Meson Hall where the UCN facility is located. The vertical UCN source is designed for a maximum of 40 μA beam on target. As a result, only one third of the beam can go to the UCN experimental area and the rest is shared with different experimental facilities.

The microstructure of BL1A is in pulses with approximately 1 ms periods of beam followed by a 50-100 μs periods of no beam. This is shown in Fig. (4.2) [134]. A kicker magnet and the septum magnet kick away 1/3 of the beam from BL1A to BL1U and transport it to a conventional dipole (bender) magnet (See Fig. 4.3).

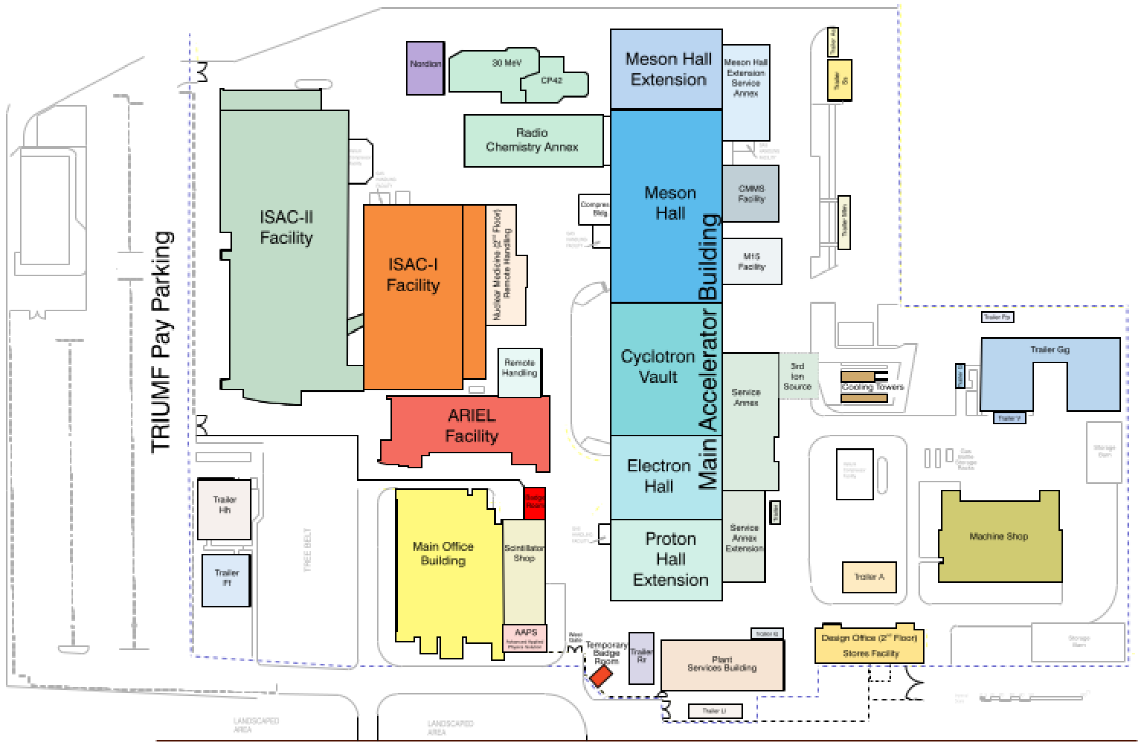

Figure 4.1: A map of TRIUMF. The UCN facility is located at the Meson Hall area shown in Blue.

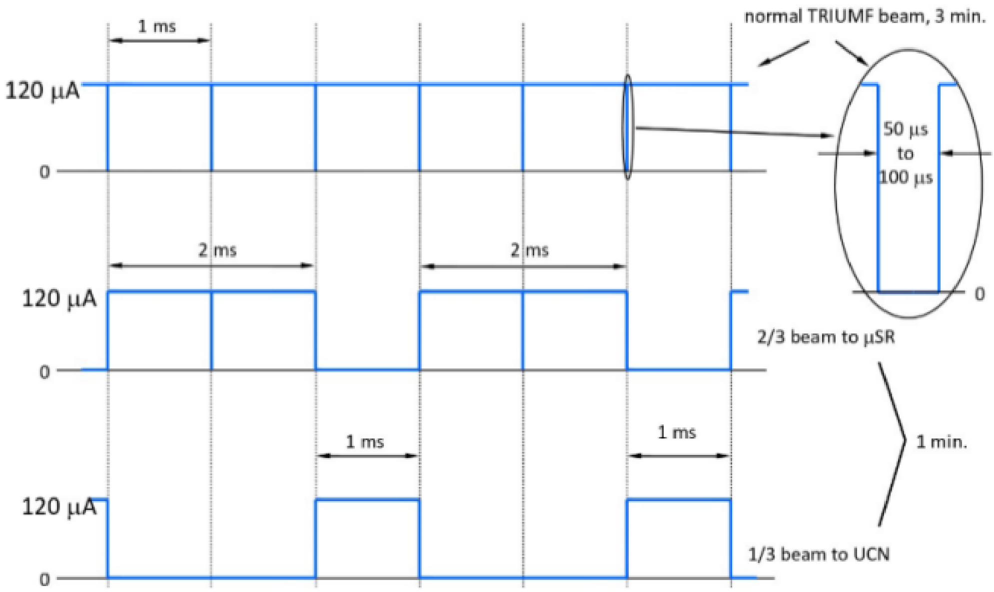

Figure 4.2: UCN beam structure. The top graph shows the 120 μA BL1A in 1 ms period of beam followed by a 50-100 μs of no beam. The middle graph shows the same beamline when the kicker magnet is on. The bottom graph shows the 1/3 of the beam that goes to the UCN area.

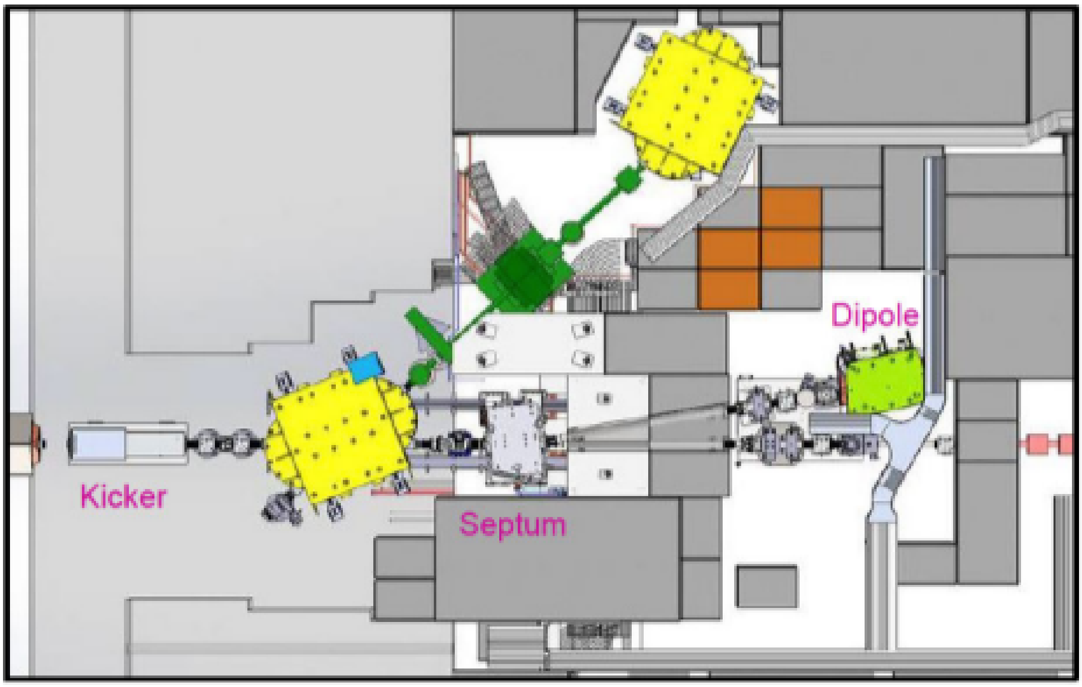

Figure 4.3: The kicker, septum and dipole (bender) magnets define the front two sections of BL1U.

After the bender magnet, the beam then passes through a cored shielding block and reaches the two quadrupole magnets providing the final focus of the beam onto a 12 cm thick tungsten spallation target. The target is located inside a hermetically-sealed target crypt, which also envelops the beamline exit window that defines the end of BL1U. Upstream of the beamline window, there is a collimator to reduce the halo from the proton beam, as well as to help reduce the amount of neutrons and photons streaming back into the beamline from the target region (the collimator also increases the impedance for the passage of gas arising from any target or window failure, to allow time for the cyclotron fast valves to close). This last part of the beamline also contains a variety of beam position and current monitors. The spallation target and UCN source, located downstream of the beamline-exit window, are enclosed in a large shielding pyramid Fig 4.4.

4.2 Tungsten Spallation Target

The spallation target is located at the downstream end of BL1U. The UCN spallation target comprises a series of rectangular blocks, adding up to roughly one stopping length (11 cm) of tungsten, with a cross-section of $\sim 6 \times 8$ cm^2 (see Fig. 4.5). This geometry is very similar to (and motivated by) the neutron spallation target design used at KEK (KENS facility) [135]. The target requires a support and cooling system, and is designed to allow for remote-handling and ease of servicing. The target-cooling and remote-handling systems are designed for an instantaneous proton current of 40 μA (10 μA time-averaged). The target is being water-cooled. A coating of tantalum prevents corrosion by the water cooling system. An extraction system allows to exchange the target when necessary.

Stuff still need to be added here.

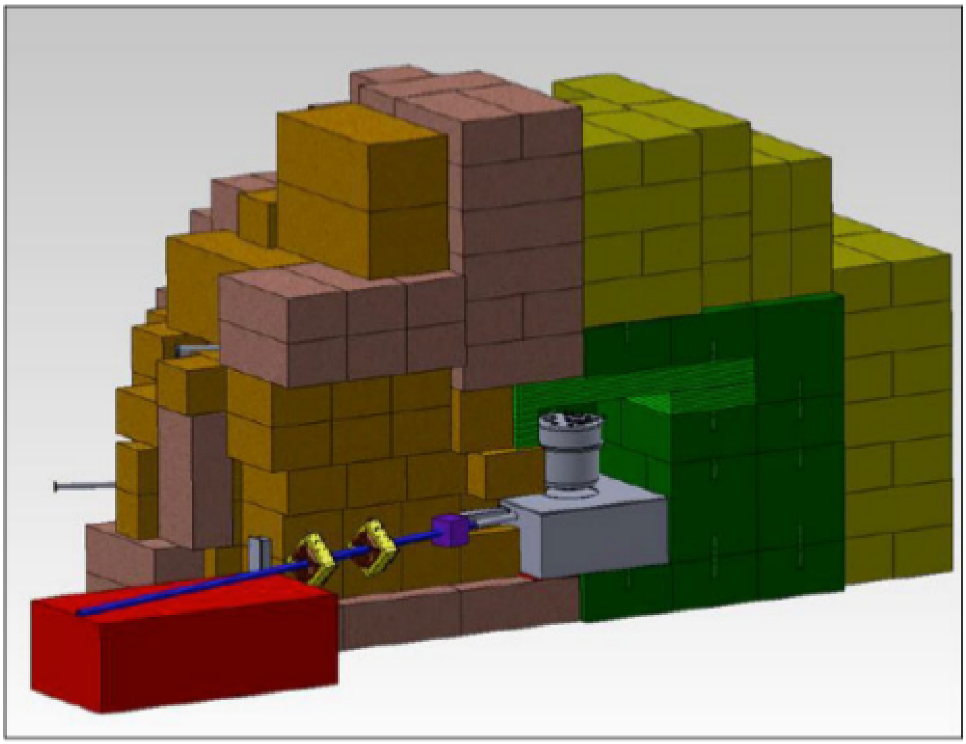

Figure 4.4: Two quadrupole magnets which focus the proton beam onto a 12 cm thick tungsten spallation target, located inside a hermetically-sealed target crypt. Also shown is the UCN shielding pyramid, which encases both the spallation target and the UCN source, and is designed to meet the dose rate requirements specified by the TRIUMF Safety Group.

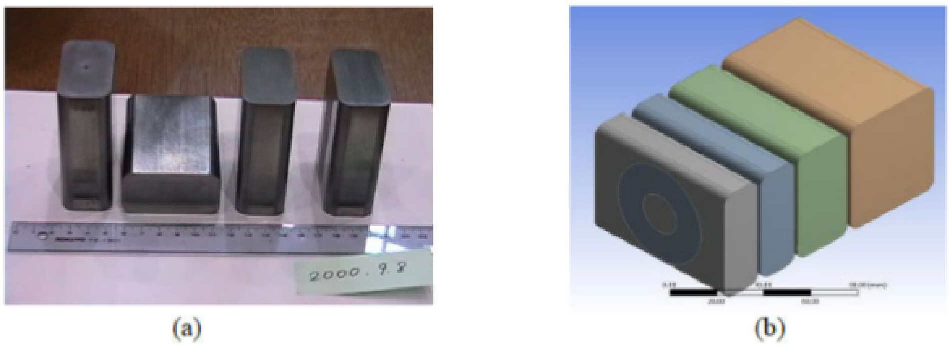

Figure 4.5: (a) Tungsten Target Blocks from the spallation target at KEK. The target blocks are plated with tantalum. (b) Present design for the tungsten spallation target at the TRIUMF UCN facility. The target blocks have a cross-section of 5.7×7.8 cm^2 , and thicknesses of 2.0, 2.0, 3.0, and 5.0 cm, respectively.

4.3 Radiation Sheilding

4.4 Vertical UCN Source at TRIUMF

4.4.1 D_2O Moderator

4.4.2 Helium Circulation

4 Kelvin Reservoir

1 Kelvin Pot

^{3}He Pot

Isopure Helium

4.5 Stages of UCN Production In The Source

At TRIUMF, UCN is produced in three stages: Spallation, moderation and conversion. Fig. (4.6) shows a schematic of this process.

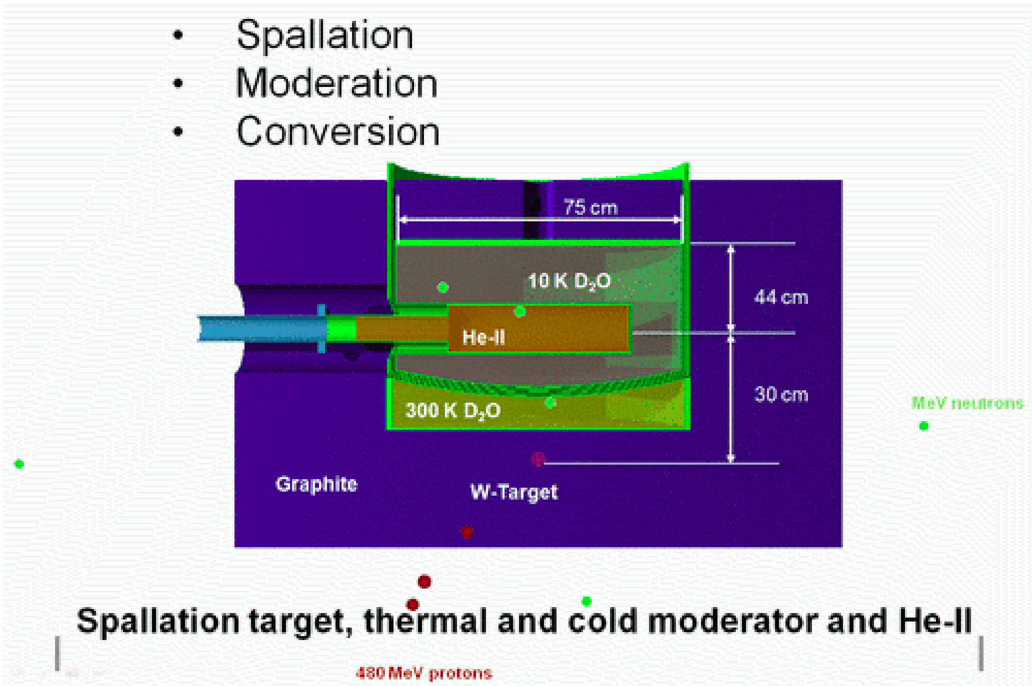

Figure 4.6: blah

The neutrons are produced through the spallation process by hitting a Tungsten target by the proton beam. Spallation is refered to a nuclear reaction where high energy particles interact with atomic nucleus. This process creates many high energy neutrons and background radiation. The target is surrounded by several blocks of lead and graphite. These fast neutrons are reflected and moderated down and enter the warm D_2O moderator at room temperature (300 K) and become thermal neutrons with an energy of 0.025 eV and the speed of 2.2 km/s.

Iced heavy water at 20 K is used as a cold moderator. After passing through the warm D_2O, thermal neutrons enter the the cold moderator and become cold neutrons. These neutrons have the speed of several hundreds of meter per second.

The last stage is when the slow neutrons enter the isotopically pure superfluid helium at 0.84 to 0.92 K. UCN is produced as a result of phonon transitions inside the superfluid helium as discussed in section 1.3.2.

4.6 D_2O Solidification

The D_2O vessel has a capacity of 100 L. At first, 14 L of liquid D_2O gets injected to the vessel. This is followed by adding 11 L of D_2O to the vessel over 8 times. After filling up the vessel, Gifford McMahon refrigerators solidify the heavy water and further cool it down to 10 K. The process of icing the heavy water takes about 6 days and cooling it down takes another XXX days.

4.7 Data Acquisition System??

Here talk about the EPICS and PLC and put pictures. I can also use stuff from student's reports.

4.8 UCN Detectors

Talk about how each detector works.

4.8.1 ^{6}Li Detector

The main detector used during the UCN measurements (See Chapter 5) is a ^{6}Li glass based scintillator detector designed and built at the University of Winnipeg for the TUCAN nEDM experiment at TRIUMF [94]. Since ^{6}Li has a high neutron capture cross-section (order of 10^5 bn) at UCN energies, the scintillator glass is doped with it. The charged particles in the reaction

$$^6Li + n \rightarrow \alpha(2.05 \text{ MeV}) + t(2.73 \text{ MeV}) \tag{4.1}$$

are detected. To reduce the effect of α or triton escaping the glass, a layer of 60 μm thick depleted ^{6}Li glass (GS30), on top of a layer of 120 μm thick dopped ^{6}Li (GS20) were optically bonded. This design allows the resultant particles to deposit all of their energy within the scintillating glass. Table 4.8.1 shows the content and density of those ^{6}Li scintillators.

Scintillator	GS20 (^{6}Li Enriched)	GS30 (^{6}Li depleted)
Total Li content (%)	6.6	6.6
^{6}Li fraction (%)	95	0.01
^{6}Li desity (cm^{-3})	1.716×10^{22}	1.806×10^{18}

Table 4.1: Properties of the glass scintillators

Making the scintillating Li glass as thin as possible reduces the sensitivity to γ-ray scintillating backgrounds and and thermal neutron captures. The mean range of the α is 5.3 μm and the mean range of the triton is 34.7 μm. This means that if the thickness of the scintillator is less than 50 μm, the resultant particles escape before stopping which gives rise to an efficiency loss. In order to handle high UCN rates of up to $\tilde{1}$ MHz, the ^{6}Li detector face is segmented into 9 tiles (See Fig. 4.7). The scintillation light is then guided through ultra-violet transmitting acrylic light-guide to its corresponding Photomultiplier Tube (PMT) outside the vaccum region of the detector.

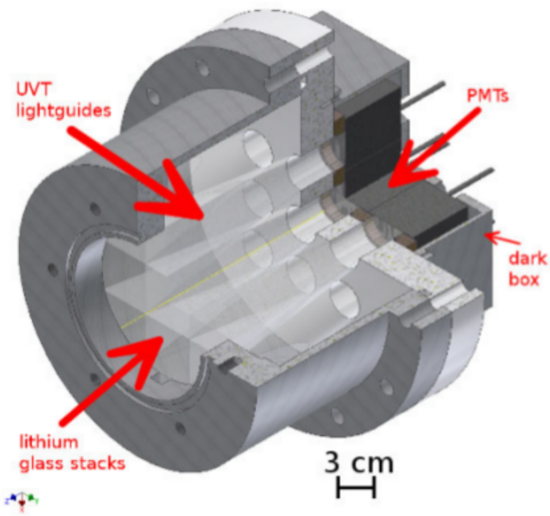

Figure 4.7: 3D drawing of the ^{6}Li detector and its enclosure. The enclosure is made of Al, and the rim of the adapter flange which UCN can hit is ccoated with 1 μm Ni by thermal evaporation.

The data acquisition with this detector includes a CAEN V1720 digitizer which has a Pulse-Shape Discrimination (PSD) firmware that triggers on pulses below a certain threshold for each channel. Every 4 ns the digitizer samples the waveform which is then digitized to a voltage on a 2 V scale into an ADC value between 0 and 4096. Each channel of the digitizer sends a trigger whenever the number of counts in the ADC goes below a certain baseline (pedestal) value. The PSD calculates the sum of the signal below the baseline for two time windows: $t_s = 40$ ns (short gate) and $t_L = 200$ ns (long gate). The short gate is chosen in a way to contain all of the charge for the γ-ray interactions in the light-guide. The ADC sum for during the long gate below the baseline is calle Q_L (read charge long) and for during the short gate below the baseline is called Q_S. Charge long has the total charge deposti for the neutron capture events. The PSD value is defined as

$$\mathrm{PSD} = \frac{(Q_L - Q_S)}{Q_L} \tag{4.2}$$

which is the amount of charge in the tail of an event.

Jamieson *et al.* showed that the absolute efficiency of this detector is $89.7^{+1.3}_{-1.9}$ % with a background contamination of 0.3 ± 0.1 % [94]. The detector is stable at the 0.06 % level or better, and that the variation in the efficiency between the detector tiles is less than 5 %.

4.8.2 ^{3}He Detector

Chapter 5

UCN Production and Detection

The first UCN at TRIUMF (Nov. 2017) were produced by using the vertical UCN source described in Sec. **??**. The spallation neutrons were converted to UCN through phonon excitation in the isotopically pure superfluid helium. During data taking several measurements were performed for better understandting of the vertical UCN source and to help design the next generation UCN source. In this chapter, the experiments are described and the result are shown.

Fig. 5.1 is a simple schematic of the UCN production and detection volume. Here volume V_1 is the production volume before the valve where N_1 number of UCN is produced, V_2 is the secondary volume where N_2 number of UCN enters after opening the valve , and V_3 is the detector volume with N_3 number of UCN.

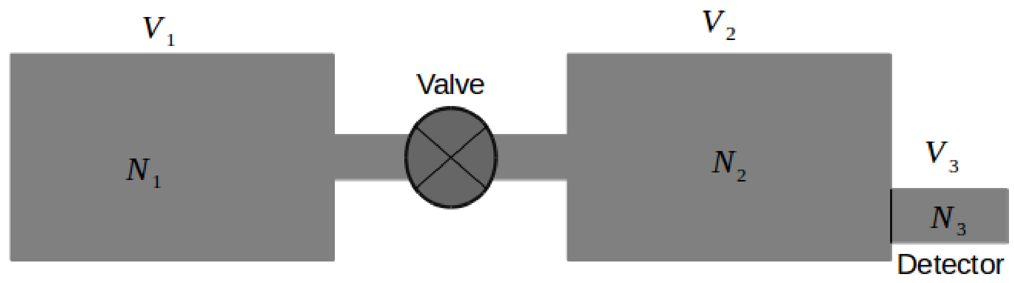

Figure 5.1: Schematic drawing of a UCN source. V_1 is the production volume with N_1 number of UCN, V_2 is the secondary volume where N_2 number of UCN exist and V_3 is the detector with N_3 number of UCN.

When the beam is on and the valve is closed, the number of UCN in V_1 goes up while the total number of UCN in V_2 and V_3 is zero. This is described as

$$\frac{dN_1}{dt} = P - \frac{N_1}{\tau_1} \tag{5.1}$$

where P is the UCN production rate in the source as describe in Sec. 1.4.2 and τ_1 is the UCN storage lifetime in the source.

After the beam is turned off, the valve is opened and the UCN travels to the volume V_2 and eventually V_3. The valve is usually left open for 2 to 3 minutes. The UCN trade between V_1, V_2 and V_3 is described by the differential Eqn. 5.2.

$$\begin{aligned}\frac{dN_1}{dt} &= -\frac{N_1}{\tau_{c,1}} - \frac{N_1}{\tau_1} + \frac{N_2}{\tau_{c,2}} \\ \frac{dN_2}{dt} &= \frac{N_1}{\tau_{c,1}} - \frac{N_2}{\tau_{c,2}} - \frac{N_2}{\tau_2} - \frac{N_2}{\tau_{c,3}} \\ \frac{dN_3}{dt} &= \frac{N_2}{\tau_{c,3}}.\end{aligned} \tag{5.2}$$

In these equations, $\frac{dN_1}{dt}$ shows the change in the UCN counts over time in V_1, $\frac{dN_2}{dt}$ shows the change in the UCN counts in V_2 and $\frac{dN_3}{dt}$ is change in the UCN count in V_3 which is the detector all after the valve is opened.

The total number of UCN in V_1 depends on three things. The UCN that get into V_2 $\left(\frac{N_1}{\tau_{c,1}}\right)$, the UCN that is lost with the storage lifetime of τ_1, and the UCN that bounce back from V_2 to V_1 $\left(\frac{N_2}{\tau_{c,2}}\right)$.

In V_2, some UCN cross from V_1 to V_2 $\left(\frac{N_1}{\tau_{c,1}}\right)$, some get lost with the lifetime of τ_2 $\left(\frac{N_2}{\tau_2}\right)$, some cross the gate valve to go back to V_1 $\left(\frac{N_2}{\tau_{c,2}}\right)$and some get to the detector $\left(\frac{N_2}{\tau_{c,3}}\right)$. The rate of the UCN detection $\frac{dN_3}{dt}$ is the number of UCN crossing from V_2. The end of the measurement cycle is determined by the valve closing time.

Solving these equation could give an estimate of how many UCN exist in each volume. The process described above is refered to the UCN production in *batch mode*. The UCN rate for 1 μA beam current and 60 s irradiation time is shown in Fig. 5.2.

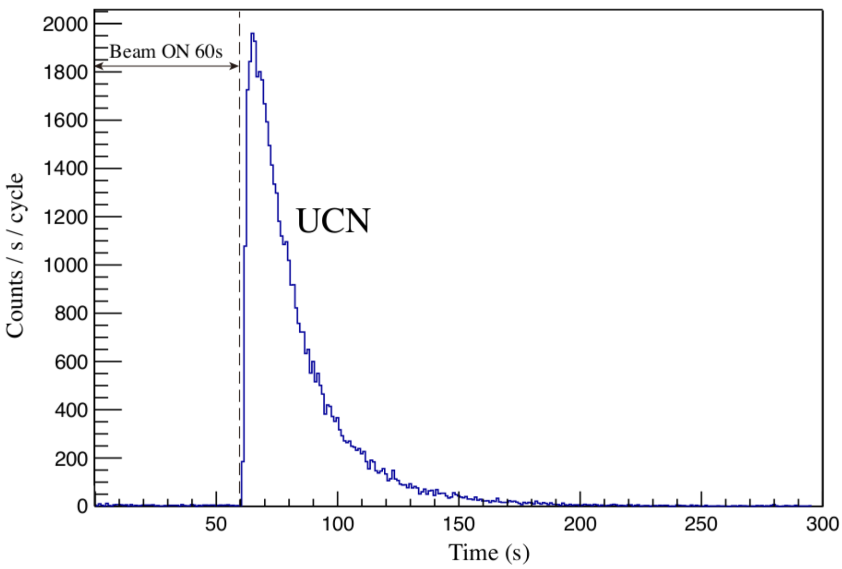

Figure 5.2: The figure shows the UCN rate at 60 s irradiation time and 1 μA beam current. In this case, the UCN gate valve is opened immediately after the end of irradiation. At this time, the UCN rate reaches the peak of about 2000 UCN/s. The UCN rate decays down to zero. The Valve is left open for 120 s.

A 3D drawing of the experimental setup is shown in Fig. 5.3. In this case, V_1 is the UCN source bottle and the horizontal section of the UCN guide before the UCN gate valve and V_2 and V_3 are the volumes after the UCN valve and the detector volume respectively.

Another possible mode of operation is when we leave the UCN valve open while irradiating the target. This is called the *steady-state* mode where we have a constant stream of UCN to the main detector.

3

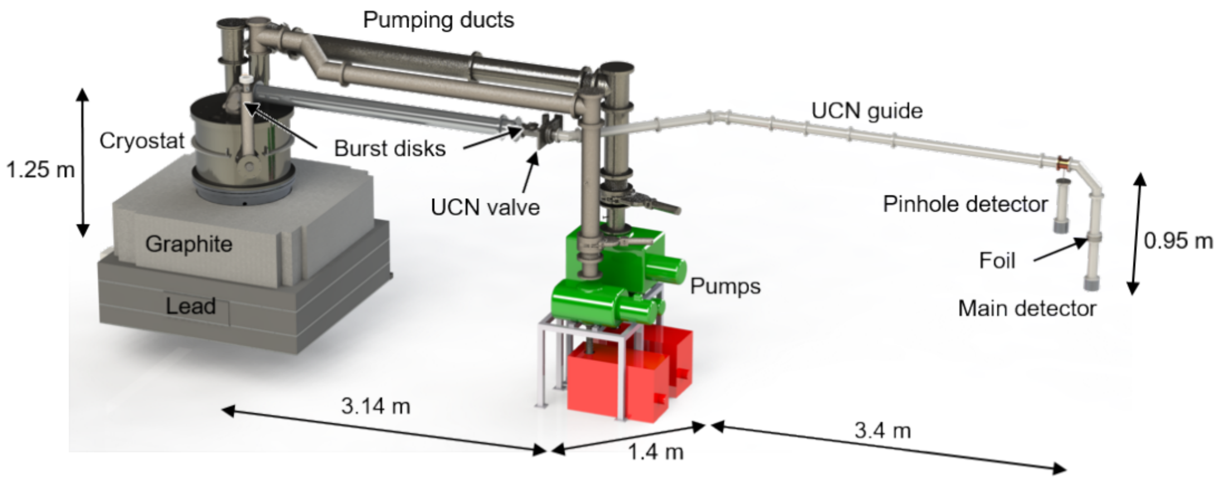

Figure 5.3: The UCN source and the guide geometry at TRIUMF

The following sections are focused on the result of the UCN yield optimization, the UCN storage lifetime measurements, the two detector comparisons and the UCN guide transmission measurements.

5.1 Data Quality Checks

The main detector for most of the collected data is the ^{6}Li glass based scintillator detector which described in Sec. 4.8.1. Before using the collected data to extract the desired information, it is critical to make sure that the detector was working as expected.

The PSD versus Q_L distribution from a UCN data run is shown in Fig. 5.4 for all the PMTs combined. This is the most useful way of separating the signal and background. Here the UCN events are mainly around the PSD value of 0.5 and Q_L between 3000 and 12000. The events at PSD ~ 0 represent the γ-rays in the lightguides. To get the actual UCN counts, a PSD cut of 0.3 and a Q_L cut of 2000 were applied. This ensures that only the UCN events are counted represented by the central oval-shaped region. Out of all 9 channels, the centeral channel counts the most number of UCN events while the corner channels receive the least as expected. Fig. 5.5.

5.2 UCN Count Measurement

The total number of produced UCN in the vertical source, N, at a certain time t$_i$ when the UCN valve is closed is the integration of eqn. 5.1

$$N = P\tau_1 \left[1 - \exp\left(\frac{t_i}{\tau_1}\right)\right] \tag{5.3}$$

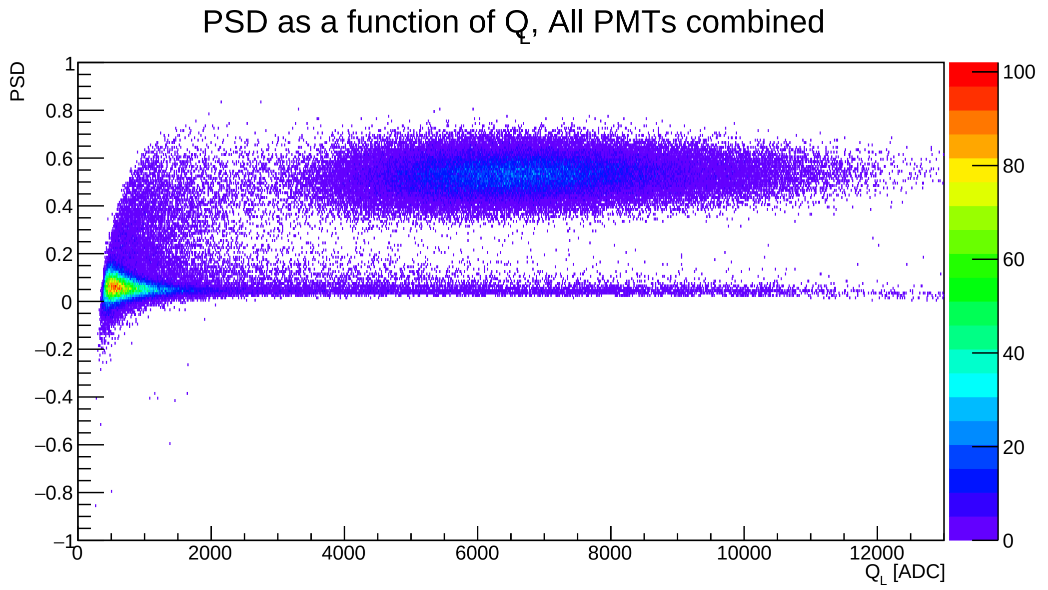

Figure 5.4: PSD versus Q_L for all of the PMTs for a standard 1 μA proton beam current and 60 s target irradiation storage lifetime measurement.

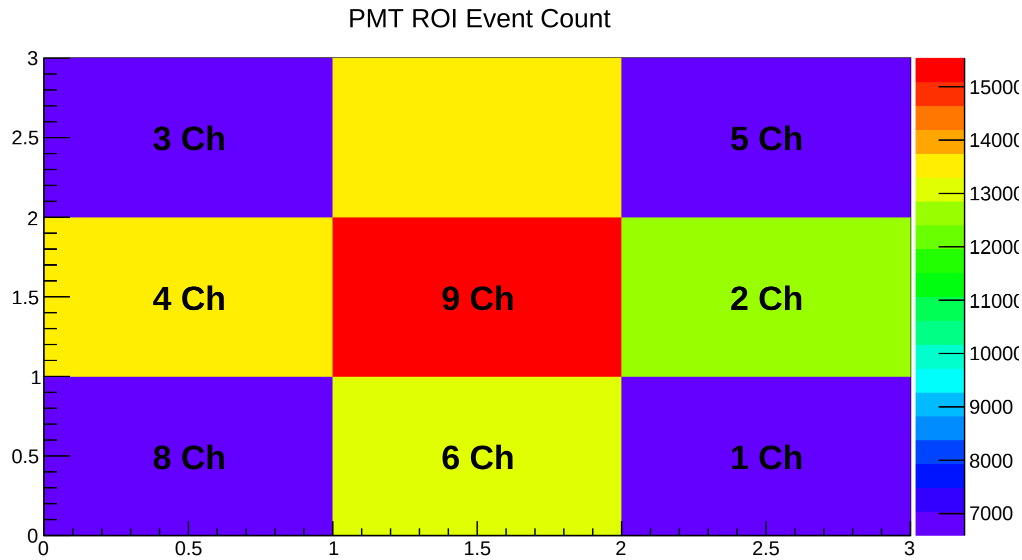

Figure 5.5: Number of UCN events for each channel. The total number of UCN events decrease as we move toward the corner channels.

where the UCN storage lifetime τ_1 is given by

$$\frac{1}{\tau_1} = \frac{f_{\mathrm{He},1}}{\tau_{\mathrm{He}}} + \frac{1}{\tau_{\mathrm{wall},1}}. \tag{5.4}$$

The storage lifetime consists of two terms: the upscattering rate in the superfluid helium and the loss rate in the UCN guide walls. The volume in which these UCN are produced consists of the UCN bottle as well as the horizontal guide section before the gate valve (See Fig. 5.3).This volume is not fully filled with the superfluid helium. As a result, $f_{\mathrm{He},1}$ is the probablity of UCN being in the superfluid helium and $\frac{f_{\mathrm{He},1}}{\tau_{\mathrm{He}}}$ is the upscattering rate in the superfluid helium which is a function of the superfluid helium temperature (See Sec. 1.4.2. The loss rate in the guide walls is $\frac{1}{\tau_{\text{wall},1}}$.

After the valve is opened, the total UCN lifetime is

$$\frac{1}{\tau_2} = \frac{f_{\text{He},2}}{\tau_{\text{He}}} + \frac{1}{\tau_{\text{wall},2}} + \frac{1}{\tau_d} \tag{5.5}$$

where τ_d^{-1} is the loss rate in the detector, $f_{\text{He},2}$ is the probability of UCN being in the superfluid helium and $\tau_{\text{wall},2}{}^{-1}$ is the UCN guide loss rate in this case where the valve is open and the target irradiation is stopped. Fig. 5.6 shows three measurement cycles at 1 μA beam current and 60 second irradiation time with zero second delay time for opening the UCN valve. The dashed lines indicate the start of the irradiation for a cycle, the dotted lines show the end of irradiation which in this case is open to the UCN valve open time. The solid lines shows the valve close time.

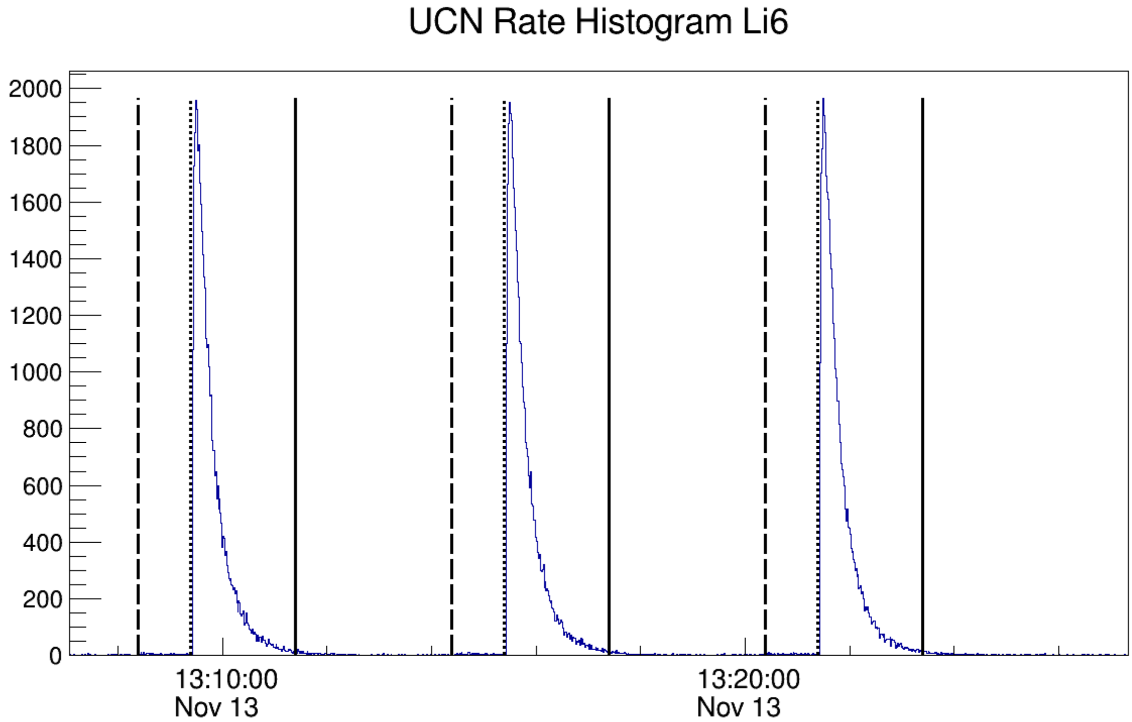

Figure 5.6: Three measurement cycles for 1 μA beam current, 60 s irradiation time and 0 seconds cycle delay time. The dashed line shows the start of the target irradiation, the dotted line shown the end of the irradiation and the valve open time for each cycle and the solid line shows the end of a cycle which is the valve close time.

The total UCN counts are given by the integration of all the UCN events for the duration of the valve open time. However, this method of counting includes the measured background UCN as well. To subtract the background counts from the actual UCN counts, the UCN background rate is calculated during the valve closed time for cycle (i-1) and the irradiation start time for cycle i. This rate is then multiplied by the valve open duration time and it gives an estimate of the total background UCN counts which is typically less than 5 UCN/s. The subtraction of the latter from the total UCN counts gives the actual UCN counts produced by the isopure helium converter.

At low and moderate UCN counts, the statistical uncertainty is readily available by taking the square root of the number of measured events, as follows conveniently from Poisson statistics [136].

Fig. 5.7 shows the total UCN counts versus the applied proton beam current in μA at 60 s irradiation time. At lower beam currents, the total UCN counts increase linearly with the proton beam current. The dashed line shows the extrapolation to higher beam current in an ideal case. However, at higher beam currents the total UCN counts deacreses due to the increase in the heat load on the isotopically pure superfluid helium and its temperature. The upscattering rate in the superfluid helium is proportional to its temperature as T^7 (See Sec. 1.4.2).

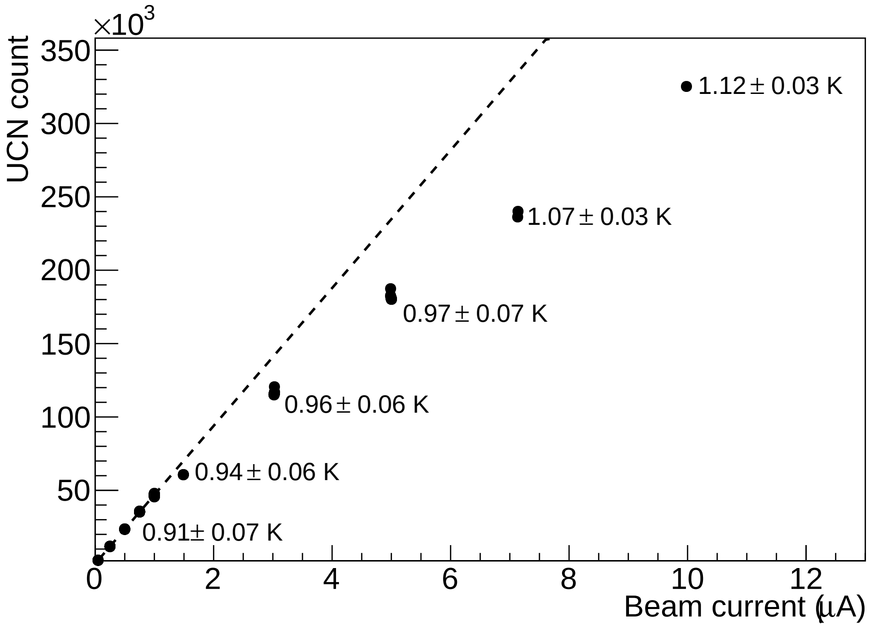

Figure 5.7: The total UCN counts versus the applied proton beam current. The labelas show the average superfluid helium temperature for that measurement. The dashed line is fit to the UCN counts at low beam current.

The labels in the graph show the average temperature during the measurement cycle. Four temperature sensors were used to measure the superfluid helium temperature: TS11, TS12, TS14 and TS16. The location of these sensors are shown in Fig. 5.8. Temperature sensor TS11 is located at the UCN heat exchanger bottom while the temperature sensor TS14 is located at the UCN heat exchanger top. The temperature sensor TS12 is located at the UCN double tube bottom while the temperature sensor TS16 is located at the UCN double tube top. At low temperature around 0.8 K these temperature sensors show a maximum of 0.1 K discrepancy with TS16 showing the highest value and TS12 showing the lowest value.

The total UCN count is optimized by irradiating the target with different proton beam currents and different irradiation times. The result is shown in Fig. 5.9. At higher beam currents, the saturation time constant decreases due to the higher heat load and faster temperature increase in the superfluid helium. At higher beam currents and longer irradiation times the total measured UCN counts are below the exponential extrapolation due to the higher temperature and higher upscattering rate in the superfluid helium.

The result shown so far achieved in the batch mode of operation. In addition to such measurements, the UCN rate at higher beam currents in the steady-state mode were

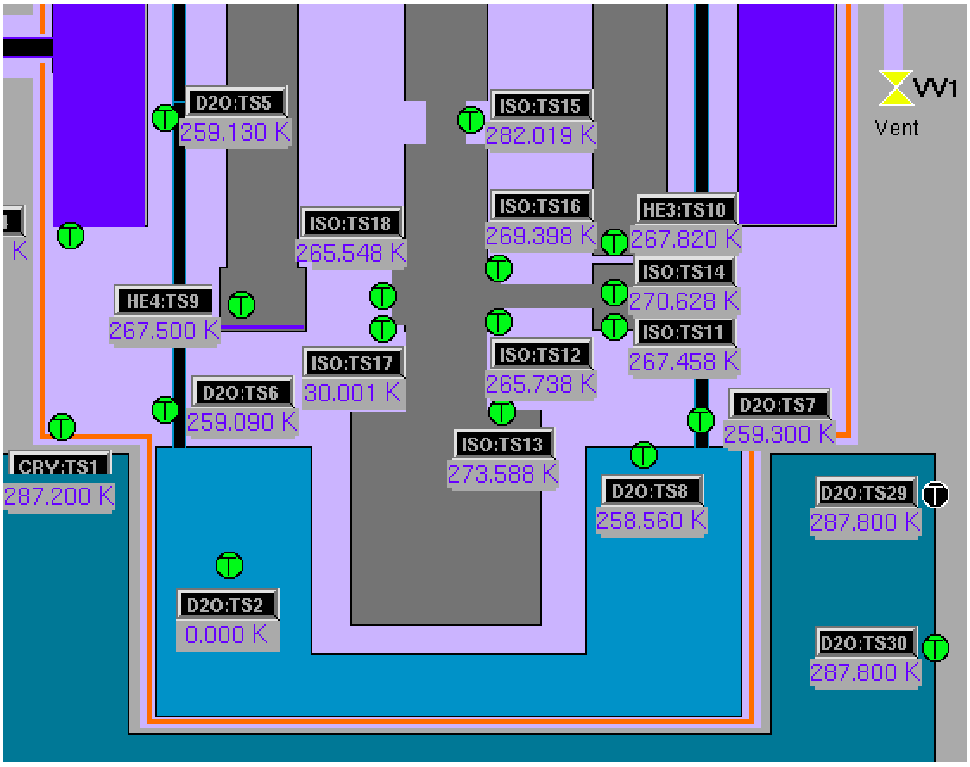

Figure 5.8: Screenshot of the Epics temperature monitoring screen. TS11 is located at the UCN head exchanger bottom, TS12 is located at the UCN double tube bottom, TS14 is located at the heat exchanger double tube top and TS16 is located at the UCN double tube top. For further information about the source schematic see Sec. 4.4

measured. In these measurements, the valve was left open and the target was irradiated for 10 min. A typicall UCN rate graph for 3 μA beam current and 10 minute irradiation time is shown in Fig. 5.10. The maximum UCN rate is achievable at the start of target irradiation. As the irradiation continues, the heat load on the cryostat increases the temperature and the upscattering rate in the superfluid helium. As a result, the UCN rate decreases. The change in the temperature is shown in Fig. 5.11.

The steady-state UCN rate measurements were conducted at different proton beam currents leading to different temperature changes for all temperature sensors. The result of all those measurements are shown in Fig. 5.12. In this figure, the vertical axis is the measured UCN rate normalized to the proton beam current and the horizontal axis shows the temperature of the isotopically pure superfluid helium for all the temperature sensors.

The detected rate of the detected UCN is given by

$$R = \frac{P\tau_3}{\tau_d} = \frac{P\tau_d^{-1}}{\tau_{\text{wall},2}^{-1} + \tau_d^{-1} + f_{\text{He},3}\tau_{\text{He}}^{-1}} \tag{5.6}$$

where τ_d^{-1} is the loss rate in the detector, $\tau_{\text{wall},2}{}^{-1}$ is the UCN guide wall loss and τ_{He}^{-1} is the loss rate in the superfluid helium.

Assuming $\tau_{\text{He}}^{-1} = B\,(T)^a$ the Eqn. **??** could be written as

$$R(T) = \frac{c}{1 + b\left(\frac{T}{1\,\text{K}}\right)^a} \tag{5.7}$$

which can be used to fit the data shown in Fig. 5.12. Since the four temperature sensors

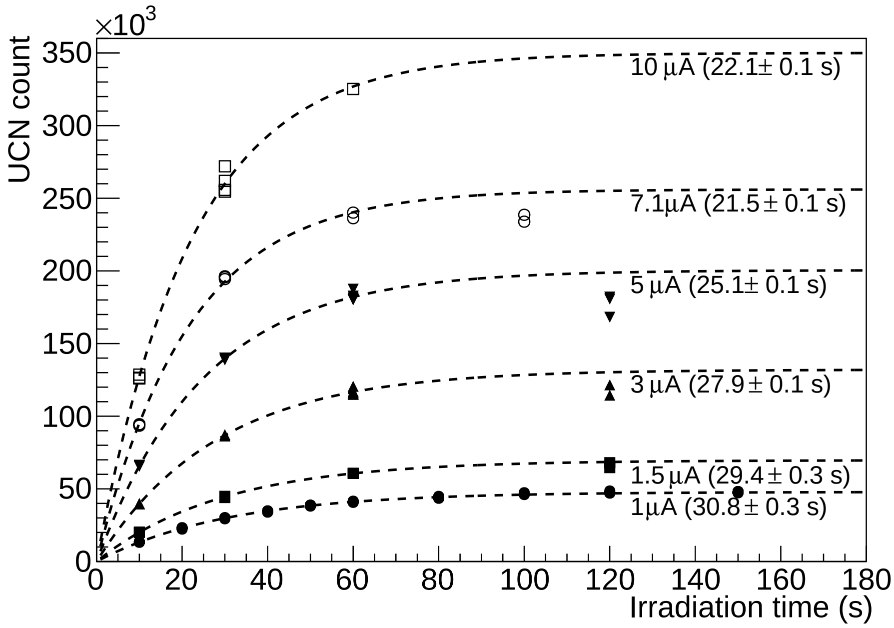

Figure 5.9: Number of UCNs extracted from the source after irradiating the target for different times with different beam currents. The dashed lines extrapolate the data for irradi- ation times below 60 s using exponential saturation curves. The labels show the saturation time constant for each beam current.

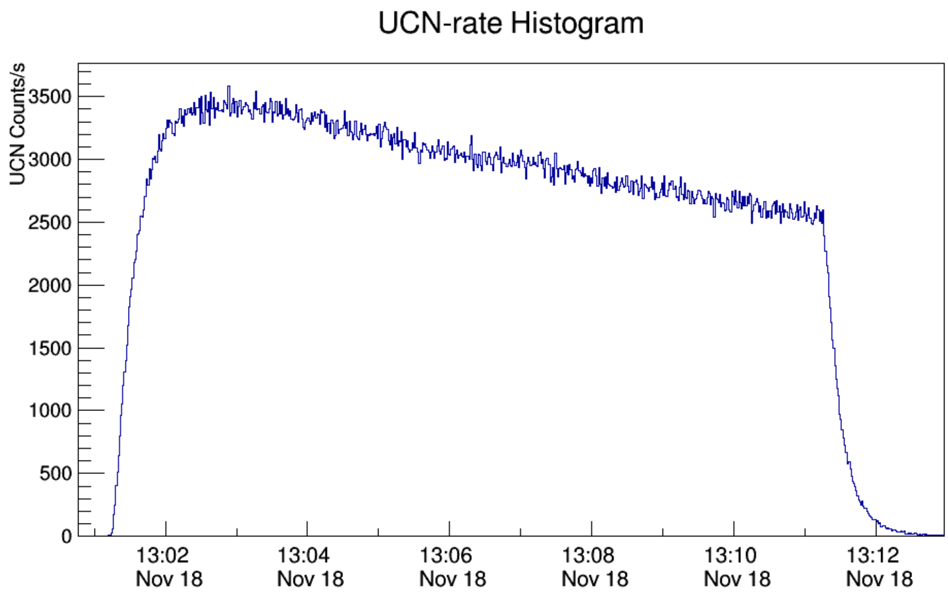

Figure 5.10: The UCN rate at 3 μA beam current at 10 min irradiation time at the steady-state mode of operation. The UCN valve is left open throughout the measurement cycle. Quickly after the start of the target irradiation the UCN rate in the detector goes up. The target irradiation creates heatload on the cryostat and superfluid helium which gives rise to a slow temperature increase in the source. As a result, the UCN rate goes down due to the higher upscattering rate.

in the superfluid helium deviate by up to 0.1 K, the rate for each temperature sensor is fitted individually (See Fig. **??** and table 5.1), and considered their differences systematic

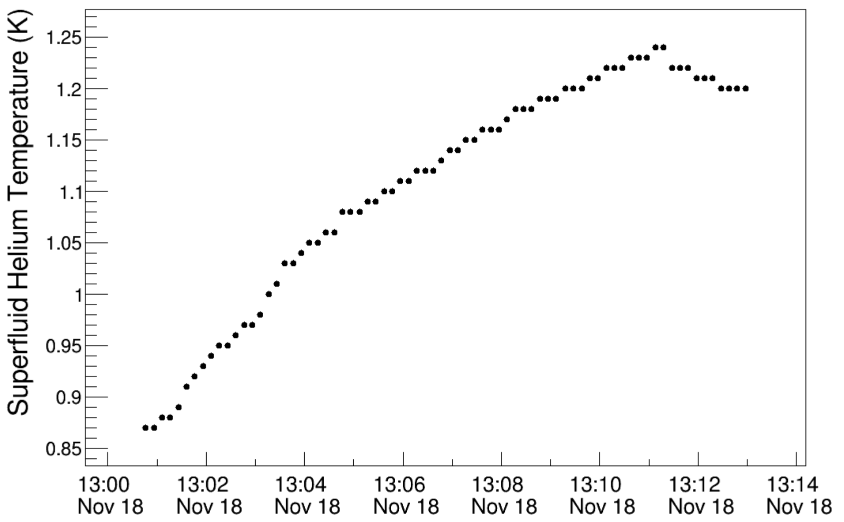

Figure 5.11: The temperature of the superfluid helium (TS12) for the steady state mode of operation at 3 μA beam current and 10 min target irradiation. After the irradiation stops, the temperature starts to go down.

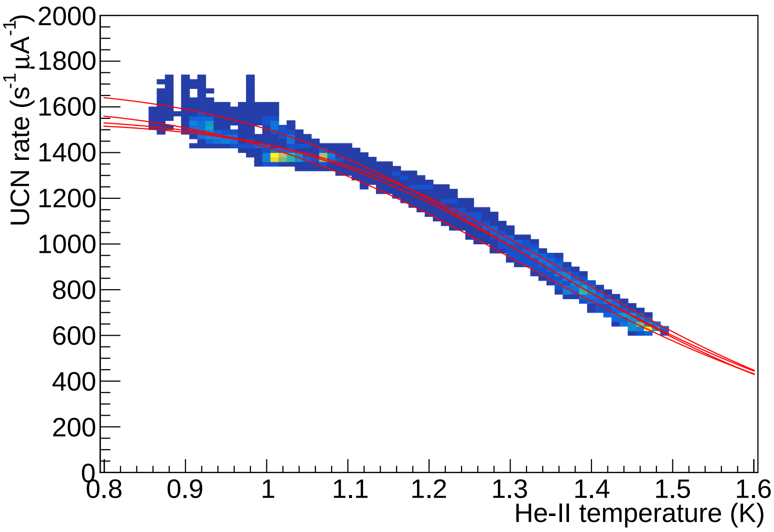

Figure 5.12: Histogram of measured UCN rates and temperatures from all four temperature sensors while the target is continuously irradiated with the UCN valve open. The four solid lines are fits of equation 5.7 to the data of each individual tem- perature sensor.

Temp. sensor	a	b	c (s^{-1})
TS11	7.55 ± 0.03	0.0697 ± 0.0009	1535 ± 1
TS12	6.48 ± 0.03	0.1293 ± 0.0016	1606 ± 2
TS14	7.34 ± 0.03	0.0832 ± 0.0011	1555 ± 2
TS16	6.67 ± 0.04	0.1215 ± 0.0019	1685 ± 3

Table 5.1: Parameters determined by fitting equation 5.7 to the measured rates shown in fig. **??** for each individual temperature sensor.

uncertainties. The exponent a can be directly determined this way, giving

$$a = 7.02 \pm 0.02_{\text{stat.}} \pm 0.53_{\text{syst.}}, \tag{5.8}$$

which is in good agreement with the theoretical prediction of $a = 7$ (see Sec.1.4.2). Here the statistical error comes from the fit and the systematic error comes from the temperature difference from the sensors and their propagated error.

The other parameters are

$$b = \frac{f_{\text{He},3} B}{\tau_{\text{wall},2}^{-1} + \tau_d^{-1}} = 0.0995 \pm 0.0007_{\text{stat.}} \pm 0.0298_{\text{syst.}} \tag{5.9}$$

$$c = \frac{P \tau_d^{-1}}{\tau_{\text{wall},2}^{-1} + \tau_d^{-1}} = (1610 \pm 1_{\text{stat.}} \pm 75_{\text{syst.}})\,\text{s}^{-1} \tag{5.10}$$

The total UCN counts for 1 μA beam current and 60 s irradiation time over the course of the experimental run is shown in Fig. 5.13. The source volume is connected to a long

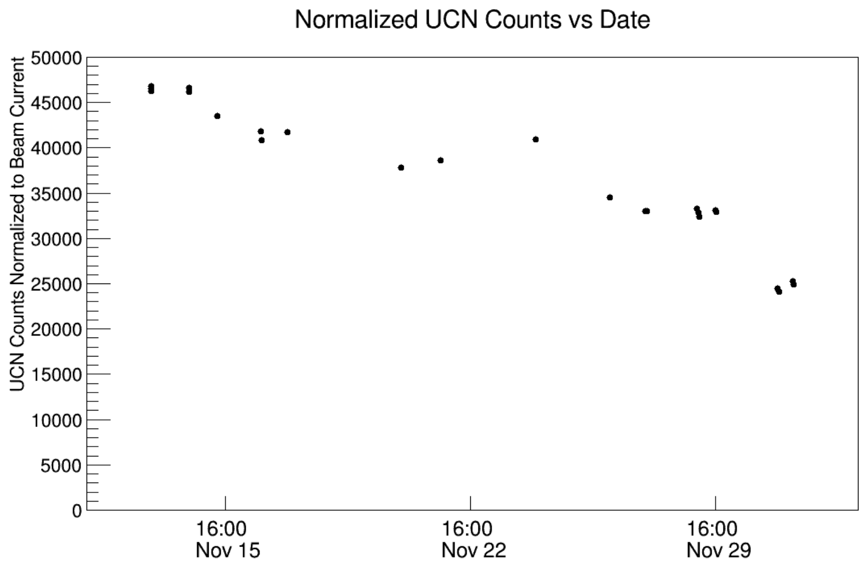

Figure 5.13: The total UCN counts extracted from the source for 1 μA beam current and 60 s irradiation time at different days during the experimental run.

UCN guide sealed with an O-ring. It is expected that the rest gas to contaminate the source every time the UCN valve is opened. This caused a reduction in the UCN yield over the course of the measurement as shown in Fig. 5.13. In addition, the changes in the UCN guide geometry in the latter half of the run pottentially affected this drop.

5.3 Storage Lifetime: Measurements And Simulations

The total number of detected UCN strongly depends on the storage lifetime of the source τ_1 (See Eqn. 5.4) which indicates the performance of the UCN source. The storage lifetime of UCN is determined by measuring the detected UCN at different valve open delay times right after the irradiation stops. The typical chosen values are 0 s, 5 s, 10 s, 20 s, 30 s, 60 s, 80 s, 120 s and 170 s. The exponential decay constant in the fit function to the total UCN counts for different valve open delay times is the total storage lifetime in the source.

Fig. ?? shows the total UCN counts versus the valve open delay time for 1 μA proton beam current and 60 s irradiation time. The longer delay times give rise to lower UCN counts due to the loss mechanisms. The one exponential fit function

$$\text{UCN counts} = Ae^{-t/\tau_1} \tag{5.11}$$

determines the storage lifetime τ_1. At 170 s valve open delay time, the total UCN counts are not consistent with what the fit function predicts. However, the result of the fit is not driven by this inconsistency as it has a negligible effect on the extrected storage lifetime.

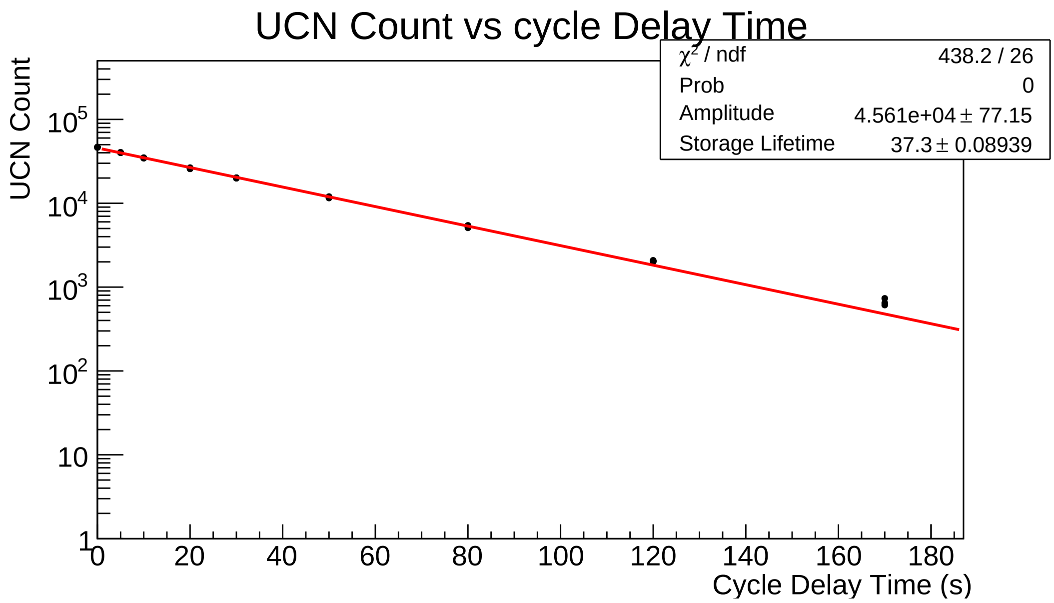

Figure 5.14: The total UCN counts at different valve open delay times for 1 μA beam current and 60 s irradiation time. The red line is the one exponential fit.

The storage lifetime of the UCN source is measured at different proton beam currents and different irradiation times for better optimization. The result of those measurements is shown in Fig. 5.15. The UCN production rate increases at higher proton beam current. However, this creates a higher heat load on the UCN source which leads to higher up-scattering rate. The higher proton beam currents and longer irradiation times give rise to lower storage lifetimes.

PENTrack Simulations

For better understanding of the loss mechanisms, the experiment was also simulated in PENTrack [137]. PENTrack is a particle tracking simulation software which simulates the trajectories of UCN and their decay products (e.g. Protons and Electrons) and their spin precession in complex geometries in Electric and Magnetic fields by solving the relativistic equation of motion. As discussed in Chapter 1, UCN interacts with all four fundamental forces. To describe the interaction of UCN with matter, a complex optical potential is used to describe matters [?]:

$$U = V - iW \tag{5.12}$$

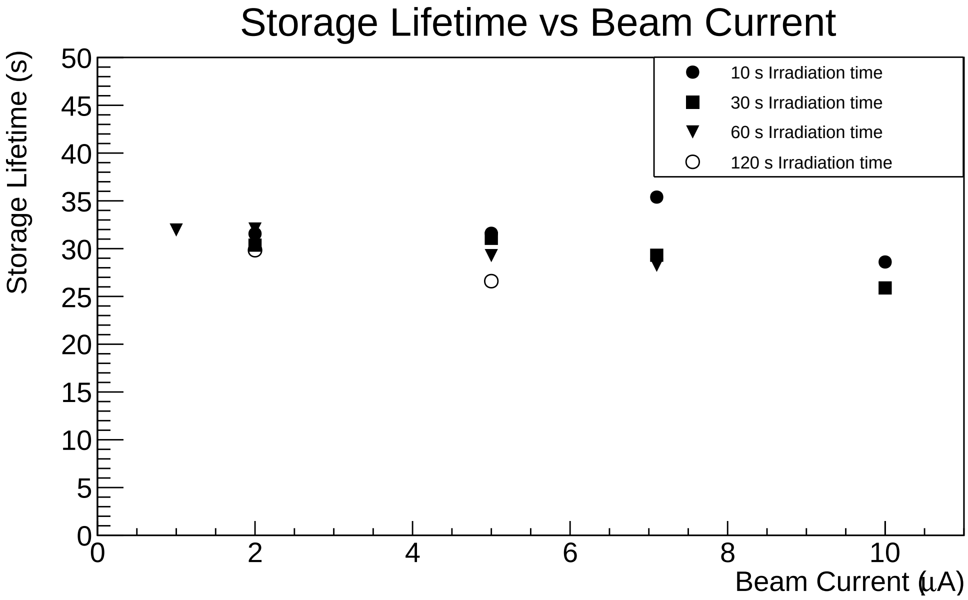

Figure 5.15: Storage lifetime in the source at different irradiation times and proton beam currents. Different markers refer to different target irradiation times. At longer irradiation times and higher beam currents the storge lifetime decreases due to the increase heat load in the cryostat and increase in the superfluid helium temperature.

Material	Fermi pot. (neV)	Diffusivity
He-II ($\tau_{\mathrm{He}} = 390\,\mathrm{s}$)	$18.8 - 8.44 \cdot 10^{-10}i$	0.16
Prod. volume (NiP)	$213 - 0.100i$	0.05
Guides (stainl. steel)	$183 - 0.120i$	0.03
Foil (aluminium)	$54.1 - 0.00281i$	0.20
GS30 scintillator	$83.1 - 0.000123i$	0.16
GS20 scintillator	$103 - 1.24i$	0.16

Table 5.2: Material parameters used in the PENTrack simulation. [14–16]

where the real part, V, depends on the number densities and bound coherent scattering lenghtes of each nucleus species. The imaginary part, W, depends on the loss cross-section for a given velocity. Upon the incidence of the UCN on a surface, it can be scatterd either specularly or diffusely. PENTrack uses two models to calculate the scattering distribution of the UCN impinging on the material surface: Lambert model or the Microroughness [138].

Experimental geometries imported in PENTrack are the StL files made through CAD models. For these simulations, the exact model of the vertical UCN source was used including the burst disk, the actual shape of the UCN valve in the open and close state, pinhole foil and the detector.

The abosorption in the foil is set according to the measurements in [14]. The main decetor is modeled with its two scintillator layes [94] and their corresponding Fermi potentials and absorption cross section, as stated in [15];

In the simulations, it is assumed that the spectrum of produced UCN is proportional to $\sqrt{E}$. The wall loss parameters were tuned to give a storge lifetime of $\tau_1 = 34.9 \pm .8$ s with an upscattering lifetime in the superfluid of $\tau_{\mathrm{He}}^{-1} = (390\text{ s})^{-1} = 0.008\text{ s}^{-1} \cdot 0.85^7$, resulting in material parameters shown in Table 5.2.

The simulation and the measurement data are both fitted with the fucntion

$$R(t) = R_0 \left[1 - \exp\left(-\frac{t-\Delta t}{\tau_{\rm rise}}\right)\right] \exp\left(-\frac{t-\Delta t}{\tau_2}\right) + R_B. \tag{5.13}$$

after opening the valve at $t = 0$. In this equation, Δt is the delay time between opening the valve and detecting the first UCN and it is 2 to 3 s. The parameter R_B is the background UCN rate in the experimental data and is zero in simulations. The Lambert model is used to tune the probablity of UCN being diffusely reflected on the guide walls to match the rise time $\tau_{mathrmrise}$ and fall time τ_2 of the UCN rate in the storage lifetime measurements (See Fig. 5.16 and 5.17). The experimental data is best described by the diffusivity of 3 % and 5 %. The

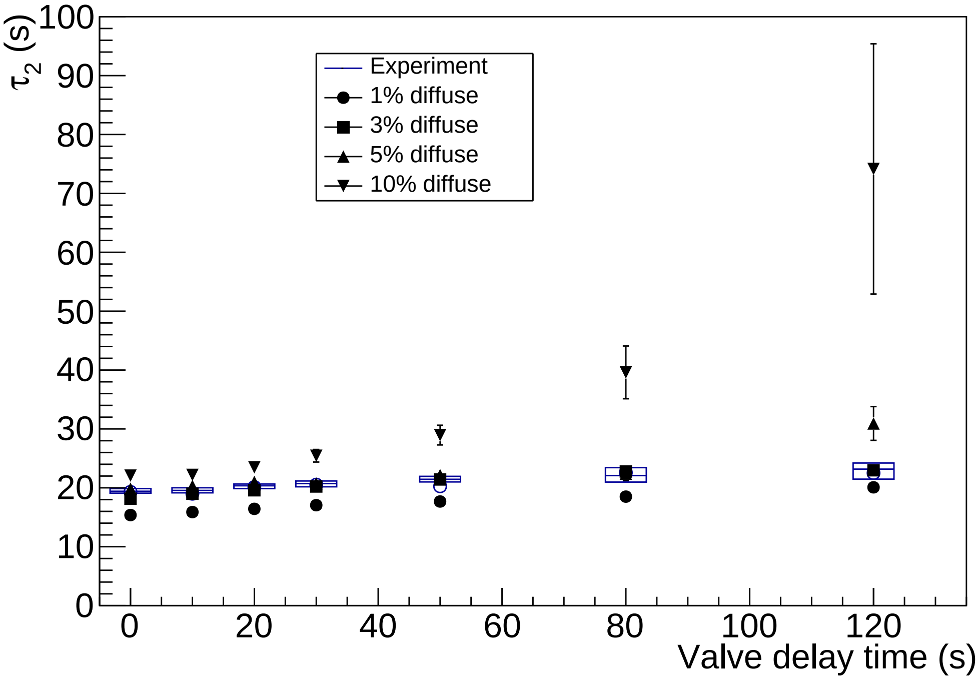

Figure 5.16: Comparison of fall time τ_2 in the experimental data and the simulations with different diffuse-reflection probabilities. The boxes indicate the second and third quartile of the experimental data.

The simulations are also used to determine the parameter $f_{\rm He}$ or the fraction of time that UCN spends in the superfluid helium in the detectable range of 120 neV to 200 neV. For the steady-state measurements, this fraction turned out to be almost constant over a range of upscattering lifetime in the superfluid giving

$$f_{\rm He,3} = 0.464 \pm 0.001_{\rm stat.} \pm 0.003_{\rm syst.}, \tag{5.14}$$

where the systematic uncertainty is the variation in simulations with $\tau_{\rm He}$ from 3.05 s to 390 s. The Eqn. 5.5 could be rewritten as

$$\tau_d^{-1} + \tau_{\rm wall,2}^{-1} = \tau_2^{-1}(T_0) - f_{\rm He,2} B\,(T_0)^a \tag{5.15}$$

where the value for τ_2 is

$$\tau_2^{-1}(T_0) = (19.3 \pm 0.8_{\rm stat.})\ \text{s} \tag{5.16}$$

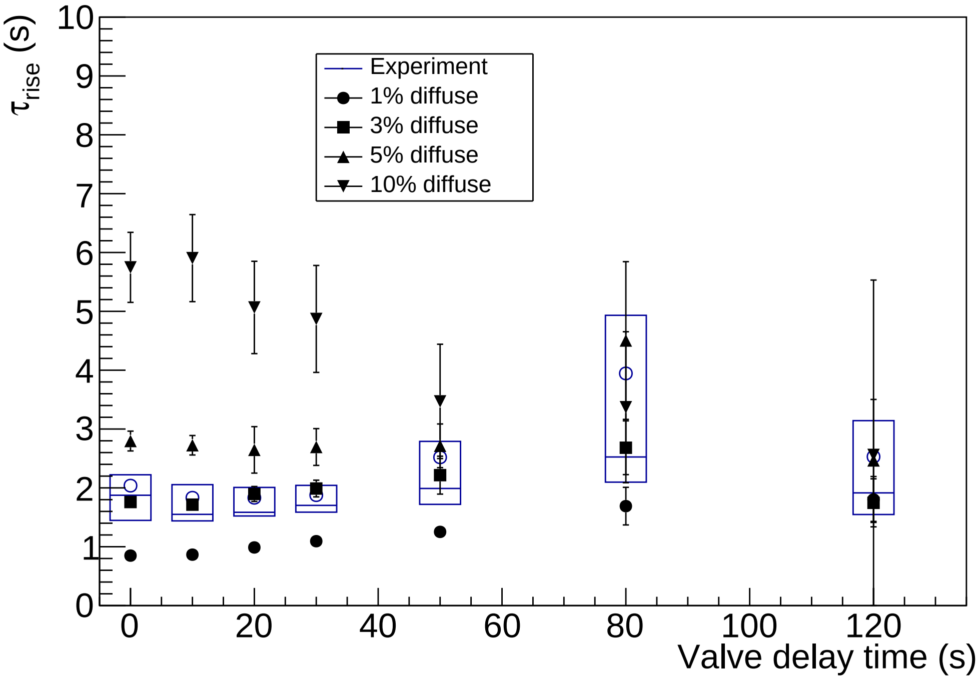

Figure 5.17: Comparison of rise time τ_{rise} in experimental data and simulations with different diffuse-reflection probabilities. The boxes indicate the second and third quartile of the experimental data.

comes from fall time in the storage lifetime measurements at the temperature T_0 which is

$$T_0 = 0.92 \pm 0.005_{\text{stat.}} \pm 0.05_{\text{syst.}}. \tag{5.17}$$

Replacing Eqn. 5.15 in Eqn. 5.9, B can be written as

$$B = \frac{b\tau_2^{-1}(T_0)}{f_{\text{He},3} + f_{\text{He},2}b\left(\frac{T_0}{1\,\text{K}}\right)^a}. \tag{5.18}$$

Here all the parameters are known except for $f_{\text{He},2}$ which does not significantly affect the result, and hence, it is assumed to lie between 0 and 1. As a result

$$B = (10.4 \pm 0.4_{\text{stat.}} \pm 4.1_{\text{syst.}}) \cdot 10^{-3}\,\text{s}^{-1}. \tag{5.19}$$

which is consistent with the result in [73].

5.4 Heater Tests of The Source

The cooling process of the spallation neutrons create a heat input on the cryostat including the superfluid helium. This heat input must be removed to keep the temperature of the superfluid helium constant. This is critical because the storage lifetime of neutrons depend strongly to the temperature of the superfluid helium.

The heat load on the cryostat creates a temperature gradient along the heat exchanger to the suprefluid helium bottle. The temperature gradient in the superfluid helium is described by its heat conductivity. The bigger the temperature difference, the lower the heat conductivity. The temperature dependence of the heat conductivity in the superfluid helium is describe by theorical models from the lambda point 2.17 K down to around 1.4 K which is above the temperature for the UCN production (< 1 K). Because of the difficulty to reach such low temperatures, the mechanism of heat transfer in that temperature region is not fully understood. To check the validity of theoretical models, the extrapolation to lower temperatures is compared to acquired data.

In order to create excess heat load on the superfluid helium, there are heater tapes wrapped around the superfluid helium bottle. These heaters can create a temperature gradient between the heat exchanger and the superfluid helium bottle (See Sec. 4.4). This temperature gradient can be measured using the temperature sensors shown in Fig. 5.8.

The heater test procedure is the following. The heater tape around the superfluid helium bottle is turned on when the temperature of the superfluid helium is stable. This is called the *base* temperature. The applied heat load could easily be calculated since the applied current and voltage are known. After the heater is turned on, the temperature of the superfluid helium starts to increase. This causes an increase in the flow rate in the ^{3}He pot. After some time, the temperature of the superfluid starts to settle and reach a new equilibrium. This temperature is referred to as the *saturation* temperature. At this point, the heater could be turned off which causes the superfluid temperature and the flow rate of the ^{3}He to go back to the base conditions.

In 2017 two sets of heater tests were performed on the vertical UCN source: The April heat test and the November heat test. In April the base temperature of the superfluid helium was slightly higher than in November. In addition, there was no proton beam during the April cooling and it was purely a cryostat cooling test. Table. 5.3 shows the heat load and the temperatures of those tests.

Theoretical Models

The relationship between the heat flux and the temperature gradient in a one dimentional channel is written as following

$$q^m = f^{-1}\left(T, p\right)\frac{dT}{dx} \tag{5.20}$$

Where q is the input heat flux, T is the temperature, p is the pressure and $\frac{dT}{dx}$ is the temperature gradient along the channel and $f\left(T, p\right)$ is the heat conductivity fucntion which controls the temperature gradient of the heat flux and could be written as

$$f\left(T, p\right) = \frac{A_{\mathrm{GM}}\rho_n}{\rho_s^3 s^4 T^3} \tag{5.21}$$

where ρ_n is the density of the normal fluid component, ρ_s is the density of the superfluid component, s is the specific entropy, T is the temperature and A_{GM} is the Gorter-Mellink parameters which describes the friction between the normal fluid component and the superfluid component.

Since the Gorter-Mellink parameter is not known, he calculation of $f\left(T, p\right)$ in the form of Eq. 5.21 is difficult because. However, there are other models to describe the behaviour of the heat conductivity functions. There are two models that are considered here at the saturated vapour pressure. As a result, the pressure dependence could be neglected. The models are the theory model from Van Sciver [139] and the HEPAK model [140]. Fig. 5.18

Heater Power (mW)	$T_{base,TS10}$ (K)	$T_{sat.,TS10}$ (K)	$T_{base,TS11}$ (K)	$T_{sat.,TS11}$ (K)	$T_{base,TS12}$ (K)	$T_{sat.,TS12}$ (K)	$T_{base,TS14}$ (K)	$T_{sat.,TS14}$ (K)	$T_{base,TS16}$ (K)	$T_{sat.,TS16}$ (K)
April Heat Test										
2.5	0.717	0.718	0.93	0.931	0.926	0.9271	0.93	0.931	1.012	1.013
12.5	0.717	0.7185	0.93	0.9315	0.924	0.929	0.93	0.9315	1.011	1.015
25	0.719	0.723	0.928	0.931	0.919	0.929	0.928	0.931	1.008	1.015
75	0.7195	0.7255	0.9285	0.937	0.922	0.952	0.928	0.937	1.01	1.03
250	0.7175	0.7375	0.93	0.9475	0.93	1	0.93	0.947	1.01	1.065
November Heat Test										
25	0.724	0.73	0.892	0.9	0.84	0.86	0.92	0.923	0.96	0.97
50	0.741	0.75	0.895	0.91	0.84	0.9	0.92	0.93	0.96	0.99
75	0.73	0.74	0.9	0.91	0.85	0.92	0.92	0.93	0.96	1
100	0.73	0.769	0.9	0.936	0.85	0.96	0.92	0.952	0.96	1.04
150	0.73	0.755	0.9	0.93	0.84	0.99	0.92	0.945	0.96	1.06
200	0.73	0.9	0.9	1.26	0.84	1.23	0.92	1.25	0.96	1.26
250	0.73	0.94	0.895	1.385	0.84	1.345	0.92	1.363	0.97	1.375

Table 5.3: The heater power and the base and saturation temperature of the temperature sensors in the superfluid helium and in the ^{3}He pot for the April and November heat tests. [13]

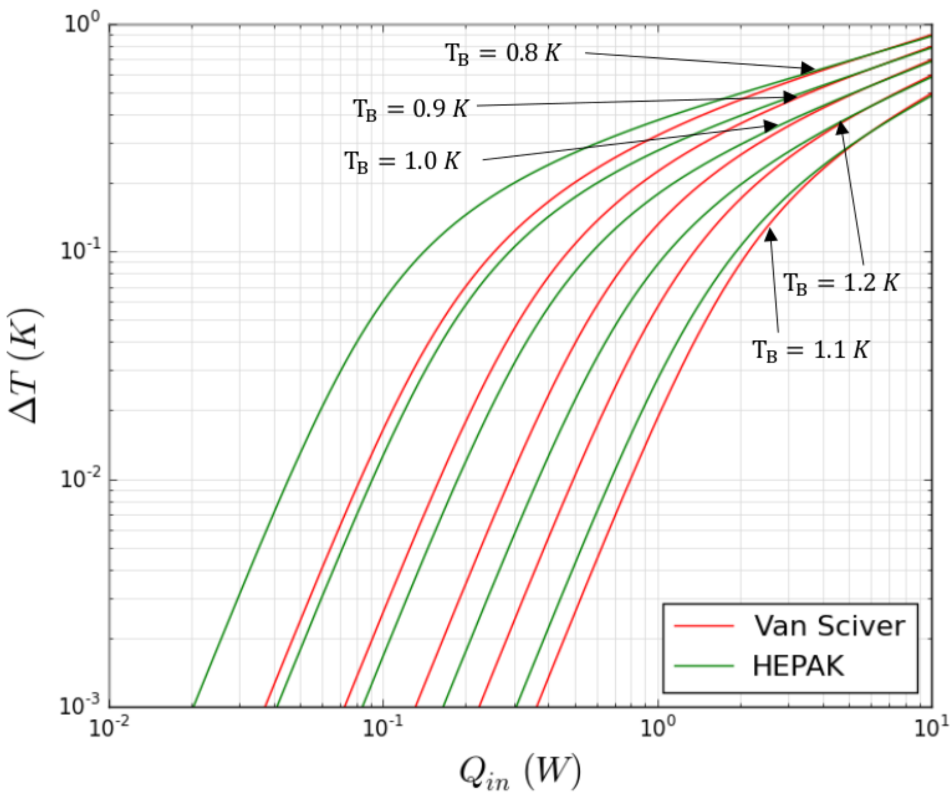

Figure 5.18: The heat conductivity function of the Van Sciver and HEPAK models. The vertical axis shows the temperature gradiant along the channel and the horizonal axis shows the input heat flux [13]. The arrows on the graph indicate the temperature of the superfluid helium

As Fig. 5.18 shows, at higher heat input both models tend to agree. However, at lower heat inputs, the heat conductivity function values for the Van Sciver model lie below the values for the HEPAK model. In addition, as the temperature of the superfluid helium increases, the heat conductivity function tends to look more linear. Since the Van Sciver model is more well known, it is used for comparision with experimental data.

Measurement Result

The data shown in Table. 5.3 is a set of cleaned data from all the heat tests in 2017. If the heat load on the cryostat is higher than its cooling power, the temperature of the superfluid helium would increase linearly without reaching an equilibrium. This phenomena has been observed for higher heater powers e.g. 1 W. As a result, that data is discarded.

Fig. 5.19 shows the result of the April heat test. For a given heat input, the temperature difference between the base and the saturation temperature for each temperature sensor is calculated (See table 5.3). The average of all of those temperature differences give the overall ΔT across the channel. Those are shown with black dots in Fig. 5.19 as the raw data. However, the heat input for each data point should be corrected since the total heat input is a combination of the added heat from the heater tapes and the background heat load on the cryostat which is not taken into account.

The two other sources of heat input to be considered are the Joule-Thomson expansion

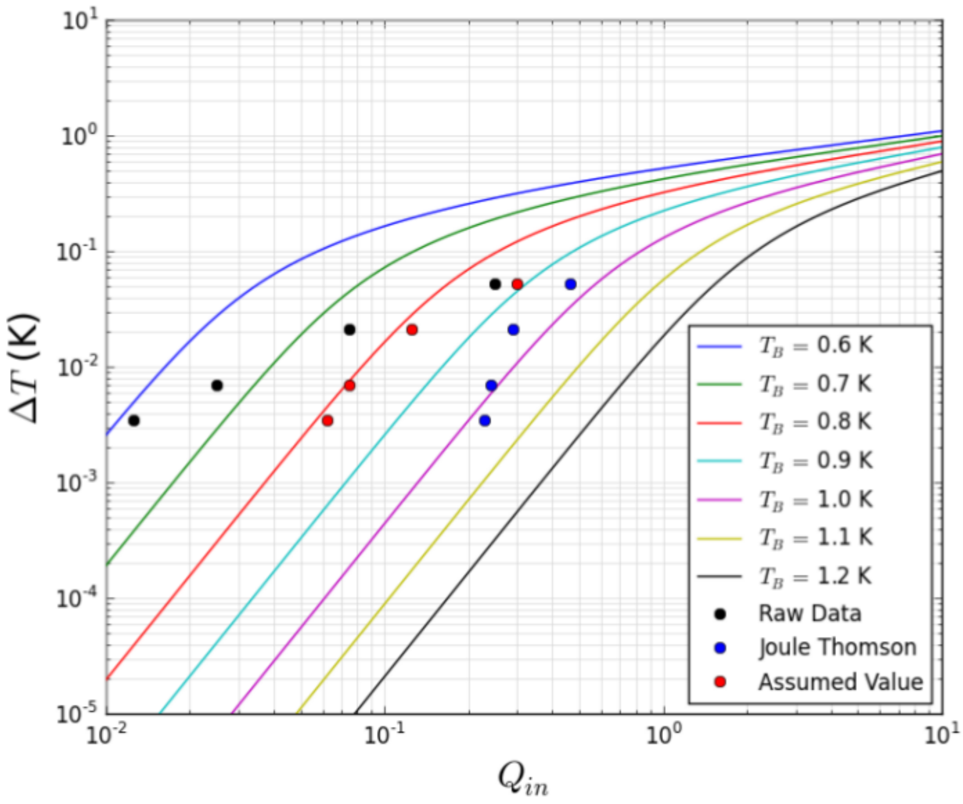

Figure 5.19: The comparison between the April heat test data and the Van Sciver model. The lines show the Van Sciver model's heat conductivity function at different superfluid helium bath temperatures. The black data points show the measured raw data of the heat tests. The blue points are the Joule Thomson values, which are the raw data plus the calculated background heat (included Joule-Thomson effect) and the red points show the raw data with the assumed 50 mW background heat input.

and the the background heat load to the ^{3}He pot due to the thermal readiation and to the superfluid helium bottle. The Joule-Thomson expansion happens when a gas or liquid passes through a valve which has different temperature and pressures on both sides while there is no heat exchange to the environment. Here ^{3}He flows into the heat exchanger and passes through a valve with different pressures and temperatures on two sides. Because of the Joule-Thomson expansion some liquid changes into vapor which is then directly pumped out of the system and does not contribute to the cooling process. For the backround heat load, based on estimations of the sources of the background heat to the bottle alone, combined with the measurements of the mass flow of ^{4}He from the top of the bottle when the ^{3}He system is switched off, a heat of $\simeq$ 50 mW is a reasonable estimate of the true background heat to the bottle alone. In Fig. 5.19, the assumed values are the sum of the 50 mW background heat and the heat input from the heaters and the Joule-Thomson values are the sum of the heat input from the heaters plus the calculated 232 mW calculated background heat [13].

Fig. 5.20 shows the data with the heaters in November as well as the theoretical model of Van Sciver for the heat conductivity. Each color represents a temperature range. The markers are the actual data taken in November 2017.

At all the temperture ranges, the acquired data shows lower heat load compared to the theoretical model. At the range of 1.2-1.3 K, the data point with the smaller ΔT is acquired at a higher He-II base temperature, whereas the data point with higher ΔT is acquired at standard He-II base temperature. The data points which are closer to the theoretical models are acquired at lower base temperature for the superfluid helium. Since the measured data show bigger temperature differences compared to the theoretical model of Van Sciver, it suggests that the theory is assuming higher heat conductivity. Looking back at Fig. 5.18, it shows that using the HEPAK model might solve this problem since the HEPAK model shows lower heat conductivity.

One reason between the disagreement between the measurements and theory could be the fact that these theoretical models are only measured down to 1.4 K and they are extrapolated to lower temperatures. Another reason could lie in the geometry difference. The theoretical models are valid for a one-dimensional channel while there is a 90° bend in the experimental setup (See Fig. **??**) which can cause a higher temperature differnece across the channel. One other reason might be the uncertainty in the measured temperature due to the calibration of the temperature sesnors. There might be other unknown sources of systematic error affecting the measurements.

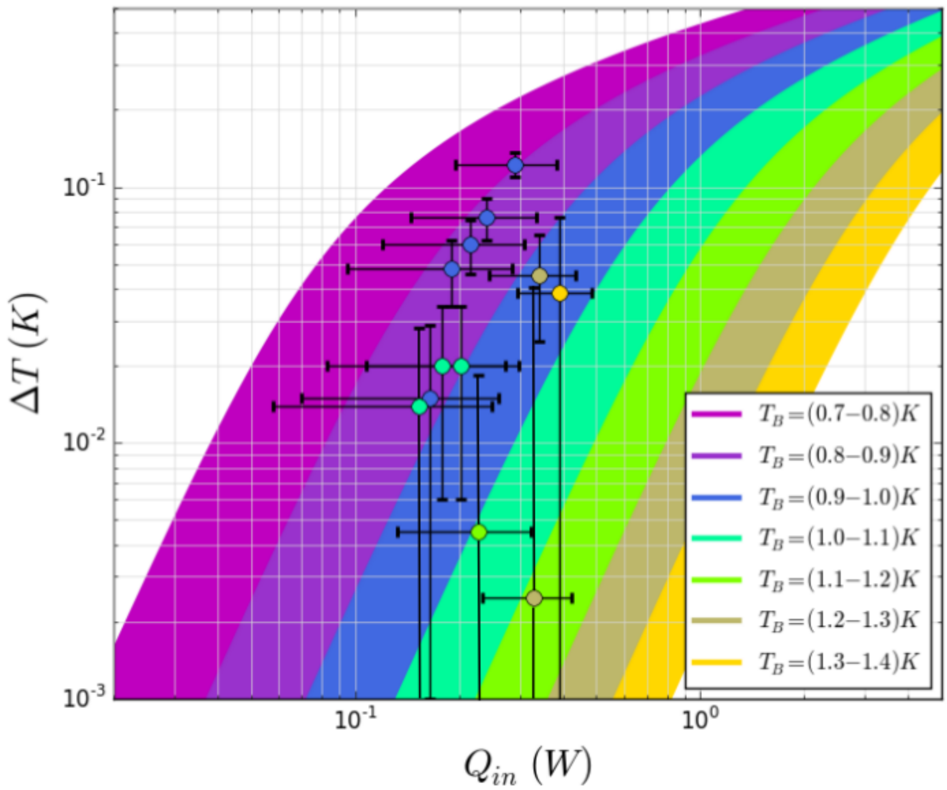

Figure 5.20: Theoretical model of Van Sciver for the heat conductivity at different temperature ranges and the November data. The vertical axis shows the temperature difference between the base and the saturation temperature for temperature sensors. The horizontal axis shows the heat input from the heaters plus the background heat.

5.4.1 Heater Test Versus Proton Beam Current

One of the UCN experiments was designed to match the heater power from the heaters with the proton beam current. The measurement procedure is to measure the steady-state UCN yield at different proton beam current and match the temperature difference in the superfluid helium with the heater tests measurements described above. However, the result of this experiment did not look as expected. One main reason was that some UCN runs were conducted during the autofil of the 4 K ^{4}He reservoir. This process causes an increase in the ^{3}He flow rate due to an increased heat load. As a result, the superfluid helium temperature could not steadily increase and it affected the UCN yield. Such measurement requires a stable cryostat which could not be achieved (See Ref. [141]). Another reason was that the irradiation time was not long enough so that the superfluid helium temperature or the ^{3}He pot flow rate could reach an equilibrium. Proton beam trips was also an additional reason for the unstable UCN rate.

5.5 Detector Comparison

Using the rotary valve

5.6 Background Measurements

With Ni foil

5.7 UCN guide Transmission Measurements

5.8 Result And Conclusion

Chapter 6

Conclusion

Appendices

Appendix A

Derivation of Ramsey's Method

MUST BE EDITED In this section, we'll review the Ramsey technique for molecular beam resonance experiments. In all previous studies the oscillating fields were extended approximately uniformly throughout the regions in which the energy levels of the system were investigated. This was not efficient since the amplitude and phase of the oscillating field might change along the path of the beam. As a different approach, Ramsey suggested to confine the oscillating fields to small regions; one at the beginning of the space which the energy levels are being studied and the other one at the end. In this case, there is no oscillating field in between.

Consider a system which at time t_1 is subjected to an oscillatory perturbation which induces transition between eigenstates p and q:

$$V = \begin{pmatrix} 0 & \hbar b e^{i\omega t} \\ \hbar b e^{-i\omega t} & 0 \end{pmatrix} \tag{A.1}$$

An example of such perturbation is a system with a magnetic moment entering a region with rotating magnetic field with angular velocity ω. The general wave function for this system is :

$$\psi(t) = C_p(t)\psi_p + C_q(t)\psi_q \tag{A.2}$$

Therefore, the time dependent Schrödinger equations will have the form :

$$\begin{cases} i\hbar \dot{C}_p(t) & = W_p C_p(t) + \hbar b e^{i\omega t} C_q(t) \\ i\hbar \dot{C}_q(t) & = \hbar b e^{-i\omega t} C_p(t) + W_q C_q(t) \end{cases} \tag{A.3}$$

Let's write the above equation in matrix notation and solve for $C_p(t)$ and $C_q(t)$. Let's define

$$C = \begin{pmatrix} C_p \\ C_q \end{pmatrix} \tag{A.4}$$

Hence, we would get,

$$i\hbar \frac{d}{dt} \begin{pmatrix} C_p \\ C_q \end{pmatrix} = \begin{pmatrix} W_p & \hbar b e^{i\omega t} \\ \hbar b e^{-i\omega t} & W_q \end{pmatrix} \begin{pmatrix} C_p \\ C_q \end{pmatrix} \tag{A.5}$$

We assume that, at $t = t_1$, C_p and C_q have the values $C_p(t_1)$ and $C_q(t_1)$ respectively. We are interested in the solution of the above equation at $t = t_1 + T$. The matrix on the right side can be written as

$$\begin{pmatrix} W_p & \hbar b e^{i\omega t} \\ \hbar b e^{-i\omega t} & W_q \end{pmatrix} = \begin{pmatrix} W_p & \hbar b \cos\omega t + i\hbar b \sin\omega t \\ \hbar b \cos\omega t - i\hbar b \sin\omega t & W_q \end{pmatrix} \tag{A.6}$$

$$= \begin{pmatrix} W_p & 0 \\ 0 & W_q \end{pmatrix} - \hbar b \sin\omega t \sigma_2 + \hbar b \cos\omega t \sigma_1 \tag{A.7}$$

Where σ_1 and σ_2 are Pauli matrices. Hence, The time dependent Schrödinger equation will take the form

$$\frac{d}{dt}\begin{pmatrix} C_p \\ C_q \end{pmatrix} = -i\left[\begin{pmatrix} \frac{W_p}{\hbar} & 0 \\ 0 & \frac{W_q}{\hbar} \end{pmatrix} + b\sigma_1 \cos\omega t - b\sigma_2 \sin\omega t\right]\begin{pmatrix} C_p \\ C_q \end{pmatrix} \tag{A.8}$$

But, we can rewrite the first matrix on the right side as

$$\begin{pmatrix} \frac{W_p}{\hbar} & 0 \\ 0 & \frac{W_q}{\hbar} \end{pmatrix} = \begin{pmatrix} \frac{W_p+W_q}{2\hbar} + \frac{W_p-W_q}{2\hbar} & 0 \\ 0 & \frac{W_p+W_q}{2\hbar} - \frac{W_p-W_q}{2\hbar} \end{pmatrix} \tag{A.9}$$

Let's define

$$C = \begin{pmatrix} C_p \\ C_q \end{pmatrix}, \Omega = \frac{W_p + W_q}{2\hbar}, \omega_0 = \frac{W_q - W_p}{\hbar} \tag{A.10}$$

Therefore the Schrödinger equation takes the form

$$\frac{d}{dt}C = -i\left[\Omega - \frac{\omega_0}{2}\sigma_3 + b\left(\sigma_1 \cos\omega t - \sigma_2 \sin\omega t\right)\right]\begin{pmatrix} C_p \\ C_q \end{pmatrix} \tag{A.11}$$

The term $(\sigma_1 \cos\omega t - \sigma_2 \sin\omega t)$ is like a rotation. In general, we have

$$e^{-i\vec{\sigma}\cdot\hat{n}\frac{\theta}{2}}\vec{a}.\vec{\sigma}e^{i\vec{\sigma}.\hat{n}\frac{\theta}{2}} = \left[\hat{n}(\hat{n}.\vec{a}) + \cos\theta(\vec{a} - \hat{n}(\hat{n}.\vec{a})) + \sin\theta(\hat{n}\times\vec{a})\right]\vec{\sigma}. \tag{A.12}$$

If we consider $\hat{n} = -\hat{k}$ and $\vec{a} = \hat{x}$, then we would get

$$\sigma_1 \cos\omega t - \sigma_2 \sin\omega t = e^{i\frac{\omega t}{2}\sigma_3}\sigma_1 e^{-i\frac{\omega t}{2}\sigma_3}. \tag{A.13}$$

Hence, the Schrödinger equation will take the form

$$\dot{C} = -ie^{i\frac{\omega t}{2}\sigma_3}\left[\Omega - \frac{\omega_0}{2}\sigma_3 + b\sigma_1\right]e^{-i\frac{\omega t}{2}\sigma_3}C. \tag{A.14}$$

Let's define D as

$$C = e^{i\frac{\omega t}{2}\sigma_3}e^{-i\Omega t}D \tag{A.15}$$

Now, we rewrite the Schrödinger equation in terms of variable D

$$\dot{D} = -i\left[\left(\frac{\omega - \omega_0}{2}\right)\sigma_3 + b\sigma_1\right]D, \tag{A.16}$$

and by defining $a := \left[(\omega_0 - \omega)^2 + (2b)^2\right]^{\frac{1}{2}}$, $\cos\theta = \frac{\omega_0-\omega}{a}$ and $\sin\theta = \frac{2b}{a}$, we get

$$\dot{D} = \frac{ia}{2}\left[\sigma_3 \cos\theta - \sigma_1 \sin\theta\right]D. \tag{A.17}$$

Hence, the solution of the above equation has the form

$$D(t_1 + T) = e^{\left[\frac{ia}{2}(\sigma_3 \cos\theta - \sigma_1 \sin\theta)T\right]}D(t_1). \tag{A.18}$$

If we use $e^{i\vec{\sigma}\cdot\hat{n}\frac{\phi}{2}} = I\cos\frac{\phi}{2} + i(\vec{\sigma}\cdot\hat{n})\sin\frac{\phi}{2}$ with $\phi = aT$ and $\vec{\sigma}\cdot\hat{n} = \sigma_3\cos\theta - \sigma_1\sin\theta$, then

$$D(t_1+T) = \left[\cos\frac{aT}{2} + i(\sigma_3\cos\theta - \sigma_1\sin\theta)\sin\frac{aT}{2}\right] D(t_1) \tag{A.19}$$

and therefore $C(t_1+T)$ would be

$$C(t_1+T) = e^{i\frac{\omega}{2}(t_1+T)\sigma_3} e^{-i\Omega T}\left[\cos\frac{aT}{2} + i(\sigma_3\cos\theta - \sigma_1\sin\theta)\sin\frac{aT}{2}\right] e^{-i\frac{\omega t_1}{2}\sigma_3} C(t_1), \tag{A.20}$$

or equivalently

$$\begin{cases} C_p(t_1+T) = \left\{\left[i\cos\theta\sin\frac{aT}{2} + \cos\frac{aT}{2}\right] C_p(t_1) - \left[i\sin\theta\sin\frac{aT}{2}e^{i\omega t_1}\right] C_q(t_1)\right\} \times \\ \qquad e^{\left\{i\left[\frac{1}{2}\omega - \frac{(W_p+W_q)}{2\hbar}\right]T\right\}} \\ C_q(t_1+T) = \left\{-\left[i\sin\theta\sin\frac{aT}{2}e^{-i\omega t_1}\right] C_p(t_1) + \left[-i\cos\theta\sin\frac{aT}{2} + \cos\frac{aT}{2}\right] C_q(t_1)\right\} \times \\ \qquad e^{\left\{i\left[-\frac{\omega}{2} - \frac{W_p+W_q}{2\hbar}\right]T\right\}} \end{cases} . \tag{A.21}$$

These are the general solutions for a system with energy eigenstates p and q. As a comparison, if we put $C_p(t_1+T) = a(t)$, $C_q(t_1+T) = b(t)$, $a = \omega'$, $2b = \omega_1$ then we would get equation (1.31). In this case, W_p and W_q are energies of the spin up and spin down configurations.

As a special case, if b=0 (no perturbation), then $\cos\theta = 1$ and $\sin\theta = 0$. Hence, the solutions would be

$$\begin{cases} C_p(t_1+T) = e^{-i\frac{W_p}{\hbar}T} C_p(t_1) \\ C_q(t_1+T) = e^{-i\frac{W_q}{\hbar}T} C_q(t_1) \end{cases} . \tag{A.22}$$

Now, consider a system which is subjected to perturbation for time τ and length l, then the perturbation goes off for time T and length L and again the perturbation goes on for another time τ. To achieve greater generality, corresponding to the experimental impossibility of attaining completely uniform magnetic fields, we assume that energy levels p and q are not constant in the intermediate state when b=0, which means it is divided to sub-regions with duration Δt_k and energies are $W_{p,k}$ and $W_{q,k}$ respectively. We assume

$$C_p(0) = 1,\ C_q(0) = 0, \tag{A.23}$$

which means the system is at state p before it enters the first perturbation region. Hence, the amplitudes would be

$$\begin{cases} C_p(\tau) = \left[i\cos\theta\sin\frac{a\tau}{2} + \cos\frac{a\tau}{2}\right] e^{i\left[\frac{\omega}{2} - \left(\frac{W_p+W_q}{2\hbar}\right)\right]\tau} \\ C_q(\tau) = \left[-i\sin\theta\sin\frac{a\tau}{2}\right] e^{i\left[-\frac{\omega}{2} - \left(\frac{W_p+W_q}{2\hbar}\right)\right]\tau} \end{cases} . \tag{A.24}$$

After entering the intermediate region we would get

$$\begin{aligned} C_p(\tau+T) &= \Pi_k e^{-iW_{p,k}\Delta\frac{t_k}{\hbar}} C_p(\tau) \\ &= e^{-\frac{i}{\hbar}\Sigma_k W_{p,k}\Delta t_k} C_p(\tau) \\ C_p(\tau+T) &= e^{-i\frac{\bar{W}_p T}{\hbar}} C_p(\tau) \end{aligned} \tag{A.25}$$

$$C_q(\tau+T) = e^{-i\frac{\bar{W}_q T}{\hbar}} C_q(\tau). \tag{A.26}$$

It is impossible to have completely uniform magnetic fields in the experiment. Hence, we assume that the energies of the p and q states are not constant in this region, and the region is divided into a number of sub-regions such that in the k^{th} sub-region of duration Δt_k the energies are $W_{p,k}$ and $W_{q,k}$.

Here we have, $\bar{W}_p = \frac{1}{T}\Sigma_k W_{p,k}\Delta t_k = \frac{1}{L}\Sigma_k W_{p,k}\Delta L_k$, which is the space mean value of W_p. There is a similar interpretation for $\bar{W}_q$ as well. After entering the final perturbation region,

$$\begin{cases} C_p(2\tau+T) = \left\{\left[i\cos\theta\sin\frac{a\tau}{2}+\cos\frac{a\tau}{2}\right]C_p(\tau+T) - \left[i\sin\theta\sin\frac{a\tau}{2}e^{i\omega(\tau+T)}\right]C_q(\tau+T)\right\}\times \\ \qquad e^{i\left[\frac{\omega}{2}-\frac{(W_p+W_q)}{2\hbar}\right]\tau} \\ C_q(2\tau+T) = \left\{-\left[i\sin\theta\sin\frac{a\tau}{2}e^{-i\omega(\tau+T)}\right]C_p(\tau+T) + \left[-i\cos\theta\sin\frac{a\tau}{2}+\cos\frac{a\tau}{2}\right]C_q(\tau+T)\right\}\times \\ \qquad e^{i\left[\frac{-\omega}{2}-\frac{(W_p+W_q)}{2\hbar}\right]\tau} \end{cases} \tag{A.27}$$

We can rewrite the above equation as

$$\begin{aligned} C_q(2\tau+T) = 2i\sin\theta&\left[\cos\theta\sin^2\frac{a\tau}{2}\sin\frac{\lambda T}{2} - \frac{1}{2}\sin a\tau\cos\frac{\lambda T}{2}\right] \\ &\times e^{-i\left[\frac{\omega}{2}+\frac{(W_p+W_q)}{2\hbar}\right]}(2\tau+T) + \left[\frac{\bar{W}_p - W_p + \bar{W}_q - W_q}{2\hbar}T\right], \end{aligned} \tag{A.28}$$

where

$$\lambda = \left(\frac{\bar{W}_q - \bar{W}_p}{\hbar}\right) - \omega. \tag{A.29}$$

Therefore, the probability that the system changes from state p to state q is

$$P_{p,q} = |C_q|^2 = 4\sin^2\theta\sin^2\frac{a\tau}{2}\left[\cos\frac{\lambda T}{2}\cos\frac{a\tau}{2} - \cos\theta\sin\frac{\lambda T}{2}\sin\frac{a\tau}{2}\right]^2. \tag{A.30}$$

We can define a dimensionless parameter

$$x := \frac{\omega_0-\omega}{2b}, \tag{A.31}$$

and therefore, a would take the form

$$a = 2b\sqrt{1+x^2}. \tag{A.32}$$

If we set $b\tau = \frac{\pi}{4}$ (which is similar to the previous section which $\omega_1 t = \pi$) and $T = 8\tau$, then

$$P(x) = \frac{4}{1+x^2}\left[\sin\left(\sqrt{1+x^2}\frac{\pi}{4}\right)\right]^2\left[\cos(2\pi x)\cos\left(\sqrt{1+x^2}\frac{\pi}{4}\right) - \frac{x}{1+x^2}\sin\left(\sqrt{1+x^2}\frac{\pi}{4}\right)\right]^2, \tag{A.33}$$

and is plotted in Fig. A.1. An important special case of this relation is that corresponding to a nuclear magnetic moment of spin-$\frac{1}{2}$ with gyromagnetic ratio γ, in a fixed field of strength B_0, with a weak field of strength B_1 perpendicular to B_0 and rotating about B_0. In this case, the above equation applies with

$$\omega_0 = \gamma B_0\,, \lambda = \omega_0 - \omega \tag{A.34}$$

$$2b = \gamma B_1 = \frac{\omega_0 B_1}{B_0} \tag{A.35}$$

p.pdf

Figure A.1: The graph above shows the transition probability of spin down using Ramsey technique of separated oscillating fields. In this graph $T = 8\tau$ and $b\tau = \frac{\pi}{4}$.

Appendix B

Geometric phase effect

B.0.1 Geometric phase effect as a Bloch-Siegert shift

Experiments designed to measure the electric dipole moment (EDM), typically observe particles of interest as they move through a region of uniform and aligned $\vec{E}$ and $\vec{B}_0$ fields. The particles under question are usually neutral and have a total spin angular momentum $\vec{J}$. The external field interaction Hamiltonian is

$$H_{ext} = \frac{\mu_a}{J}\vec{J}\cdot\vec{B}_0 - \frac{d_a}{J}\vec{J}\cdot\vec{E}, \tag{B.1}$$

where μ_a and d_a are the magnetic and electric dipole moments, respectively.

The Larmor precesssion frequencies, for parallel and antiparallel $\vec{B}_0$ and $\vec{E}$, are given by the expressions

$$\omega_{L\uparrow\uparrow} = -\frac{(\mu_a B_{0\uparrow\uparrow} + d_a E)}{J\hbar}\ ,\ \omega_{L\uparrow\downarrow} = -\frac{(\mu_a B_{0\uparrow\downarrow} - d_a E)}{J\hbar} \tag{B.2}$$

An EDM will reveal itself by causing a reduction or enhancement of the accumulated precession frequency according to whether the fields are parallel or anti-parallel.

If the particles are moving through static, but non-uniform fields, there exists motion of the fields in the frame of any particle. This causes geometric phases (GP's) in the precession of the total spin of the ensemble, which is generally independent of the precession caused by an EDM. We therefore must add the terms $+\epsilon_{geo\uparrow\uparrow}/T$ and $+\epsilon_{geo\uparrow\downarrow}/T$, respectively, ot the right-hand sides of Equations B.2. For the accumulated phases measured in the time interval T, we then have

$$(|\omega_{L\uparrow\uparrow}| - |\omega_{L\uparrow\downarrow}|)T = \frac{|\mu_a|(B_{0\uparrow\uparrow} - B_{0\uparrow\downarrow})T}{J\hbar} \pm \frac{2d_a ET}{J\hbar} \pm (\varepsilon_{geo\uparrow\uparrow} - \varepsilon_{geo\uparrow\downarrow})\ , \tag{B.3}$$

where the sign alternative has to be chosen to be the same as the sign of μ_a. Assuming that B_0 remains constant while $\vec{E}$ is revered, then the first term is zero. The geometric phase term will result in a false EDM $d_a f$ given by

$$d_{af} = -(\varepsilon_{geo\uparrow\uparrow} - \varepsilon_{geo\uparrow\downarrow})\frac{J\hbar}{2ET} = -(\Delta\omega_{geo\uparrow\uparrow} - \Delta\omega_{geo\uparrow\downarrow})\frac{J\hbar}{2E}\ , \tag{B.4}$$

where $\Delta\omega_{geo\uparrow\uparrow}$ is the average rate of accumulation of the GP proportional to E for the particle ensemble of spins in parallel fields.

As a particle moves through the electric field with velocity v, it experiences an effective magnetic field

$$\vec{B}_v = \frac{\vec{E} \times \vec{v}}{c^2} \ , \tag{B.5}$$

which interacts with the particles magnetic moment μ_a, creating a geometric phase. This is independent of the interaction of a genuine EDM with the $\vec{E}$ field. A gradient $\partial B_{0z}/\partial z$, in the case of cylindrical symmetry, has the associated components in the xy plane,

$$\vec{B}_{0xy} = \vec{B}_{0r} = -\left(\frac{\partial B_{0z}}{\partial z}\right)\frac{\vec{r}}{2} \ , \tag{B.6}$$

at all radial positions $\vec{r}$ relative to the axis of symmetry.

A geometric phase is caused by the combination of $\vec{B}_v$ and $\vec{B}_{0xy}$, thus we have

$$\vec{B}_{xy} = (\vec{B}_{0xy} + \vec{B}_v) \ . \tag{B.7}$$

These fields are varying with position in the trap. We will assume that inhomogeneities in $\vec{E}$ are small enough that they only effect $\vec{B}_v$ to second order, and thus we will not consider them.

The particles are assumed to be moving in conditions where $mc^2 \gg mv^2 \gg |\mu_a B_0|$. Thus, no relativity is needed other than Equation B.5.

Ramsey considered a neutral particle with spin and magnetic moment precessing with an angular velocity $\omega_L = \omega_0 = -\gamma B_{0z}$ in a constant magnetic field $\vec{B}_{0z}$ and the addition of a magnetic field of strength B_{xy} in the xy plane rotating in the plane at angular velocity ω_r. He found that the Larmor precession frequency ω_L is shifted away from ω_0, and to first order, this shift $\Delta\omega = \omega_L - \omega_0$ is given by

$$\Delta\omega = \frac{\omega_{xy}^2}{2(\omega_0 - \omega_r)} \ , \tag{B.8}$$

where $\omega_{xy} = -\gamma B_{xy}$ [**?**]. We will refer to this as the Ramsey-Bloch-Siegert (RBS) shift. It is useful to note that the numerator ω_{xy}^2 is

$$\omega_{xy}^2 = \gamma^2 \vec{B}_{xy}^2 = \gamma^2(\vec{B}_{0xy}^2 + \vec{B}_v^2 + 2\vec{B}_{0xy} \cdot \vec{B}_v) \ . \tag{B.9}$$

The first term takes into account the influence of $\vec{B}_{xy}$ on ω_L in the absence of an $\vec{E}$ field. The second term is proportional to $(\vec{E} \times \vec{v})^2$, and is involved in the calculation of the second order $(\vec{E} \times \vec{v})$ shift. The third term is the one that causes the GP shifts linear in E.

Consider a particle in a cylindrical storage vessel with the shape shown in Fig. B.0.1. The z-axis points along the cylinder axis of the trap. Circular electrodes in the xy plane form the roof and floor of the trap, and the walls are fully specular in terms of reflections of particles. We also assume no particle-particle collisions.

We may assume that the particles motion is confined to the xy plane with velocity v_{xy}, since any motion in the z-direction does not contribute to the GP's under investigation $(\vec{E} \times \vec{v} = 0)$. The $\vec{B}_0$ field is taken to be nearly uniform with a small gradient $\partial \vec{B}_{0z}/\partial z$ that is to first order independent of position. As in B.6, we have

$$\vec{B}_{0xy} = \vec{B}_{0r} = -\frac{\partial B_{0z}}{\partial z}\frac{\vec{r}}{2} = B_{0r}\frac{\vec{r}}{r} \ . \tag{B.10}$$

trap.png

Figure B.1: Effective magnetic field in the rotating coordinate system

Very close to the wall of the trap, $\vec{B}_{0r}$ and $\vec{B}_v$ are nearly parallel and aligned with the radius $\vec{r}$. Therefore, a particle moving along the edge of the trap experiences rotating radial magnetic field of amplitudes;

$$\text{for } \vec{B}_{0\uparrow} \text{ and } \vec{E}_{\uparrow},\;\; B_{xy+} = B_{0r} - |B_v|,\;\; B_{xy-} = B_{0r} + |B_v|\;, \tag{B.11}$$

$$\text{for } \vec{B}_{0\uparrow} \text{ and } \vec{E}_{\downarrow},\;\; B_{xy+} = B_{0r} + |B_v|,\;\; B_{xy-} = B_{0r} - |B_v|\;, \tag{B.12}$$

where the (+) case is the sense with the particles angular momentum vector parallel to $\vec{B}_0$ and the (-) case is the opposite sense. This peripheral motion has $|\omega_r| = v_{xy}/R$, where R is the trap radius. We then have the following relations:

$$|B_v| = \frac{|v_{xy}||E|}{c^2},\; |\omega_0| = |\gamma B_{0z}|,\; |\omega_r| = \frac{|v_{xy}|}{R}, \tag{B.13}$$

$$B_{0r} \rightarrow \{B_{0R} = -\frac{\partial B_{0z}}{\partial z}\frac{R}{2}\} \;\text{ as }\; \alpha \rightarrow 0\;.$$

These rotating fields induce shifts in the Larmor frequency, which is described by the RBS shift equation. In mechanical equilibrium, any particle is equally likely to move in either direction around the trap. We are interested in the ensemble average shift, and so we equally weight the shifts of the two senses of circulation, giving

$$\Delta\omega = \frac{(\gamma B_{xy+})^2}{4(\omega_0 - |\omega_r|)} + \frac{(\gamma B_{xy-})^2}{4(\omega_0 + |\omega_r|)}\;. \tag{B.14}$$

Inserting our expressions for $B_{xy\pm}$, we get

$$\begin{aligned}\Delta\omega_{\uparrow\uparrow} = & \frac{\gamma^2(B_{0R}^2 + B_v^2)}{4}\left[\frac{1}{(\omega_0 - |\omega_r|)} + \frac{1}{(\omega_0 + |\omega_r|)}\right] \\ & - \frac{\gamma^2 B_{0R}|B_v|}{2}\left[\frac{1}{(\omega_0 - |\omega_r|)} - \frac{1}{(\omega_0 + |\omega_r|)}\right]\;,\end{aligned} \tag{B.15}$$

$$
\begin{aligned}
\Delta\omega_{\uparrow\downarrow} =& \frac{\gamma^2(B_{0R}^2+B_v^2)}{4}\left[\frac{1}{(\omega_0-|\omega_r|)}+\frac{1}{(\omega_0+|\omega_r|)}\right] \\
&+\frac{\gamma^2 B_{0R}|B_v|}{2}\left[\frac{1}{(\omega_0-|\omega_r|)}-\frac{1}{(\omega_0+|\omega_r|)}\right] .
\end{aligned}
\tag{B.16}
$$

Taking the difference

$$
\begin{aligned}
(\Delta\omega_{\uparrow\uparrow}-\Delta\omega_{\uparrow\downarrow}) &= -\gamma^2 B_{0R}|B_v|\left[\frac{1}{(\omega_0-|\omega_r|)}-\frac{1}{(\omega_0+|\omega_r|)}\right] \\
&= -2\gamma^2 B_{0R}|B_v|\frac{|\omega_r|}{(\omega_0^2-\omega_r^2)} ,
\end{aligned}
\tag{B.17}
$$

we can see that only the cross terms involving $B_{0R}|B_v|$ contribute to the GP that is linear in E. The factor $(\omega_0^2-\omega_r^2)^-1$ has a sharp peak and changes sign at the boundary between the ranges $|\omega_r|<|\omega_0|$ and $|\omega_r|>|\omega_0|$.

Typical neutron EDM measurements using ultra-cold neutrons (UCNs) work in the nearly adiabatic regime where $|\omega_r|<|\omega_0|$. In this case, we rearrange Eqn. B.17, in the form

$$
(\Delta\omega_{\uparrow\uparrow}-\Delta\omega_{\uparrow\downarrow}) = -2\gamma^2 B_{0R}|B_v|\frac{|\omega_r|}{\omega_0^2}\left[1-\frac{\omega_r^2}{\omega_0^2}\right]^{-1} . \tag{B.18}
$$

Comparing this with $(\Delta\omega_{geo\uparrow\uparrow}-\Delta\omega_{geo\uparrow\downarrow})$ from Eqn. B.4, and using the relations in Eqn. B.13, we find that

$$
d_{af} = -\frac{J\hbar}{2}\left(\frac{\partial B_{0z}/\partial z}{B_{0z}^2}\right)\frac{v_{xy}^2}{c^2}\left[1-\frac{\omega_r^2}{\omega_0^2}\right]^{-1} , \tag{B.19}
$$

for particles moving in peripheral orbits.

B.0.2 T1,T2, GPE redux

An alternative approach to determining the geometric phase effect provides a more general theory, valid for an arbitrary shape of the magnetic field as well as for arbitrary geometry of the confinement cell [**?**].

The frequency shift induced by a fluctuating transverse field is given by the Lamoreaux-Golub expression [**?**]:

$$
\delta\omega = \frac{1}{2}\int_0^\infty d\tau\cos(\omega_0 t)\langle\omega_x(0)\omega_y(\tau)-\omega_y(0)\omega_x(\tau)\rangle+\frac{1}{2}\int_0^\infty d\tau\sin(\omega_0 t)\langle\omega_x(0)\omega_x(\tau)-\omega_y(0)\omega_y(\tau)\rangle, \tag{B.20}
$$

where the bracket refers to the ensemble average of the quantity of particles in the trap.

We can write the frequency shift in powers of the magnetic and electric field:

$$
\delta\omega = \delta\omega_{B^2}+\delta\omega_{E^2}+\delta\omega_{BE}. \tag{B.21}
$$

If we flip the direction of the electric field, only the linear term in E

$$
\delta\omega_{BE} = \frac{\gamma^2 E}{c^2}\int_0^\infty d\tau\cos(\omega_0\tau)\langle B_x(0)v_x(\tau)+B_y(0)V_y(\tau)\rangle \tag{B.22}
$$

generates a frequency shift (as long as the field amplitude doesn't change). Therefore, it generates a false EDM of:

$$
d_{False} = \frac{\hbar}{4E}[\delta\omega(E)-\delta\omega(-E)] = \frac{\hbar}{4E}\delta\omega_{BE}(E), \tag{B.23}
$$

The frequency shifts $\delta\omega_{B^2}$, $\delta\omega_{E^2}$, and $\delta\omega_{BE}$ involve Fourier transforms (evaluated at the Larmor frequency) of correlation functions involving field and velocity components. In the adiabatic regime these can be expanded in perturbation series using integration by parts:

$$\int_0^\infty d\tau \cos(\omega_0\tau)\langle B_x(0)v_x(\tau)\rangle = [\cos(\omega_0\tau)\langle B_x(0)x(\tau)\rangle]_0^\infty + \omega_0 \int_0^\infty d\tau \sin(\omega_0\tau)\langle B_x(0)x(\tau)\rangle, \tag{B.24}$$

where the second term vanishes in the nonadiabatic limit ($\omega_0\tau_c \ll 1$). Using this expansion with Eqn.B.22, we arrive at a false EDM:

$$d_{False} = -\frac{\hbar\gamma^2}{2c^2}\langle xB_x + yB_y\rangle, \tag{B.25}$$

which is valid for arbitrary field inhomogeneities in the nonadiabatic regime.

B.0.3 Why is it called a geometric phase?

In the nEDM experiment, it is important to understand how UCN move adiabatically through a magnetic field gradient. In the frame of reference of the UCN, the magnetic field is changing with time, which results in a Berry phase shift as the particle moves through a closed curve. Since the UCN is moving slowly with respect to the change in magnetic field, its spin will follow the field adiabatically. The change in field strength with time is then reflected in the geometry of the container that the UCN are moving in, and therefore the phase accrued is geometric in origin.

Adiabatic Approximation

Consider a Hamiltonian that depends on some set of parameters. If these parameters change “slowly” with time, then the energy eigenvalues will also change as the parameters themselves change. By slowly, we mean that the parameters change on a time scale T that is much greater than $\frac{2\pi\hbar}{E_{ab}}$ for some difference E_{ab} in energy eigenstates.

Starting from the eigenvalue equation for Hamiltonian :

$$H(t)|n;t\rangle = E_n(t)|n;t\rangle, \tag{B.26}$$

the Schrödinger equation can be written as

$$i\hbar\frac{d}{dt}|\alpha;t\rangle = H(t)|\alpha;t\rangle. \tag{B.27}$$

We can write $|\alpha;\rangle$ in terms of Hamiltonian eigenkets

$$|\alpha;t\rangle = \sum_n c_n(t)e^{i\theta_n(t)}|n;t\rangle, \tag{B.28}$$

where

$$\theta_n(t) \equiv -\frac{1}{\hbar}\int_0^t E_n(t')dt'. \tag{B.29}$$

By substituting equation B.28 into B.27 we find

$$\sum_n e^{i\theta_n(t)}\left[\dot{c}_n(t)|n;t\rangle + c_n(t)\frac{\partial}{\partial t}|n;t\rangle\right] = 0. \tag{B.30}$$

If we multiply the above equation with $\langle m;t|$ and use orthonormality of Hamiltionian eigenstates at equal times, we get

$$\dot{c}_m(t) = -\sum_n c_n(t)e^{i[\theta_n(t)-\theta_m(t)]}\langle m;t|\left[\frac{\partial}{\partial t}|n;t\rangle\right]. \quad \text{(B.31)}$$

Now, we need to calculate $\langle m;t|\left[\frac{\partial}{\partial t}|n;t\rangle\right]$ in terms of the Hamiltonian and its eigenvalues. To do this, we should take the time derivative of Equation B.26, and then multiply it on the left by $\langle m;t|$:

$$\langle m;t|\dot{H}|n;t\rangle = [E_n(t)-E_m(t)]\,\langle m;t|\left[\frac{\partial}{\partial t}|n;t\rangle\right]. \quad \text{(B.32)}$$

Therefore, we obtain

$$\dot{c}_m(t) = -c_m(t)\langle m;t|\left[\frac{\partial}{\partial t}|n;t\rangle\right] - \sum_{n\neq m} c_n(t)e^{i(\theta_n-\theta_m)}\frac{\langle m;t|\dot{H}|n;t\rangle}{E_n-E_m}. \quad \text{(B.33)}$$

This is the solution to the general time-dependent problem and it means, as time goes on, states with $n \neq m$ will mix with $|m;t\rangle$ because of the time dependence of the Hamiltonian. In the adiabatic limit, we can neglect the second term which means,

$$\frac{\langle m;t|\dot{H}|n;t\rangle}{E_{nm}} \equiv \frac{1}{\tau} \ll \langle m;t|\left[\frac{\partial}{\partial t}|m;t\rangle\right] \sim \frac{E_m}{\hbar}. \quad \text{(B.34)}$$

In other words, the Hamiltonian changes with time much slower than the inverse natural frequency of the state-phase factor. Hence,

$$c_n(t) = e^{i\gamma_n(t)}c_n(0), \quad \text{(B.35)}$$

where,

$$\gamma_n(t) \equiv i\int_0^t \langle n;t'|\left[\frac{\partial}{\partial t'}|n;t'\rangle\right]dt', \quad \text{(B.36)}$$

is a real quantity. This is called the geometric phase, and it is the result of the adiabatic approximation. So, we can rewrite equation B.28 as

$$|\alpha^{(n)};t\rangle = e^{i\gamma_n(t)}e^{i\theta_n(t)}|n;t\rangle. \quad \text{(B.37)}$$

Berry's Phase

The accumulated phase for systems that travel in a closed loop is generaly called Berry's phase, although Berry himself refers to it as a "geometric phase".

Assume that the time dependence of the Hamiltonian is represented by a parameter $\vec{R}(t)$. For example, it can be a magnetic field for a spin-$\frac{1}{2}$ system. Therefore, $E_n(t) = E_n(\vec{R}(t))$ and $|n;t\rangle = |n(\vec{R}(t))\rangle$, and also

$$< n;t|\left[\frac{\partial}{\partial t}|n;t>\right] =< n;t|\left[\vec{\nabla}_R|n;t>\right]\cdot\frac{d\vec{R}}{dt}. \quad \text{(B.38)}$$

Combining equation B.36 and B.38 we get,

$$\begin{aligned}\gamma_n(T) &= i\int_0^T \langle n;t|\left[\vec{\nabla}_R|n;t\rangle\right]\cdot\frac{d\vec{R}}{dt}dt \\ &= i\int_{\vec{R}(0)}^{\vec{R}(t)} \langle n;t|\left[\vec{\nabla}_R|n;t\rangle\right]\cdot d\vec{R}.\end{aligned} \tag{B.39}$$

If T is the period for one full cycle then $\vec{R}(0) = \vec{R}(t)$ and therefore, we can calculate the geometric phase for a closed loop in which the vector $\vec{R}$ traces a curve C:

$$\gamma_n(C) = i\oint < n;t|\left[\vec{\nabla}_R|n;t>\right]\cdot d\vec{R}. \tag{B.40}$$

Let's define,

$$\vec{A}_n(\vec{R}) \equiv i\langle n;t|\left[\vec{\nabla}_R|n;t\rangle\right], \tag{B.41}$$

and so, the geometric phase will take the form

$$\gamma_n(C) = \oint_c \vec{A}_n(\vec{R})\cdot d\vec{R}. \tag{B.42}$$

Using Stokes' theorem we get

$$\gamma_n(C) = \int \left[\vec{\nabla}_R \times \vec{A}_n(\vec{R})\right]\cdot d\vec{a}. \tag{B.43}$$

Thus, Berry's Phase is determined by the "flux" of a generalized field

$$\vec{B}_n(\vec{R}) \equiv \vec{\nabla}_R \times \vec{A}_n(\vec{R}). \tag{B.44}$$

Equation B.42 has an interesting property. If you multiply the energy eigenkets by an arbitrary phase, the value of $\gamma_n(c)$ will not be affected because the curl of a gradient is zero. This means, the geometric phase does not depend on the phase behavior along the path and it only depends on the geometry of the path traced out by $\vec{R}(t)$, which is why it is called a "geometric phase".
By doing a little math, we can rewrite Berry's phase as

$$\vec{B}_n(\vec{R}) = i\sum_{n\neq m}\frac{\langle n;t|\vec{\nabla}_R H|m;t\rangle \times \langle m;t|\vec{\nabla}_R H|n;t\rangle}{(E_m - E_n)^2}. \tag{B.45}$$

Example:Berry's Phase for Spin-1/2

We can easily calculate the geometric phase for a spin-$\frac{1}{2}$ particle manipulated slowly through a time-varying magnetic field. As before, we can write the Hamiltonian as

$$H = -\frac{2\mu}{\hbar}\vec{S}.\vec{R}(t) = -\gamma\vec{S}\cdot\vec{R}(t). \tag{B.46}$$

$R(t)$ represents the magnetic field to avoid confusion with Berry's phase $\vec{B}_n(\vec{R})$. We can consider $|\pm;t\rangle$ to be the eigenstates of S_z. If we write

$$\vec{S} = \frac{1}{2}(S_+ + S_-)\hat{x} + \frac{1}{2i}(S_+ - S_-)\hat{y} + S_z\hat{z}, \tag{B.47}$$

then we can write

$$\langle \pm; t|\vec{S}|\mp; t\rangle = \frac{\hbar}{2}(\hat{x} \mp i\hat{y}). \tag{B.48}$$

Combining these results we finally get

$$\gamma_{\pm}(C) = \mp\frac{1}{2}\int \frac{\hat{\vec{R}} \cdot d\vec{a}}{R^2} = \mp\frac{1}{2}\Omega, \tag{B.49}$$

where Ω is the "solid angle" subtended by the path through which the parameter vector $\vec{R}(t)$ travels, relative to an origin $\vec{R} = 0$ that is the source point for the field $\vec{B}$. This implies that the specifics of the path do not matter, so long as the solid angle subtended by the path is the same. This is also independent of the magnetic moment μ.

References

[1] Salvat, D. J., Gutsmiedl, E., Liu, C.-Y., Geltenbort, P., Orecchini, A., Paul, S., and Schober, H., EPL **103**, 12001 (2013).

[2] F. Atchison, B. Blau, K. Bodek, B. van den Brandt, T. Bryś, M. Daum, P. Fierlinger, A. Frei, P. Geltenbort, P. Hautle, R. Henneck, S. Heule, A. Holley, M. Kasprzak, K. Kirch, A. Knecht, J. Konter, M. Kuźniak, C.-Y. Liu, C. Morris, A. Pichlmaier, C. Plonka, Y. Pokotilovski, A. Saunders, Y. Shin, D. Tortorella, M. Wohlmuther, A. Young, J. Zejma, and G. Zsigmond, Nuclear Instruments and Methods in Physics Research Section A: Accelerators, Spectrometers, Detectors and Associated Equipment **611**, 252 (2009), particle Physics with Slow Neutrons.

[3] E. Alsolami, *An examination of keystroke dynamics for continuous user authentication*, Ph.D. thesis, Queensland University of Technology (2012).

[4] K. Kirch, B. Lauss, P. Schmidt-Wellenburg, and G. Zsigmond, Nuclear Physics News **20**, 17 (2010), https://doi.org/10.1080/10619121003626724 .

[5] P. Schmidt-Wellenburg, K. Andersen, and O. Zimmer, Nuclear Instruments and Methods in Physics Research Section A: Accelerators, Spectrometers, Detectors and Associated Equipment **611**, 259 (2009), particle Physics with Slow Neutrons.

[6] E. Korobkina, R. Golub, B. Wehring, and A. Young, Physics Letters A **301**, 462 (2002).

[7] W. Schott, J.M. Pendlebury, I. Altarev, S. Gröger, E. Gutsmiedl, F.J. Hartmann, S. Paul, G. Petzoldt, P. Schmidt-Wellenburg, and U. Trinks, Eur. Phys. J. A **16**, 599 (2003).

[8] B. Fåk and K. Andersen, Physics Letters A **160**, 468 (1991).

[9] F. Atchison, B. Blau, K. Bodek, B. van den Brandt, T. Bryś, M. Daum, P. Fierlinger, A. Frei, P. Geltenbort, P. Hautle, R. Henneck, S. Heule, A. Holley, M. Kasprzak, K. Kirch, A. Knecht, J. A. Konter, M. Kuźniak, C.-Y. Liu, C. L. Morris, A. Pichlmaier, C. Plonka, Y. Pokotilovski, A. Saunders, Y. Shin, D. Tortorella, M. Wohlmuther, A. R. Young, J. Zejma, and G. Zsigmond, Phys. Rev. Lett. **99**, 262502 (2007).

[10] A. Frei, E. Gutsmiedl, C. Morkel, A. R. Müller, S. Paul, S. Rols, H. Schober, and T. Unruh, EPL (Europhysics Letters) **92**, 62001 (2010).

[11] C. L. Morris, J. M. Anaya, T. J. Bowles, B. W. Filippone, P. Geltenbort, R. E. Hill, M. Hino, S. Hoedl, G. E. Hogan, T. M. Ito, T. Kawai, K. Kirch, S. K. Lamoreaux,

C.-Y. Liu, M. Makela, L. J. Marek, J. W. Martin, R. N. Mortensen, A. Pichlmaier, A. Saunders, S. J. Seestrom, D. Smith, W. Teasdale, B. Tipton, M. Utsuro, A. R. Young, and J. Yuan, Phys. Rev. Lett. **89**, 272501 (2002).

[12] C. Bidinosti and J. Martin, AIP Advances **4**, 047135 (2014).

[13] F. Rehm, "Bachelor Thesis, Heat conductivity in superfluid helium and ultracold neutron source cryogenics," (2018).

[14] F. Atchison, B. Blau, A. Bollhalder, M. Daum, P. Fierlinger, P. Geltenbort, G. Hampel, M. Kasprzak, K. Kirch, S. Köchli, *et al.*, Nuclear Instruments and Methods in Physics Research Section A: Accelerators, Spectrometers, Detectors and Associated Equipment **608**, 144 (2009).

[15] G. Ban, G. Bison, K. Bodek, Z. Chowdhuri, P. Geltenbort, W. C. Griffith, V. Hélaine, R. Henneck, M. Kasprzak, Y. Kermaidic, K. Kirch, S. Komposch, P. A. Koss, A. Kozela, J. Krempel, B. Lauss, T. Lefort, Y. Lemière, A. Mtchedlishvili, M. Musgrave, O. Naviliat-Cuncic, F. M. Piegsa, E. Pierre, G. Pignol, G. Quéméner, M. Rawlik, D. Ries, D. Rebreyend, S. Roccia, G. Rogel, P. Schmidt-Wellenburg, N. Severijns, E. Wursten, J. Zejma, and G. Zsigmond, The European Physical Journal A **52**, 326 (2016).

[16] V. F. Sears, Neutron news **3**, 26 (1992).

[17] M. Pospelov and A. Ritz, Annals of physics **318**, 119 (2005).

[18] T. D. Lee and C.-N. Yang, Physical Review **105**, 1671 (1957).

[19] C. S. Wu, E. Ambler, R. W. Hayward, D. D. Hoppes, and R. P. Hudson, Phys. Rev. **105**, 1413 (1957).

[20] R. L. Garwin, L. M. Lederman, and M. Weinrich, Phys. Rev. **105**, 1415 (1957).

[21] J. I. Friedman and V. Telegdi, Physical Review **106**, 1290 (1957).

[22] L. Landau, Nuclear Physics **3**, 127 (1957).

[23] J. D. Jackson, S. B. Treiman, and H. W. Wyld, Phys. Rev. **106**, 517 (1957).

[24] M. Romalis, W. Griffith, J. Jacobs, and E. Fortson, Physical Review Letters **86**, 2505 (2001).

[25] J. Smith, E. Purcell, and N. Ramsey, Physical Review **108**, 120 (1957).

[26] J. Pendlebury, S. Afach, N. Ayres, C. Baker, G. Ban, G. Bison, K. Bodek, M. Burghoff, P. Geltenbort, K. Green, *et al.*, Physical Review D **92**, 092003 (2015).

[27] J. M. Cline, (2006), arXiv:hep-ph/0609145 [hep-ph] .

[28] A. Sakharov, Pisma Zh.Eksp.Teor.Fiz. **5**, 32 (1967).

[29] E. W. Kolb and M. S. Turner, Front. Phys., Vol. 69, **1** (1990).

[30] A. G. Cohen, D. Kaplan, and A. Nelson, Annual Review of Nuclear and Particle Science **43**, 27 (1993).

[31] B. Graner, Y. Chen, E. Lindahl, and B. Heckel, arXiv preprint arXiv:1601.04339 (2016).

[32] C. Baker, G. Ban, K. Bodek, M. Burghoff, Z. Chowdhuri, M. Daum, M. Fertl, B. Franke, P. Geltenbort, K. Green, *et al.*, Physics Procedia **17**, 159 (2011).

[33] J.-C. Peng, Modern Physics Letters A **23**, 1397 (2008).

[34] I. Altarev, E. Babcock, D. Beck, M. Burghoff, S. Chesnevskaya, T. Chupp, S. Degenkolb, I. Fan, P. Fierlinger, A. Frei, *et al.*, Review of scientific instruments **85**, 075106 (2014).

[35] I. Altarev, M. Bales, D. Beck, T. Chupp, K. Fierlinger, P. Fierlinger, F. Kuchler, T. Lins, M. Marino, B. Niessen, *et al.*, Journal of Applied Physics **117**, 183903 (2015).

[36] I. Altarev, P. Fierlinger, T. Lins, M. Marino, B. Nießen, G. Petzoldt, M. Reisner, S. Stuiber, M. Sturm, J. T. Singh, *et al.*, Journal of Applied Physics **117**, 233903 (2015).

[37] I. Altarev, D. Beck, S. Chesnevskaya, T. Chupp, W. Feldmeier, P. Fierlinger, A. Frei, E. Gutsmiedl, F. Kuchler, P. Link, *et al.*, Nuovo Cimento-C **35**, 122 (2012).

[38] B. Franke, *Investigations of the internal and external magnetic fields of the neutron electric dipole moment experiment at the Paul Scherrer Institute*, Ph.D. thesis, ETH Zurich (2013).

[39] A. Knecht, *Towards a New Measurement of the Neutron Electric Dipole Moment*, Ph.D. thesis, Zurich (2009).

[40] R. Golub and S. K. Lamoreaux, Physics Reports **237**, 1 (1994).

[41] R. Golub, D. Richardson, and S. K. Lamoreaux, *Ultra-cold neutrons* (CRC Press, 1991).

[42] K. A. O. et al. (Particle Data Group), Chin. Phys. C ((2014) and 2015 update).

[43] C. Baker, D. Doyle, P. Geltenbort, K. Green, M. Van der Grinten, P. Harris, P. Iaydjiev, S. Ivanov, D. May, J. Pendlebury, *et al.*, Physical Review Letters **97**, 131801 (2006).

[44] A. Serebrov, P. Geltenbort, I. Shoka, G. Shmelev, A. Kharitonov, A. Vassiliev, I. Krasnoshekova, M. Lasakov, E. Siber, A. Fomin, *et al.*, Nuclear Instruments and Methods in Physics Research Section A: Accelerators, Spectrometers, Detectors and Associated Equipment **611**, 263 (2009).

[45] S. Lamoreaux and R. Golub, Journal of Physics G: Nuclear and Particle Physics **36**, 104002 (2009).

[46] I. Altarev, G. Ban, G. Bison, K. Bodek, M. Burghoff, Z. Chowdhuri, M. Daum, C. Düsing, M. Fertl, P. Fierlinger, *et al.*, Nuclear Physics A **844**, 47c (2010).

[47] J. Pendlebury, S. Afach, N. Ayres, C. Baker, G. Ban, G. Bison, K. Bodek, M. Burghoff, P. Geltenbort, K. Green, *et al.*, Physical Review D **92**, 092003 (2015).

[48] S. Paul, Nuclear Instruments and Methods in Physics Research Section A: Accelerators, Spectrometers, Detectors and Associated Equipment **611**, 157 (2009).

[49] F. E. Wietfeldt and G. L. Greene, Reviews of Modern Physics **83**, 1173 (2011).

[50] S. Arzumanov, L. Bondarenko, S. Chernyavsky, W. Drexel, A. Fomin, P. Geltenbort, V. Morozov, Y. Panin, J. Pendlebury, and K. Schreckenbach, Physics Letters B **483**, 15 (2000).

[51] A. Serebrov, V. Varlamov, A. Kharitonov, A. Fomin, Y. Pokotilovski, P. Geltenbort, J. Butterworth, I. Krasnoschekova, M. Lasakov, R. Tal'daev, *et al.*, Physics Letters B **605**, 72 (2005).

[52] P. R. Huffman, C. Brome, J. Butterworth, K. Coakley, M. S. Dewey, S. Dzhosyuk, R. Golub, G. Greene, K. Habicht, S. K. Lamoreaux, *et al.*, Nature **403**, 62 (2000).

[53] M. P. Mendenhall, R. W. Pattie, Y. Bagdasarova, D. B. Berguno, L. J. Broussard, R. Carr, S. Currie, X. Ding, B. W. Filippone, A. García, P. Geltenbort, K. P. Hickerson, J. Hoagland, A. T. Holley, R. Hong, T. M. Ito, A. Knecht, C.-Y. Liu, J. L. Liu, M. Makela, R. R. Mammei, J. W. Martin, D. Melconian, S. D. Moore, C. L. Morris, A. Pérez Galván, R. Picker, M. L. Pitt, B. Plaster, J. C. Ramsey, R. Rios, A. Saunders, S. J. Seestrom, E. I. Sharapov, W. E. Sondheim, E. Tatar, R. B. Vogelaar, B. VornDick, C. Wrede, A. R. Young, and B. A. Zeck (UCNA Collaboration), Phys. Rev. C **87**, 032501 (2013).

[54] L. Broussard and U. Collaboration, AIP Conference Proceedings **1560**, 149 (2013), https://aip.scitation.org/doi/pdf/10.1063/1.4826741 .

[55] .

[56] O. Zimmer, Physics Letters B **685**, 38 (2010).

[57] S. Baessler, V. Nesvizhevsky, K. Protasov, and A. Y. Voronin, Physical Review D **75**, 075006 (2007).

[58] A. P. Serebrov, O. Zimmer, P. Geltenbort, A. K. Fomin, S. Ivanov, E. Kolomensky, I. Krasnoshekova, M. Lasakov, V. M. Lobashev, A. Pirozhkov, *et al.*, JETP letters **91**, 6 (2010).

[59] S. Afach, G. Ban, G. Bison, K. Bodek, M. Burghoff, M. Daum, M. Fertl, B. Franke, Z. Grujić, V. Helaine, *et al.*, Physics Letters B **745**, 58 (2015).

[60] I. Altarev, Phys. Rev. Lett. **103**, 081602 (2009).

[61] V. V. Nesvizhevsky, H. Börner, A. Gagarski, A. Petoukhov, G. Petrov, H. Abele, S. Baeßler, G. Divkovic, F. Rueß, T. Stöferle, *et al.*, Physical Review D **67**, 102002 (2003).

[62] R.GolubJ.M.Pendlebury, Physics Letters A **53**, 133 (1975).

[63] O. Zimmer, F. M. Piegsa, and S. N. Ivanov, Physical review letters **107**, 134801 (2011).

[64] C. Patrignani, P. D. Group, *et al.*, Chinese physics C **40**, 100001 (2016).

[65] A. Steyerl, H. Nagel, F.-X. Schreiber, K.-A. Steinhauser, R. Gähler, W. Gläser, P. Ageron, J. Astruc, W. Drexel, G. Gervais, *et al.*, Physics Letters A **116**, 347 (1986).

[66] A. Steyerl, Nuclear Instruments and Methods **125**, 461 (1975).

[67] A. R. Young (JGU Mainz, Germany, 2016).

[68] R. Golub and J. Pendlebury, Physics Letters A **62**, 337 (1977).

[69] C. R. Brome, J. Butterworth, S. Dzhosyuk, C. Mattoni, D. McKinsey, J. Doyle, P. Huffman, M. Dewey, F. Wietfeldt, R. Golub, *et al.*, Physical review C **63**, 055502 (2001).

[70] G. L. Squires, *Introduction to the Theory of Thermal Neutron Scattering*, 3rd ed. (Cambridge University Press, 2012).

[71] M. Gibbs, W. Stirling, K. Andersen, and H. Schober, Journal of low temperature physics **120**, 55 (2000).

[72] K. H. Andersen, W. G. Stirling, R. Scherm, A. Stunault, B. Fak, H. Godfrin, and A. J. Dianoux, Journal of Physics: Condensed Matter **6**, 821 (1994).

[73] K. K. H. Leung, S. Ivanov, F. M. Piegsa, M. Simson, and O. Zimmer, Phys. Rev. C **93**, 025501 (2016).

[74] A. Frei, E. Gutsmiedl, C. Morkel, A. R. Müller, S. Paul, M. Urban, H. Schober, S. Rols, T. Unruh, and M. Hölzel, Phys. Rev. B **80**, 064301 (2009).

[75] T. V. F., *Slow Neutrons*, 3rd ed. (Israel Program for Scientific Translations, 1965).

[76] C.-Y. Liu, A. R. Young, and S. K. Lamoreaux, Phys. Rev. B **62**, R3581 (2000).

[77] R. Golub and K. Böning, Zeitschrift für Physik B Condensed Matter **51**, 95 (1983).

[78] J. W. Martin (APS DNP meeting, Vancouver, Canada, 2016).

[79] A. Serebrov (Neutron Electric Dipole Moment Workshop, Ascona, Switzerland, 2014).

[80] F. M. Piegsa, M. Fertl, S. N. Ivanov, M. Kreuz, K. K. H. Leung, P. Schmidt-Wellenburg, T. Soldner, and O. Zimmer, Phys. Rev. C **90**, 015501 (2014).

[81] O. Zimmer and R. Golub, Phys. Rev. C **92**, 015501 (2015).

[82] T. Ito (Neutron Electric Dipole Moment Workshop, Ascona, Switzerland, 2014).

[83] D. Ries (Neutron Electric Dipole Moment Workshop, Ascona, Switzerland, 2014).

[84] J. Karch, Y. Sobolev, M. Beck, K. Eberhardt, G. Hampel, W. Heil, R. Kieser, T. Reich, N. Trautmann, and M. Ziegner, The European Physical Journal A **50**, 78 (2014).

[85] R. Picker (Neutron Electric Dipole Moment Workshop, Ascona, Switzerland, 2014).

[86] N. F. Ramsey, Phys. Rev. **78**, 695 (1950).

[87] P. Schmidt-Wellenburg, *Proceedings, 11th Latin American Symposium on Nuclear Physics and Applications: Medellin, Colombia*, AIP Conf. Proc. **1753**, 060002 (2016), arXiv:1602.01997 [nucl-ex] .

[88] J. M. Pendlebury, W. Heil, Y. Sobolev, P. G. Harris, J. D. Richardson, R. J. Baskin, D. D. Doyle, P. Geltenbort, K. Green, M. G. D. van der Grinten, P. S. Iaydjiev, S. N. Ivanov, D. J. R. May, and K. F. Smith, Phys. Rev. A **70**, 032102 (2004).

[89] S. Afach, G. Bison, K. Bodek, F. Burri, Z. Chowdhuri, M. Daum, M. Fertl, B. Franke, Z. Grujic, V. Hélaine, *et al.*, Journal of Applied Physics **116**, 084510 (2014).

[90] J. W. Martin, R. R. Mammei, W. Klassen, C. Cerasani, T. Andalib, C. P. Bidinosti, M. Lang, and D. Ostapchuk, Nuclear Instruments and Methods in Physics Research Section A: Accelerators, Spectrometers, Detectors and Associated Equipment **778**, 61 (2015).

[91] W. C. Griffith, M. D. Swallows, T. H. Loftus, M. V. Romalis, B. R. Heckel, and E. N. Fortson, Phys. Rev. Lett. **102**, 101601 (2009).

[92] T. Momose, in *APS Division of Nuclear Physics Meeting Abstracts* (2014).

[93] G. Ban, K. Bodek, T. Lefort, O. Naviliat-Cuncic, E. Pierre, C. Plonka, and G. Rogel, Nuclear Instruments and Methods in Physics Research, Section A: Accelerators, Spectrometers, Detectors and Associated Equipment **611**, 280 (2009).

[94] B. Jamieson, L. A. Rebenitsch, S. Hansen-Romu, B. Lauss, T. Lindner, R. Mammei, J. W. Martin, and E. Pierre, The European Physical Journal A **53**, 3 (2017).

[95] A. P. Serebrov, E. Kolomenskiy, A. Pirozhkov, I. Krasnoschekova, A. Vassiljev, A. Polushkin, M. Lasakov, A. K. Fomin, I. Shoka, V. Solovey, *et al.*, JETP letters **99**, 4 (2014).

[96] A. Serebrov, S. Boldarev, A. Erykalov, V. Ezhov, V. Fedorov, A. Fomin, V. Ilatovskiy, K. Keshyshev, K. Konoplev, A. Krivshitch, *et al.*, Physics Procedia **17**, 251 (2011).

[97] K. Kirch, in *AIP Conference Proceedings*, Vol. 1560 (AIP, 2013) pp. 90–94.

[98] T. M. Ito, nEdm Collaboration, *et al.*, in *Journal of Physics: Conference Series*, Vol. 69 (IOP Publishing, 2007) p. 012037.

[99] R. Picker, in *Proceedings of the 14th International Conference on Meson-Nucleon Physics and the Structure of the Nucleon (MENU2016)* (2017) p. 010005.

[100] T. Bryś, S. Czekaj, M. Daum, P. Fierlinger, D. George, R. Henneck, M. Kasprzak, K. Kirch, M. Kuźniak, G. Kuehne, *et al.*, Nuclear Instruments and Methods in Physics Research Section A: Accelerators, Spectrometers, Detectors and Associated Equipment **554**, 527 (2005).

[101] B. Patton, E. Zhivun, D. Hovde, and D. Budker, Physical review letters **113**, 013001 (2014).

[102] J. Voigt, S. Knappe-Grüneberg, A. Schnabel, R. Körber, and M. Burghoff, Metrology and Measurement Systems **20**, 239 (2013).

[103] Z. Sun, M. Reisner, P. Fierlinger, A. Schnabel, S. Stuiber, and L. Li, Journal of Applied Physics **119**, 193902 (2016).

[104] B. Franke, Ph.D. thesis, ETH Zürich (2013).

[105] G. Couderchon and J. Tiers, Journal of Magnetism and Magnetic Materials **26**, 196 (1982).

[106] Krupp VDM Magnifer 7904, *Material Data Sheet No. 9004*, Tech. Rep. (Krupp VDM, Aug. 2000).

[107] K. Gupta, K. Raina, and S. Sinha, Journal of alloys and compounds **429**, 357 (2007).

[108] R. Bozorth, "Ferromagnetism, american telephone and telegraph company, 1978," (1993).

[109] "Finite Element Method Magnetics FEMM, version 4.2, available from `http://www.femm.info`. ," .

[110] R. H. Lambert and C. Uphoff, Review of Scientific Instruments **46**, 337 (1975).

[111] T. Sumner, Journal of Physics D: Applied Physics **20**, 692 (1987).

[112] F. Pfeifer and C. Radeloff, Journal of magnetism and magnetic materials **19**, 190 (1980).

[113] "Bartington Instruments Ltd., 10 Thorney Leys Business Park, Witney, Oxon, OX28 4GG, England." .

[114] "Stanford Research Systems, 1290-D Reamwood Ave., Sunnyvale, CA 94089." .

[115] E. Paperno, IEEE transactions on magnetics **35**, 3940 (1999).

[116] D. C. Jiles, Journal of Applied Physics **76**, 5849 (1994).

[117] D. C. Jiles and D. L. Atherton, Journal of applied physics **55**, 2115 (1984).

[118] D. C. Jiles and D. L. Atherton, Journal of magnetism and magnetic materials **61**, 48 (1986).

[119] I. B. Khriplovich and S. K. Lamoreaux, *CP violation without strangeness* (Springer, 1997).

[120] W. F. Brown Jr and J. H. Sweer, Review of Scientific Instruments **16**, 276 (1945).

[121] H. A. Wheeler, Proceedings of the IRE **46**, 1595 (1958).

[122] E. M. Purcell, American Journal of Physics **57**, 18 (1989), https://doi.org/10.1119/1.15860 .

[123] R. Beth, "Brookhaven National Laboratory Report," (), BNL-10143 (1966).

[124] R. Beth, (), US Patent 3466499, September 9, 1969.

[125] C. Bidinosti, I. Kravchuk, and M. Hayden, Journal of Magnetic Resonance **177**, 31 (2005).

[126] R. Turner and R. M. Bowley, Journal of Physics E: Scientific Instruments **19**, 876 (1986).

[127] H.-T. S.S., Concepts in Magnetic Resonance Part A **36A**, 223, https://onlinelibrary.wiley.com/doi/pdf/10.1002/cmr.a.20163 .

[128] B. M. A., F. L. K., and C. Stuart, Concepts in Magnetic Resonance **14**, 9, https://onlinelibrary.wiley.com/doi/pdf/10.1002/cmr.10000 .

[129] L. K. Forbes and S. Crozier, Journal of Physics D: Applied Physics **36**, 68 (2003).

[130] V. V. Kuzmin, C. P. Bidinosti, M. E. Hayden, and P.-J. Nacher, Journal of Magnetic Resonance **256**, 70 (2015).

[131] C. Crawford, "private communication," .

[132] Y. Masuda, T. Kitagaki, K. Hatanaka, M. Higuchi, S. Ishimoto, Y. Kiyanagi, K. Morimoto, S. Muto, and M. Yoshimura, Physical review letters **89**, 284801 (2002).

[133] Y. Masuda, K. Hatanaka, S.-C. Jeong, S. Kawasaki, R. Matsumiya, K. Matsuta, M. Mihara, and Y. Watanabe, Physical review letters **108**, 134801 (2012).

[134] N. Christopher, "Bachelor Thesis, An amalgamation of work on the ultra-cold neutron source and neutron electric dipole moment experiment at TRIUMF," (2016).

[135] M. Kawai, K. Kikuchi, H. Kurishita, J.-F. Li, and M. Furusaka, Journal of nuclear materials **296**, 312 (2001).

[136] S. Pomme, R. Fitzgerald, and J. Keightley, Metrologia **52**, S3 (2015).

[137] W. Schreyer, T. Kikawa, M. J. Losekamm, S. Paul, and R. Picker, Nuclear Instruments and Methods in Physics Research Section A: Accelerators, Spectrometers, Detectors and Associated Equipment **858**, 123 (2017).

[138] A. Steyerl, Zeitschrift für Physik A Hadrons and nuclei **254**, 169 (1972).

[139] S. W. Van Sciver, *Helium cryogenics* (Springer Science & Business Media, 2012).

[140] V. Arp, R. McCarty, and F. Jeffrey, Inc, Data Program (2005).

[141] T. Andalib, "UCN Analysis Report (https://ucn.triumf.ca/)," (2018).